

Self-assembly of confined liquid crystals: From nanoscale physics to designing photonic metamaterials

**Vom Promotionsausschuss der
Technischen Universität Hamburg**
zur Erlangung des akademischen Grades
Doktorin der Naturwissenschaften (Dr. rer. nat.)
genehmigte Dissertation

von
Kathrin Sentker

aus
Papenburg

2020

Erster Gutachter:	Prof. Dr. rer. nat. Patrick Huber
Zweiter Gutachter:	Prof. Dr. Ing. Robert Meißner
Vorsitzender des Prüfungsausschusses:	Prof. Dr. Ing. Otto von Estorff

Tag der mündlichen Prüfung:	19.05.2020
-----------------------------	------------

Abstract

Liquid crystals in combination with nanoporous media, exhibiting structures significantly smaller than the wavelengths of visible light, are promising candidates to design new soft-hard photonic metamaterials. The liquid crystal provides functionality, resulting from temperature tunable anisotropic properties, i.e. optical birefringence, while the nanoporous solid provides a mechanical robust scaffold structure. Then the optical functionality of prospective metamaterials is not determined by the properties of base materials, but from newly designed multiscale structures often absent in the base materials. However, the extreme spatial and topological constraints can result in inhomogeneous molecular arrangements or even the complete suppression of liquid crystallinity in nanoconfinement hampering the optical functionality.

Depending on the type of confining space (meso- and macroporous silica and anodized aluminium oxide) and as a function of temperature, pore size and pore surface chemistry, the molecular self-assembling process and the resulting metamaterial potential of a discotic liquid crystal (HAT6) in nanoconfinement is analyzed. In order to correlate orientational and translational ordering, synchrotron-based 2D X-ray diffraction in combination with high-resolution optical polarimetry measurements are performed.

Resulting from a quantized phase transition a rarely measured material specific parameter giving a measure of the tendency of the liquid crystal to bend along the preferred alignment direction is found. Additionally, the experiments and complementary Monte Carlo simulations show a remarkably rich self-assembly behavior resulting in structures absent in the bulk state. These diverse configurations on the nanoscale result in integrated material systems exhibiting a temperature- and liquid-solid interaction-dependent positive and negative optical birefringence. Hence, the self-organized nanoporous solids in combination with liquid-crystalline self-assembly allow the fabrication of newly designed photonic metamaterials with tailorable optical anisotropy.

Kurzbeschreibung

Flüssigkristalle in Kombination mit nanoporösen Festkörpern, deren Strukturen deutlich kleiner sind als die Wellenlängen des sichtbaren Lichts, sind vielversprechende Kandidaten für das Design neuer photonischer Metamaterialien. Die temperaturabhängigen anisotropen Eigenschaften, insbesondere die Doppelbrechung des Flüssigkristalls liefert die Funktionalität, während der nanoporöse Festkörper eine mechanisch robuste Gerüststruktur gewährleistet. Dann wird die optische Funktionalität dieser Metamaterialien nicht durch die Eigenschaften der Basismaterialien bestimmt, sondern mittels der neu gestalteten Multiskalenstrukturen. Die extremen räumlichen und topologischen Einschränkungen führen jedoch oft zu inhomogenen molekularen Anordnungen oder sogar zur vollständigen Unterdrückung der flüssigkristallinen Eigenschaften, was die optische Funktionalität stark beeinträchtigt.

Abhängig von der Art des porösen Festkörpers (meso- und makroporöses Siliziumdioxid und anodisiertes Aluminiumoxid) und in Abhängigkeit von Temperatur, Porengröße und Porenoberflächenchemie wird die molekulare Selbstorganisation eines diskotischen Flüssigkristalls (HAT6) und das daraus resultierende Potential als Metamaterial analysiert. Zur Korrelation von Orientierungs- und Translationsordnung wird synchrotronbasierte 2D-Röntgendiffraktometrie in Kombination mit hochauflösenden optischen Polarisationsmessungen durchgeführt.

Ausgehend von einem quantisierten Phasenübergang kann ein selten gemessener materialspezifischer Parameter bestimmt werden, der ein Maß für die Tendenz des Flüssigkristalls zur Verbiegung entlang der bevorzugten Ausrichtungsrichtung liefert. Zusätzlich zeigen die Experimente und ergänzenden Monte-Carlo-Simulationen eine vielfältige Selbstorganisation, die zu Strukturen führt, die in den Basismaterialien nicht zu finden sind. Diese unterschiedlichen Konfigurationen auf der Nanoskala führen zu integrierten Materialsystemen, die eine temperaturabhängige positive und negative optische Doppelbrechung aufweisen, welche stark von der Wechselwirkung zwischen Flüssigkristall und Festkörper abhängt. Die nanoporösen Festkörper in Kombination mit der flüssigkristallinen Selbstorganisation ermöglichen somit die Herstellung neu entwickelter photonischer Metamaterialien mit anpassbarer optischer Anisotropie.

Contents

1. Introduction	1
2. The scientific background of liquid crystals	3
2.1. Nematic-to-isotropic phase transition	5
2.1.1. Order parameter	6
2.1.2. Maier-Saupe theory	7
2.1.3. Landau-de Gennes theory	10
2.2. Confinement effects	12
2.2.1. Distortion free energy	12
2.2.2. Capillary melting and freezing	15
2.3. Anisotropic properties	18
2.3.1. Dielectric anisotropy	18
2.3.2. Optical anisotropy	20
3. Materials & techniques	23
3.1. Sample characteristics	23
3.1.1. Discotic liquid crystal	23
3.1.2. Confining hosts	24
3.2. Experimental techniques	29
3.2.1. Sample preparation	29
3.2.2. Optical polarimetry setup	30
3.2.3. X-ray diffraction	34
4. Quantized self-assembly of discotic rings in nanoconfinement	39
5. Tailoring photonic metamaterial properties by discotic self-assembly in nanopores	51
5.1. Phase transition, supercooling and hysteresis	51
5.2. Structure analysis	59
5.2.1. Face-on molecular anchoring in hydrophilic nanochannels	60
5.2.2. Edge-on molecular anchoring in hydrophobic nanochannels	66
5.3. Metamaterial properties	71
6. Conclusion	77

Bibliography	79
A. Appendix	87
A.1. Complementary information	87
A.2. LabView programm	92
A.3. Berek's equation	97

1. Introduction

The liquid crystalline state was first discovered at the end of the 19th century [1, 2]. Causing numerous subsequent research and a wide discourse in the scientific community it took almost a century to develop useful applications [3]. Since then liquid crystals have changed our everyday life regarding liquid crystal displays used in e. g. television, screens, tablets and smartphones.

The most important property that is utilized in these applications is the optical anisotropy, i. e. birefringence. Even in recent research, beyond liquid crystal devices, this property is still of importance. By filling liquid crystals into porous solids, with lattice spacing larger than the molecular length but much smaller than the wavelength of visible light, the whole structure can be described as a metamaterial with resulting effective parameters, such as effective refractive indices [4, 5].

In general, metamaterials derive their mechanical and functional properties not from the base materials, but from their newly designed, often multiscale structures. Utilizing their anisotropic properties, in particular birefringence, the liquid crystal adds functionality, whereas the solid nanopores can guide the self-assembly giving stability against mechanical loading and provide a macroscopic monolithic scaffold structure. Hence, by confining liquid crystals on the nanoscale their often temperature tunable self-assembly and self-healing mechanisms can be used to design a new soft-hard metamaterial resulting in properties that do not naturally occur in the base materials [6, 7].

Liquid crystals with disk-like molecules built up of aromatic cores and aliphatic side chains stack up in columns, which arrange in a two-dimensional lattice. These discotic liquid crystals provide a molecular orientation, and hence spatial modulation in density, not only in one but two dimensions [4]. In addition to their optical anisotropy, discotic columnar liquid crystals exhibit high one-dimensional charge mobility along the stacking direction, resulting from overlapping π -electrons of the aromatic cores [8]. Therefore, they are also of high interest as 1-D semiconductors with possible applications in sensing, light harvesting or emission, and for molecular electronic components [9–12].

In general, the exceptional liquid crystalline properties are strongly sensitive to interfacial interactions and the phase and self-assembly behavior of confined liquid crystals may substantially deviate from the unconfined space [13–17]. Inhomogeneous molecular arrangements or even complete suppression of liquid-crystalline order [18] hamper the optical functionality. In recent years, the effect of confinement on the behavior of dis-

cotic columnar liquid crystals has been investigated intensively [19–25]. All these studies aimed for a particular molecular orientation applicable in organic electronics, i.e. an orientation of the columnar axis along the cylindrical confining space. However, this configuration was only achieved by increasing the rigidity of the columns [24]. Additionally, a complex self-assembly behavior with structural arrangements depending on the size of the confining space, but absent in the bulk state, were found [21, 25]. Nevertheless, the metamaterial potential resulting from these temperature tunable orientational transitions in confinement, especially with regard to the optical properties, has to the best of my knowledge never been analyzed before.

To overcome this lack of knowledge, the molecular orientation of the commercially available triphenylene based discotic liquid crystal HAT6¹ confined in cylindrical pores of porous silica and anodized aluminium oxide is investigated in this thesis. The theoretical background of liquid crystals regarding in particular the isotropic to liquid crystalline phase transition, anisotropic properties and effects of confinement is given in chapter 2. By polarimetry measurements, sensitive to the orientational ordering, and X-ray diffraction measurements, giving additional information about the translational ordering, see chapter 3, the molecular configurations are probed in detail. Confinement effects and resulting structural arrangements of the used discotic liquid crystal are analyzed depending on the type and size of the confining space, the pore surface chemistry and as a function of temperature, see chapters 4 and 5. A temperature dependent quantized phase transition is found enabling the determination of a rarely measured material specific parameter (chapter 4). This parameter gives a tendency of how easy the liquid crystal bends along the preferred alignment direction. Additionally, depending on pore size and surface chemistry the liquid crystalline self-assembly, leading to structural arrangements absent in the bulk state, can be used to tune photonic metamaterial properties of the resulting integrated material system (chapter 5). The thesis ends with a summarizing chapter (chapter 6).

¹2,3,6,7,10,11-hexakis(hexyloxy)triphenylene

2. The scientific background of liquid crystals

Liquid crystalline materials show an intermediate or mesomorphic phase inbetween the crystalline and liquid phase. These two states differ first and foremost in the presence of a regular stacked three-dimensional lattice of their components, or lack thereof. A crystal is defined by the fact, that, if a primitive basis is located at point \vec{x}_0 , the probability of finding an identical pattern at point $\vec{x} = \vec{x}_0 + n_1\vec{a}_1 + n_2\vec{a}_2 + n_3\vec{a}_3$ ($n_{1,2,3} \in \mathbb{Z}$ and $\vec{a}_{1,2,3}$ basis vector) is finite as long as $|\vec{x} - \vec{x}_0| \rightarrow \infty$ holds [27]. Hence, an X-ray diffraction pattern shows sharp Bragg reflections characteristic for the lattice. In contrast, the probability of finding a similar primitive basis at point \vec{x} far away from \vec{x}_0 in a liquid cannot be expressed except by using an average particle density [27]. Consequently, liquid like Bragg reflections are diffuse peaks having a width inversely proportional to an isotropic length scale ξ , also called coherence length, over which correlations are lost.

In liquid crystals a liquid like order exists in at least one direction. In this mesomorphic phase the material still flows like a liquid but has properties of a crystal, e.g. anisotropic properties. By eliminating orientational degrees of freedom in an isotropic liquid anisotropy can be generated. This directional dependency results from the fact, that the correlation function depends on the orientation of $\vec{x} - \vec{x}_0$ with respect to the macroscopically defined axes. This axis, along which liquid crystal molecules preferentially align, is called director \hat{n} , see fig. 2.1. Thus, at least two selected directions,

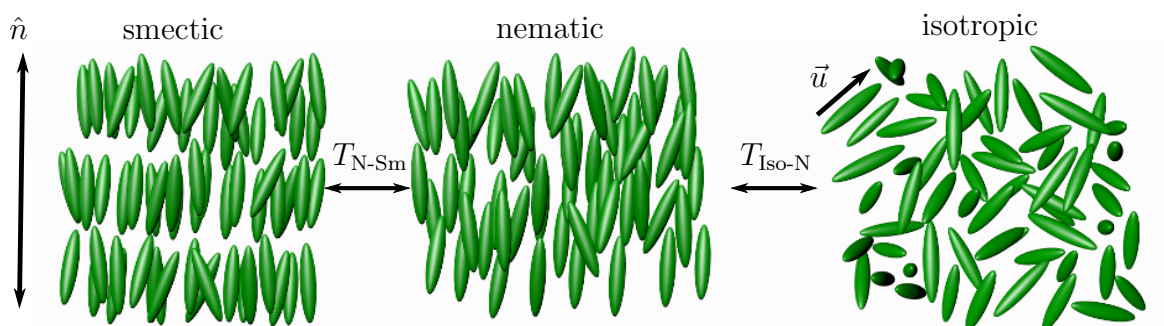


Figure 2.1.: Smectic, nematic and isotropic phase of a thermotropic rod-like liquid crystal. In the nematic phase the molecules align with their long axes represented by \vec{u} along the director \hat{n} . Positional ordering in one dimension, causing regular stacked layers, is imposed in the smectic phase. Adapted and reprinted with permission from [26]. Copyright Springer Fachmedien Wiesbaden 2014.

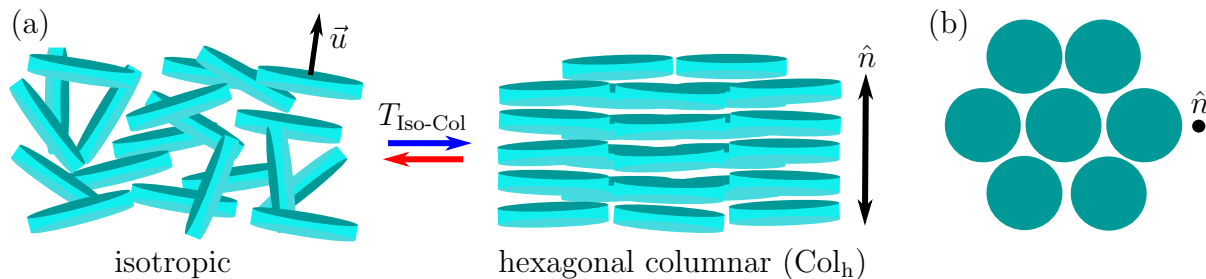


Figure 2.2.: (a) By temperature variations the in the isotropic phase disordered disc shaped molecules start to orient at the phase transition temperature $T_{\text{Iso-Col}}$ along the director \hat{n} forming (b) columns arranged in a hexagonal lattice. This hexagonal columnar phase Col_h is a two-dimensional ordered system with liquid properties along the molecules stacking direction, hence, the director \hat{n} .

perpendicular and parallel to \hat{n} , are present along which correlations decay.

In general liquid crystals can be classified based on how the mesophase is obtained. *Lyotropic* liquid crystals are generated by adding a solvent. In contrast to that, *thermotropic* liquid crystals, used in this thesis, change their phases by varying the systems temperature, as shown for e. g. elongated molecules in fig 2.1. In the high temperature isotropic phase no order is present. Upon cooling, at the isotropic to nematic phase transition temperature $T_{\text{Iso-N}}$, the elongated molecules start to orient along \hat{n} . In this *nematic* phase no positional ordering is present. Further decrease in temperature may impose additional positional order in one dimension. Below the nematic-to-smectic phase transition temperature $T_{\text{N-Sm}}$ the compounds form two-dimensional liquid layers that stack on top of each other in a regular pattern. These systems are called *smectics*. Comparable to that a two-dimensional ordered system in three dimensions is called a *columnar phase*. But in contrast to smectics, that have elongated rod-like molecules, columnar phases can also be realized with disk-like molecules.

These thermotropic discotic liquid crystals (DLCs) usually consist of molecules that have a central discotic core made up of aromatic rings substituted by several saturated aliphatic (CH compounds) chains, see e. g. fig. 3.1. The π - π -interaction of the conjugated carbon rings promotes crystalline properties, while the liquid character results from melting of the alkyl chains. This microsegregation results in four mesophases formed by disk-like molecules: nematic, smectic, cubic and columnar phases [28]. The latter is the most frequent phase and the DLC investigated in this thesis solely show a columnar phase. At low temperature in the liquid crystalline phase, due to the molecular interaction of the conjugated cores, the molecules stack on top of each other forming columns, see fig. 2.2(a). These columns then arrange in an hexagonal lattice resulting in a two-dimensional ordered system, see fig. 2.2(b). This columnar hexagonal mesophase is abbreviated Col_h and possesses a $P6/mmm$ planar space group [28]. In this phase the liquid like properties are present only along the stacking direction of the molecules, hence, the director \hat{n} . Notice, that in contrast to rod-like liquid crystals the director points along the short axis of the

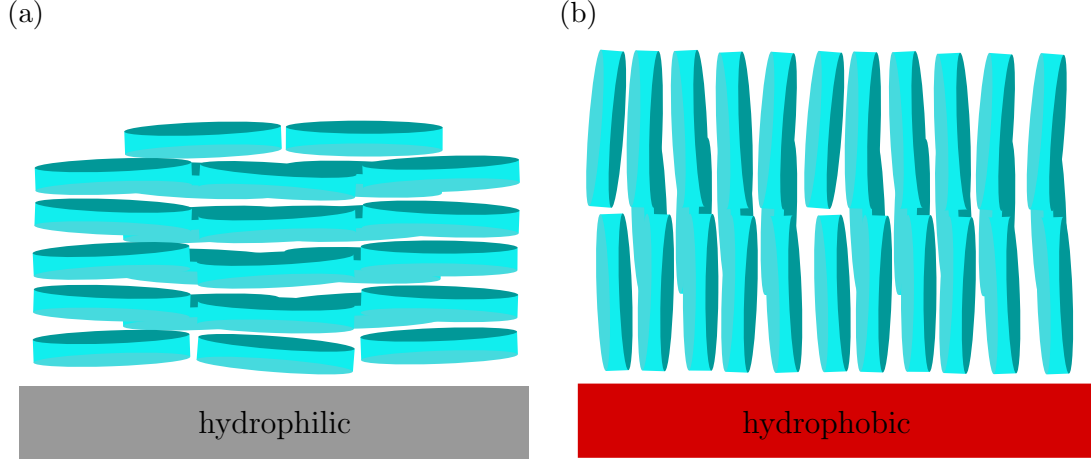


Figure 2.3.: Orientational order of discotic liquid crystal close to a (a) hydrophilic and (b) hydrophobic surface resulting in face-on (homeotropic) or edge-on (planar or homogeneous) anchoring respectively.

molecules resulting in different optical properties, see section 2.3.2.

Close to an interface DLCs can have two types of orientations with respect to the surface as illustrated in fig. 2.3. What kind of orientation is achieved strongly depends on the interaction between surface and molecules, e.g. the interfacial tension. Resulting from delocalized π -electrons the central aromatic core is the hydrophilic part of DLC molecules. This effect can be enhanced by attaching atoms with a large electronegativity, e.g. oxygen, see fig. 3.1, to the core. Hence, the long aliphatic side chains represent the hydrophobic part. Thus, close to an hydrophilic surface the molecules orient in a *homeotropic* (face-on) configuration, with their director \hat{n} perpendicular to the surface, see fig. 2.3(a). In contrast to that, near a hydrophobic surface, the molecules align *planar* with their director \hat{n} parallel to the surface with equal probability in all in-plane directions. If the director \hat{n} lies along one specific direction in the plane of the surface a *homogeneous* orientation (edge-on) is present, see fig. 2.3(b) [29].

2.1. Nematic-to-isotropic phase transition

Theoretically the isotropic to nematic phase transition has been described by many theories, e.g. the mean-field theory for hard rods and platelets discussed by Onsager [30]. However, the most successful one is the mean field theory developed by Maier and Saupe [31], see section 2.1.2. An expression of the systems free energy near the phase transition temperature is then given by Landau and de Gennes [32, 33], see section 2.1.3. Neglecting translational ordering these theories can be applied to smectic and columnar phases as well. Then the only characteristic distinguishing between an isotropic liquid and the liquid crystalline phase is the collective molecular ordering that can be quantified by an order parameter.

2.1.1. Order parameter

Most liquid crystalline systems are uniaxial with a rotational symmetry around one direction labeled director \hat{n} . In the liquid crystalline phase the molecules tend to align along this direction, that is arbitrary in space and imposed by weak intermolecular forces. In addition, \hat{n} and $-\hat{n}$ are not distinguishable [27]. To quantify the orientational differences between an isotropic liquid and liquid crystal an order parameter, that is non-zero in the liquid crystalline phase but vanishes in the isotropic phase, can be defined. The starting point of this definition can be on the microscopic molecular level or, since the molecular anisotropy manifests itself in measurable anisotropic physical properties, the macroscopic scale [27, 33].

For the microscopic approach assume a rod-like molecule with complete cylindrical symmetry around one molecular axis \vec{u} forming a nematic phase, see fig. 2.1. If the director \hat{n} points along the z -direction in a Cartesian laboratory frame (x, y, z) \vec{u} is defined with polar angles θ and ϕ [27]

$$u_x = \sin(\theta) \cos(\phi) \quad (2.1)$$

$$u_y = \sin(\theta) \sin(\phi) \quad (2.2)$$

$$u_z = \cos(\theta). \quad (2.3)$$

Then the molecular alignment can be described by a distribution function $\psi(\vec{u})$ of the molecular orientation with \vec{u} being a unit vector parallel (perpendicular) to the long axis (disk-shaped surface area) of the molecules in the nematic (columnar) phase, see figs. 2.1 and 2.2. This distribution function is normalized as [34]

$$\int d\vec{u} \psi(\vec{u}) = 1 \quad (2.4)$$

with $d\vec{u}$ being a surface element of sphere $\vec{u} = 1$. In the isotropic phase $\psi(\vec{u})$ is independent of \vec{u} and constant. In contrast to that, in the nematic phase $\psi(\vec{u})$ will point along the direction of \hat{n} and thus becomes anisotropic.

In polar coordinates $\psi(\theta, \phi)d\Omega$ then gives the probability of finding a molecule in an angle $d\Omega = \sin(\theta)d\theta d\phi$ around the direction (θ, ϕ) [27]. Since the nematic phase possesses complete rotational symmetry around \hat{n} , the distribution function is independent of ϕ , see fig. 2.4. The first non-zero¹ numerical parameter that characterizes the molecular alignment is given by the quadrupole of $\psi(\theta)$ [27]

$$S = \frac{1}{2} \langle (3 \cos^2(\theta) - 1) \rangle = \int \psi(\theta) \frac{1}{2} (3 \cos^2(\theta) - 1) / d\Omega. \quad (2.5)$$

¹The first moment $\langle \vec{u} \cdot \hat{n} \rangle$ equals zero since $\hat{n} = -\hat{n}$.

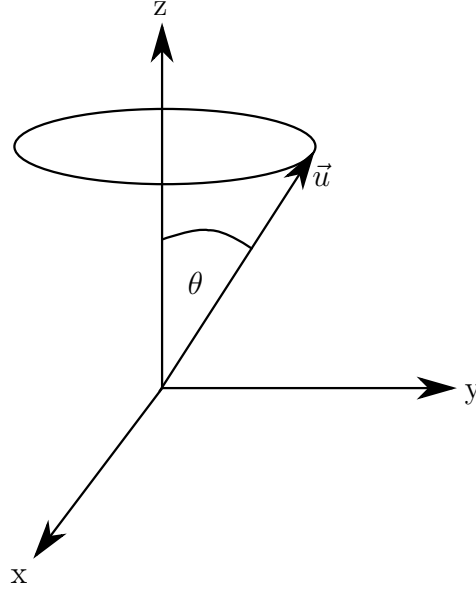


Figure 2.4.: For an oriented uniaxial liquid crystal the molecular axis \vec{u} rotates with an angle θ around the director \hat{n} (along z -direction). ϕ lies in the xy -plane.

The brackets $\langle \rangle$ represent thermal averaging. According to eq. (2.5) parallel alignment along \hat{n} ($\theta = 0$ and $\theta = \pi$) results in $\cos(\theta) = \pm 1$ and thus $S = 1$, while perpendicular alignment ($\theta = \pi/2$) results in $S = -1/2$. An entirely random orientation, as present in the isotropic phase, leads to $\langle \cos^2(\theta) \rangle = 1/3$ and thus $S = 0$. Hence, S is a measure of the orientational order.

A generalization of eq. (2.5) is given by [27]

$$S_{ij}^{\alpha\beta} = \frac{1}{2} \langle 3i_{\alpha}j_{\beta} - \delta_{\alpha\beta}\delta_{ij} \rangle \quad (2.6)$$

with $\alpha, \beta = x, y, z$ referring to the laboratory frame with three orthogonal unit vectors \vec{a}, \vec{b} and \vec{c} , Kronecker symbols $\delta_{\alpha\beta}, \delta_{ij}$ and $i, j = a, b, c$. The ordering matrix $S_{ij}^{\alpha\beta}$ is a symmetric tensor in ij and $\alpha\beta$ and traceless for $S_{ij}^{\alpha\alpha} = 0$ and $S_{ii}^{\alpha\beta} = 0$. Because of rotational symmetry around \hat{n} , here along the z -direction, $S_{ij}^{xx} = S_{ij}^{yy}$ and $S_{ij}^{xy} = 0$. Additionally, the xy -plane is a plane of reflection for the structure, so that $S_{ji}^{zx} = S_{ij}^{zy} = 0$. So all in all for a uniaxial nematic structure the only non-zero components in eq. (2.6) are [27]

$$S_{ij}^{zz} = -2S_{ij}^{xx} = -2S_{ij}^{yy} = S_{ji}. \quad (2.7)$$

Hence, the molecular alignment can be described by a symmetric and traceless (3x3) matrix S_{ji} .

2.1.2. Maier-Saupe theory

The Maier-Saupe theory describes the isotropic-to-nematic phase transition by evaluating the temperature dependence of the order parameter. Therefore, an interaction potential

that forces the molecules to align parallel to each other is assumed. In this mean-field approximation the interaction is assumed to result from dipole-dipole interactions of the anisotropic dispersion forces [31, 35]. Additionally, it is temperature independent and decreases with decreasing angle between neighbors [27]. Hence, the molecules are forced to align along the same direction. Liquid crystals exhibit change in volume with varying temperature. Keeping the pressure p fixed, the appropriate thermodynamic potential, that will be minimal in the equilibrium state and can best describe the phase transition, is the Gibbs free enthalpy per molecule or chemical potential $G(p, T)$ [27]. The chemical potential describing intermolecular effects assumed in this mean field theory is given by [27]

$$G_1 = -\frac{1}{2}U(p, T)S^2. \quad (2.8)$$

It is quadratic in S and decreases with increasing S , so that the interaction energy $U(p, T)$ is positive. Combining eq. (2.8) with the free enthalpy of the isotropic phase $G_i(p, T)$ the free enthalpy per molecule close to the phase transition temperature is given by [27]

$$G(p, T) = G_i(p, T) + k_B T \int \psi(\theta) \log(4\pi\psi(\theta)) d\Omega + G_1(p, T, S). \quad (2.9)$$

It depends on the distribution function $\psi(\theta)$ and the second term describes the decrease in entropy resulting from an additional anisotropic distribution in the liquid crystalline phase.

To find the equilibrium state eq. (2.9) can be minimized with respect to all variations of ψ that still satisfy eq. (2.4) [27]

$$\delta G = \lambda \int \delta\psi(\theta, \phi) d\Omega. \quad (2.10)$$

Combining eq. (2.5) and eq. (2.8) the variation of G_1 yields [27]

$$\delta G_1 = -US\delta S = -US \int \frac{1}{2}(3\cos^2(\theta) - 1)\delta\psi(\theta, \phi) d\Omega. \quad (2.11)$$

The variation of eq. (2.9) then results to [27]

$$\delta G = \int \delta\psi [k_B T \{\log(4\pi\psi) + 1\} - US(3\cos^2(\theta) - 1/2)] d\Omega \quad (2.12)$$

with

$$\log(4\pi\psi) = \lambda - 1 + \frac{US}{k_B T}(3\cos^2(\theta) - 1)/2. \quad (2.13)$$

Using the normalization constant [27]

$$Z = \int_0^1 \exp(mx^2) dx \quad (2.14)$$

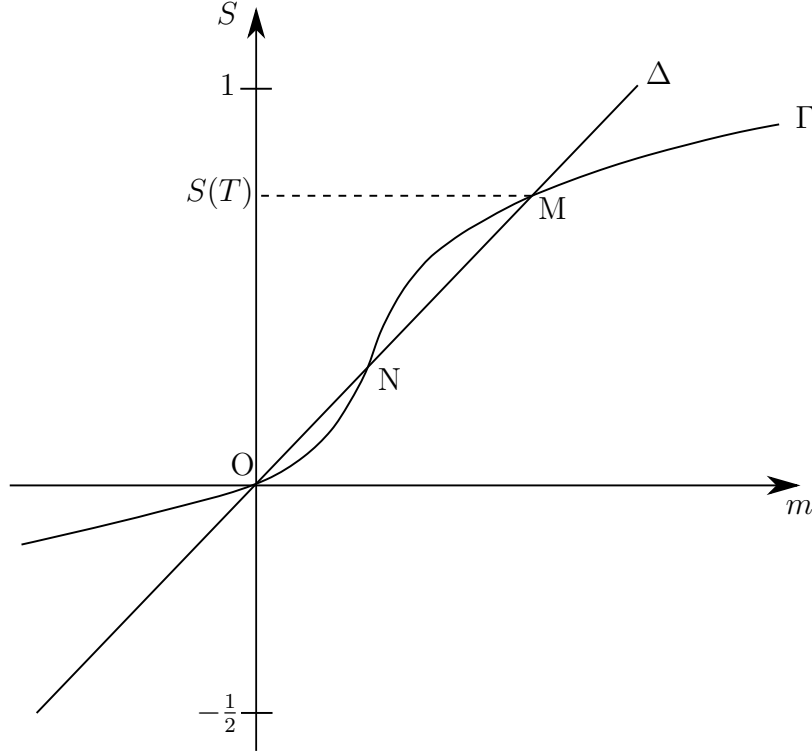


Figure 2.5.: Graphical solution of eqs. (2.16), (2.17) and (2.18) giving the order parameter $S(T)$ as a function of m defined in eq. (2.16). The slope of Δ is given by eq. (2.16) and the curve Γ is given by eqs. (2.17), (2.18) and (2.14). For $T < T_c$ Δ intersects with Γ at O, N (unstable) and M. The latter gives the physical state of minimum free enthalpy G . Inspired by [27].

the resulting form of the distribution function is [27]

$$\psi(\theta) = \exp(m \cos^2(\theta)) / 4\pi Z \quad (2.15)$$

with

$$m = \frac{3}{2}(US/k_B T). \quad (2.16)$$

Using eq. (2.5) a self-consistent equation for S can be expressed by [27]

$$S = -\frac{1}{2} + \frac{3}{2} \langle \cos^2(\theta) \rangle = -\frac{1}{2} + \frac{3}{2Z} \int_0^1 x^2 \exp(mx^2) dx \quad (2.17)$$

$$S = -\frac{1}{2} + \frac{3}{2} \frac{\partial Z}{Z \partial m} \quad (2.18)$$

By solving eqs. (2.16), (2.17) and (2.18) graphically, see fig. 2.5, the dependencies $S(T)$ and $m(T)$ can be extracted relative to a certain temperature [27]. In the isotropic phase at high temperature there is only one solution corresponding to $S = 0$. Below the isotropic to nematic phase transition, hence, for low temperatures, two solutions (point O and M) corresponding to local minima in the chemical potential exist². The one at $S = 0$ ($S \neq 0$)

²Other solutions may exist, e.g. point N in fig. 2.5. However, these are unstable states since they correspond to a maximum of the free enthalpy.

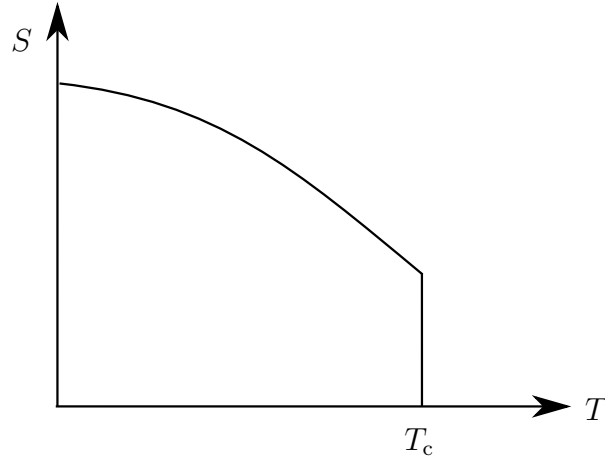


Figure 2.6.: Temperature evolution of the order parameter S for a thermotropic liquid crystal. Upon increasing temperature S vanishes discontinuously at the clearing temperature T_c typical for a first-order transition.

corresponds to the isotropic liquid (nematic phase). The nematic phase is the stable one if the temperature stays below a so called clearing temperature T_c defined by [27]

$$\frac{k_B T_c}{U(T_c)} = 4.55. \quad (2.19)$$

At T_c a first-order phase transition to the isotropic phase occurs. Hence, the nematic phase can appear as the temperature is lowered. The resulting temperature evolution of the order parameter S is plotted in fig. 2.6. Upon increasing temperature S vanishes discontinuously at the clearing temperature T_c typical for a first-order transition. Just below T_c the order parameter for all isotropic-nematic transitions is $S_c = S(T_c) = 0.44$ [27].

2.1.3. Landau-de Gennes theory

An expression of the free energy close to T_c can be calculated according to the Landau-de Gennes theory [33]. Assuming that the free energy solely depends on the temperature and order parameter it can be, for small S , expanded as a power series in S [34]

$$F(S, T) = a_0 + a_1(T)S + a_2(T)S^2 + a_3(T)S^3 + a_4(T)S^4 + \dots \quad (2.20)$$

By minimizing eq. (2.20) with respect to the order parameter $\frac{\partial F}{\partial S} = 0$, and thus determining its equilibrium value, solutions for varying temperatures can be found [34], see fig. 2.7. Similar as described in section 2.1.2 at $T > T_c$ only one stable state at $S = 0$ representing the isotropic state is present. At $T = T_c$ the free energy has three solutions, two minima and one maximum. The two minima equally stand for the isotropic and nematic state with a finite amount of order, hence, a coexistence of both states is

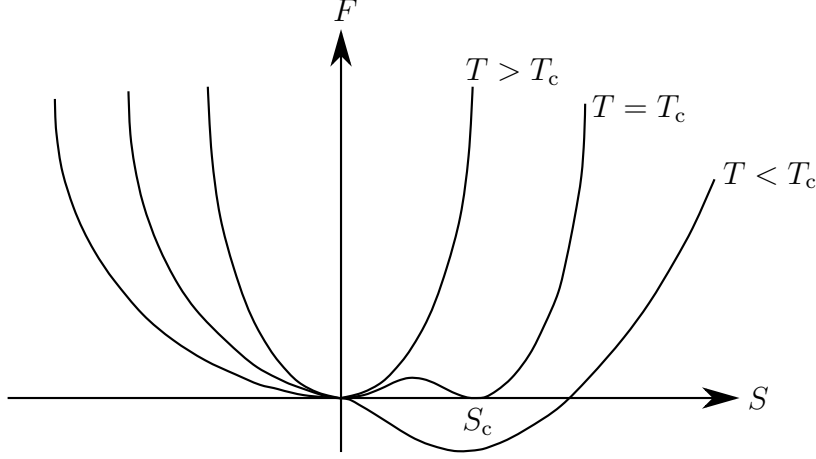


Figure 2.7.: Temperature dependence of the free energy as a function of the order parameter S . The absolute minimum at $S = 0$ for $T > T_c$ corresponds to the isotropic state. Upon decreasing temperature at $T = T_c$ the free energy $F(S, T)$ has three solutions, two minima and one maximum. The minimum at $S = 0$ ($S = S_c$) corresponds to the isotropic (nematic) state. Below T_c the local minimum at $S = 0$ becomes a local maximum. The isotropic state is unstable, only the nematic state is realized.

realized. Upon decreasing temperature the isotropic disordered state becomes unstable at T_c , solely the nematic state exists. Considering these solutions, assumptions about the terms in eq. (2.20) can be made [34]. The first term does not affect the transition and can be neglected. Below T_c the state at $S = 0$ changes from a local minimum to a local maximum of $F(S, T)$, hence, becomes unstable. In order for this to happen, the second term in eq. (2.20) must be zero, while $a_2(T) = A(T - T_c)S^2$. To make sure that its change of sign also changes that of $F(S, T)$ all following higher terms are considered constants, so that [34]

$$F(S, T) = \frac{1}{2}A(T - T_c)S^2 + \frac{1}{3}BS^3 + \frac{1}{4}CS^4 + \dots \quad (2.21)$$

The important difference between the nematic transition compared to e.g. the magnetic transition is that it is discontinuous. This difference manifests itself in the discontinuous temperature dependence of the order parameter, see fig. 2.6. In contrast to that, the magnetic moment M , being the order parameter of the magnetic transition, changes continuously. Additionally, the magnetic moments M and $-M$ represent equal states, since the free energy is an even function in M . Hence, the second term in eq. (2.21) must be zero. For the nematic transition S and $-S$ represent different states. For $S > 0$ the molecules align parallel to one direction, while they orient perpendicular to that for $S < 0$. In order for this to happen, the second term in eq. (2.21) is not equal to zero. Hence, the free energy in eq. (2.21) is characteristic for an order-disorder transition with a discontinuous change in the order parameter resulting in a first-order transition.

2.2. Confinement effects

Embedding liquid crystals into porous matrices with extreme spatial confinement various effects regarding the phase transition temperature, see section 2.2.2, structural reorientations or surface effects have to be considered. As confining hosts porous membranes with straight cylindrical pores with pore radius r described in detail in section 3.1.2 are used in this thesis.

One may assume that the continuum theories given in sections 2.1.2 and 2.1.3 do not apply to liquid crystals in complex geometries on the nanoscale. However, as shown for many soft matter systems in confinement this is, by making adjustments to e.g. the free energy given in eq. (2.21), indeed still the case [36–39].

For nematic rod-like liquid crystals confined in pores of only a few nanometer the free energy in eq. (2.21) has to be adapted. Following the theoretical work by refs. [40, 41] and experiments performed by ref. [42] the model by Kutnjak, Kralj, Lahajnar, and Zumer (KKLZ model) considers a nematic ordering field σ and a parameter κ representing effects due to surface-induced deformations [43–46]. The nematic ordering field then depends on the molecular anchoring strength at the pore surface and is inversely proportional to the size of the confining space. Resulting from a bilinear coupling between order parameter and nematic ordering field a term lowering the free energy is introduced. Hence, an upward shift of the phase transition temperature resulting in a pretransitional paranematic state is possible. It is opposed by a term representing the disorder effects at the surfaces. The resulting addition to the Landau de Gennes free energy is then given by [45]

$$F_{\text{conf}} = -S\sigma + S^2\kappa. \quad (2.22)$$

Hence, the shift of the nematic-to-paranematic transition in confinement is determined by a competition of two opposite contributions. Minimizing this modified free energy with respect to the order parameter yields a critical nematic ordering field. Above that value the phase transition changes from discontinuous to continuous.

By embedding DLCs into cylindrical pores from a few up to a few dozen nanometer similar effects are present. The pore surfaces either enforce edge-on or face-on anchoring of the molecules depending on the surface chemistry, see fig. 2.3. Upon confining DLCs with a columnar hexagonal phase Col_h in these matrices, molecular structures that are absent in the bulk state can be generated, see fig. 2.9. These structures and the resulting distortions giving rise to the free energy of the system are discussed in detail in the following section.

2.2.1. Distortion free energy

External forces imposed by geometric constraints can significantly act on the molecules position rendering the ideal conformation impossible. Thus, in a realistic situation the

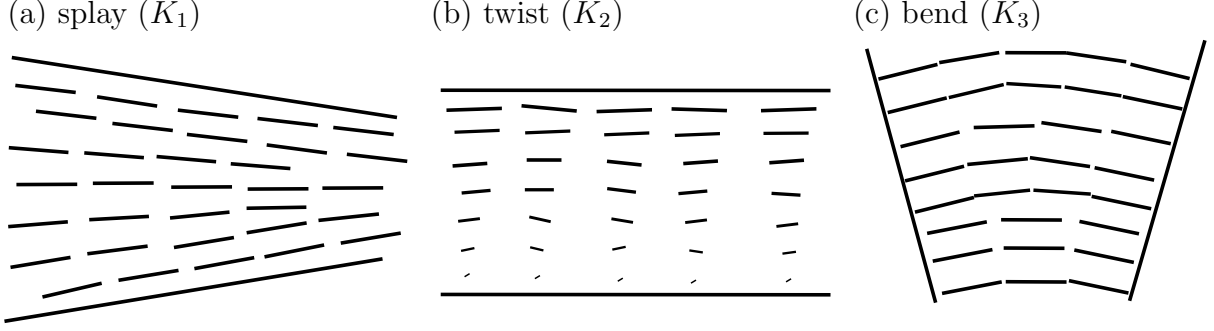


Figure 2.8.: Examples of spatial distortions of the director \hat{n} : splay ($\vec{\nabla} \cdot \hat{n} \neq 0$), twist ($\vec{\nabla} \times \hat{n} \neq 0$) and bend ($\hat{n} \times (\vec{\nabla} \times \hat{n}) \neq 0$) distortions.

order parameter defined in eq. (2.5) is not independent of the molecules position \vec{r} . It varies from point to point resulting in distortions of the molecular alignment. Deformations in the order parameter occur over distances that are much larger than the molecular dimensions. Thus, they can be described using a continuum theory neglecting structural details on the molecular scale [47, 48]. As a result, for nematic liquid crystals without translational ordering, the distortion energy F_d has to be added to the free energy density defined in eq. (2.21). This addition must be an even function in \hat{n} and can be expanded in a power series of $\nabla \hat{n}$ [27]

$$F_d = \frac{1}{2}K_1(\vec{\nabla} \cdot \hat{n})^2 + \frac{1}{2}K_2(\hat{n} \cdot \vec{\nabla} \times \hat{n})^2 + \frac{1}{2}K_3(\hat{n} \times \vec{\nabla} \times \hat{n})^2. \quad (2.23)$$

The Frank elastic constants $K_{1,2,3}$ respectively represent the resistance of a liquid crystal to one of three spatial variations in \hat{n} shown in fig. 2.8; the splay, twist and bend deformation. Each constant must be positive. Otherwise the undisturbed state would not correspond to a minimum of free energy.

For DLCs the splay, bend or twist deformations can be described by a two-dimensional displacement field \vec{u} . Gradients in \vec{u} change the free energy, but first-order derivations along the liquid direction (z -axis), hence, along the columns, are merely rotations of the system. Only second-order derivatives along the liquid direction can enter the free energy. Variations of $\vec{u}(\vec{r})$ in the vicinity of \vec{r} lead to the distortion free energy for DLCs [24, 27]

$$\begin{aligned} F_d = & \frac{1}{2}\bar{B} \left(\frac{\partial u_x}{\partial x} + \frac{\partial u_y}{\partial y} \right)^2 + \frac{1}{2}C \left[\left(\frac{\partial u_x}{\partial x} - \frac{\partial u_y}{\partial y} \right)^2 + \left(\frac{\partial u_x}{\partial y} + \frac{\partial u_y}{\partial x} \right)^2 \right] \\ & + \frac{1}{2}K_3 \left[\left(\frac{\partial^2 u_x}{\partial z^2} \right)^2 + \left(\frac{\partial^2 u_y}{\partial z^2} \right)^2 \right]. \end{aligned} \quad (2.24)$$

The last term represents bending of the columns, see fig. 2.8(c). The first term describes a radial compression or dilation, while the second term corresponds to shearing of the columns. The splay and twist elastic constants $K_{1,2}$ are combined in the compression and

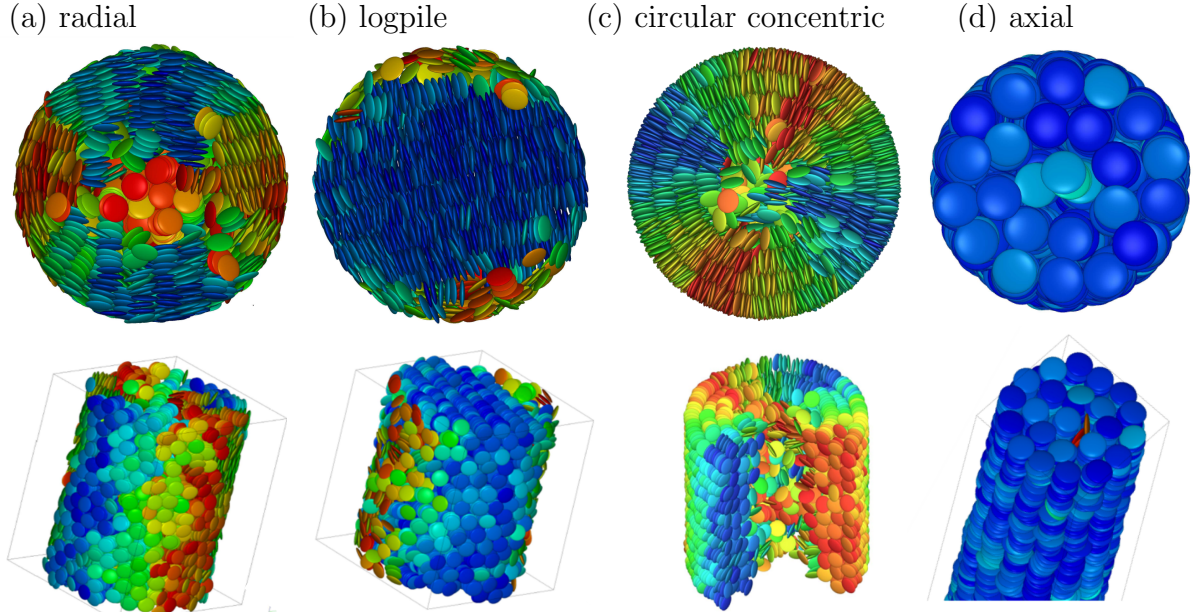


Figure 2.9.: Top and side view of possible configurations of DLCs embedded in a straight cylindrical pore with a diameter on the nanoscale. Images extracted from Monte Carlo simulations and adapted with permission from [49] Copyright American Physical Society 2018 for subframe (c) and from [50] for subframe (a,b,d).

shear moduli \bar{B} and C [24].

Close to a hydrophilic surface face-on anchoring of the molecules with their director perpendicular to the pore wall and perpendicular to the long pore axis is the energetically favored configuration and can lead to either a *logpile* or *radial* configuration, see fig. 2.9(a,b). The occurrence of either of them strongly depends on the size of the confinement [20, 21, 25].

For cylindrical pores of a few nanometer a nematic, radial discotic state without translational order is present. This configuration is absent in the bulk state and characterized by a molecular stacking along the pore radius, see fig. 2.9(a). No twist and bend distortions are present. Hence, the last two terms in eq. (2.23) equal zero. The only contribution to the distortion free energy results from splay distortions that are highest in the pore center resulting in an isotropic core. These splay distortions decrease with increasing distance r from the pore center. The additional contribution to the Landau-de Gennes free energy in eq. (2.21) then reads [20]

$$F_{\text{splay}} = \frac{1}{2} b_1 (\vec{\nabla} \hat{n})^2 S^2 = \frac{b_1}{A} \frac{1}{r^2} S^2 \quad (2.25)$$

with b_1 representing a coupling constant, pore radius r and A being the same Landau-de Gennes free energy expansion coefficient as in eq. (2.21). Increasing the confining size to a few dozen nanometer or even several micrometer results in the logpile configuration, see fig. 2.9(b) [25]. The molecules stack up into straight uniaxial columns forming a single domain structure, see fig. 2.9(a). To preserve the surface anchoring to the sides of the

domain either an isotropic layer close to the pore wall, resulting in lattice irregularities, or splayed columns in the vicinity of the pore wall are possible [25]. Besides that no significant distortions are present.

A hydrophobic surface favors edge-on anchoring of the molecules with their director parallel to the pore wall. Is the director still perpendicular to the long pore axis a *circular concentric* configuration forming supermolecular ring structures absent in the bulk state is present, fig. 2.9(c). The distortion energy solely results from bending of the columns with bending radius r_b . Hence, the first two terms in eq. (2.24) equal zero. The geometric constraints and thus the bend distortion is highest in the pore center resulting in an isotropic core similar as in the radial configuration. The last term in eq. (2.24) then reads [24]

$$\left(\frac{\partial^2 u_x}{\partial z^2}\right)^2 + \left(\frac{\partial^2 u_y}{\partial z^2}\right)^2 = \frac{1}{r_b^2}. \quad (2.26)$$

The resulting distortion energy per unit length of a pore then results to [24]

$$F_{\text{bend}} = \pi K_3 \int_a^r \frac{1}{r_b^2} r dr = \pi K_3 \ln\left(\frac{r}{a}\right) \quad (2.27)$$

with pore radius r and lattice parameter a of the hexagonal phase.

In contrast to that, when the molecules stack up into columns with their director parallel to the pore axis and parallel to the pore walls the *axial* configuration is present, see fig. 2.9(d). Then the last term in eq. (2.24) vanishes since no bending of the columns is present. The first two terms can be estimated by an effective lattice distortion at the pore wall equally distributed over all columns fitting inside the pore. Assuming that in the Col_h phase two hexagonal domains $\{100\}$ and $\{110\}$ with different surface tensions σ are present, a surface term including splay and twist distortions can be expressed as [24]

$$F_{\text{axial}} = B_{\text{axial}} a^2 + 2\pi r \left(\frac{1}{2} \sigma_{(100)} + \frac{1}{2} \sigma_{(110)} \right). \quad (2.28)$$

B_{axial} is a constant with the same order of magnitude as \bar{B} and C in eq. (2.24). Since the axial configuration is proportional to r but the circular concentric configuration proportional to $\ln(r)$, see eq. (2.27), pores with a radius larger than a critical radius r_c favor the circular concentric orientation.

2.2.2. Capillary melting and freezing

Capillary freezing and melting of a liquid can be directly applied to the liquid to liquid crystalline phase transition of liquid crystals. Consider a capillary with radius r filled with a vapor of relative vapor pressure p/p_0 and its liquid, see fig. 2.10(a). This coexistence is

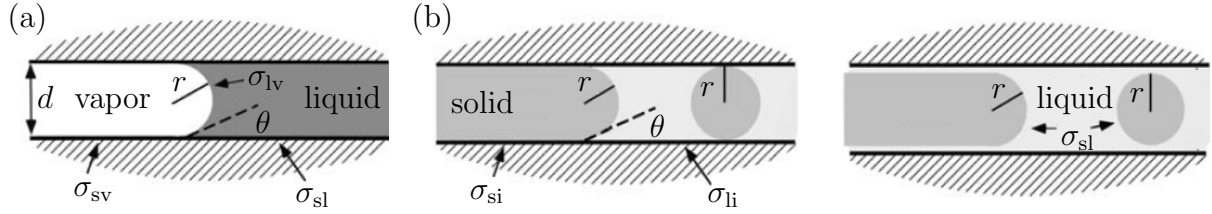


Figure 2.10.: (a) Schematic illustration of the coexistence of a liquid and its vapor in a pore with diameter d , radius r of the curved liquid-vapor with surface tension σ_{lv} , contact angle θ of the liquid at the pore surface and surface tension of the vapor-solid and liquid-solid interface σ_{sv} and σ_{sl} . (b) Solid to liquid transition with solid-substrate and liquid-substrate surface tension σ_{si} and σ_{li} . In this case, r gives the radius of the solid sphere or solid cylindrical plug. In the right panel a non-freezing layer exists between solid and substrate. Adapted and reprinted with permission from [52]. Copyright IOP Publishing 2001.

described by Laplace's equation [51]

$$p'' - p' = \frac{2\sigma_{lv}}{r} \quad (2.29)$$

with radius r of the curved liquid-vapor interface. Thereby the pressure differences of the normal pressures p'' and p' in the liquid and vapor phase across the curved liquid-vapor interface with surface tension σ_{lv} are considered. The relation between the surface tension of the solid-vapor phase σ_{sv} , the solid-liquid interface σ_{sl} and σ_{lv} is given by Young's equation [52]

$$\sigma_{sv} = \sigma_{sl} + \sigma_{lv} \cos(\theta). \quad (2.30)$$

Assuming that the contact angle θ of the liquid on the pore surface is less than 90° , the radius r in eq. (2.29) is given by the Kelvin equation [52]

$$r = \frac{\sigma_{lv} v_{ml}}{k_B T \ln(p/p_0)} \quad (2.31)$$

with molecular volume v_{ml} of the liquid, temperature T and Boltzmann constant k_B .

This reduction in pressure over the concave liquid meniscus in a pore has a direct impact on the solid (liquid crystalline)-liquid transition, see p - T phase diagram in fig. 2.11. It shifts the intersection of the vapor pressure-temperature curve of the confined liquid with that of bulk solid towards lower temperatures. Hence, the confined liquid coexists with the bulk solid at temperature below the bulk melting temperature T_{bulk} . The capillary held solid can have either an enhanced or lowered vapor pressure depending on the curvature of the solid-liquid interface and thus the wetting properties of the liquid. Hence, the pressure shift can result in a reduced or enhanced equilibrium point of capillary held solid and liquid. The vapor pressure as function of the temperature is given by the Clausius-Clapeyron equation [53]

$$\frac{dp}{dT} = \frac{\Delta S}{\Delta V} = \frac{Q_m}{T \Delta V} \quad (2.32)$$

with molar evaporation heat Q_m and difference of liquid and gas molar volume $\Delta V =$

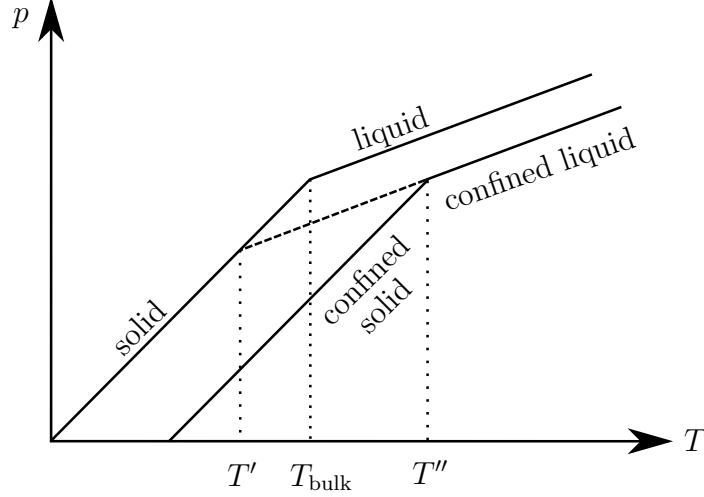


Figure 2.11.: Comparison of the confined solid-vapor and liquid-vapor equilibrium line in a p - T phase diagram for the bulk and confined system. The dashed line indicates the metastable extension of the isotropic liquid in confinement for $T < T''$. The dotted lines give the respective phase transition temperatures. Inspired by [54].

$v_{\text{mg}} - v_{\text{mf}}$. Correlating this equation with eq. (2.31), by assuming that the radius of the curved liquid-vapor interface is, to good approximation, equal to the pore radius, the melting point depression/enhancement for a cylindrical pore with radius r [51, 54]

$$\Delta T = T_{\text{bulk}} - T_{\text{pore}}(r) = -\frac{T_{\text{bulk}}}{\Delta H} \frac{2}{r} (v_{\text{ml}}\sigma_1 - v_{\text{sl}}\sigma_s). \quad (2.33)$$

where ΔH is the latent heat of melting, $v_{\text{ml/ms}}$ the molar volumes of the liquid/solid and $\sigma_{1/s}$ the corresponding surface energies. Assuming that the solid is wetted by its own melt, i. e. $\sigma_s - \sigma_1 = \sigma_{\text{sl}}$, and neglecting the change in molar volume at T_{bulk} , eq. (2.33) simplifies to the Gibbs-Thompson equation [52, 55, 56]

$$\Delta T = T_{\text{bulk}} \frac{4\sigma_{\text{sl}}}{\Delta H \rho d} \quad (2.34)$$

with density ρ and pore diameter d . The contact angle between liquid-solid (liquid crystal) is assumed to be 180° implying that the solid is separated from the pore surface by a non-freezing layer, see fig. 2.10(b) [57]. In addition, it is assumed that σ_{sl} is isotropic and ΔH and ρ_s maintain their bulk properties. The possibility of the failure of these assumption in strong confinement has to be kept in mind.

Equation (2.34) describes the decrease of phase transition temperature of DLCs in confinement compared to bulk as the pore diameter, hence, the confining space, gets smaller. In restricted geometries of a few nanometers solely inducing splay distortion described by eq. (2.25) an additional term proportional to d^{-2} has to be added to eq. (2.34) [20].

The in section 2.2.1 discussed various orientational configurations and effects on the phase transition temperature in confinement discussed above can be used to control and optimize anisotropic material specific parameters characteristic for DLCs. These anisotropic

properties in particular the dielectric and optical anisotropy will be discussed in detail in the next section.

2.3. Anisotropic properties

The anisotropy of a material reveals itself in anisotropic physical properties, that can be measured e. g. by the interaction with an electromagnetic wave with electric and magnetic field vectors \vec{E} and \vec{B} . These are perpendicular to each other and to the direction of propagation z , that is in turn perpendicular to the planes spanned by \vec{E} and \vec{B} in the xy -plane. The moment-by-moment direction of \vec{E} is called polarization, that depends on the phase shift δ of the two orthogonal components of \vec{E} with amplitudes $a_{1,2}$, wave vector \vec{k} and angular frequency ω , see fig. 2.12, [58]

$$\vec{E}_x(z, t) = a_1 \cos(\vec{k}z - \omega t) \quad (2.35)$$

$$\vec{E}_y(z, t) = a_2 \cos(\vec{k}z - \omega t + \delta) \quad (2.36)$$

For e. g. $\delta > 0$ \vec{E}_y lags behind \vec{E}_x . In general, the electric field changes its amplitude and direction continuously resulting in an elliptical trace, that is to say elliptical polarized light. Linear polarized light results from a phase difference $\delta = m\pi$ for $m = 0, 1, 2, \dots$, see fig. 2.12. The electric field and propagation vector lie in the so called plane-of-vibrations. If both components in eqs. (2.36) and (2.35) have identical amplitudes and $\delta = (2m+1)\pi/2$ for $m = 0, 1, 2, \dots$ the \vec{E} -vector makes one complete rotation as the wave advances through one wavelength. The light is circular polarized. These two cases may be considered special cases of elliptically polarized light.

2.3.1. Dielectric anisotropy

Applying an electric field \vec{E} to a dielectric material results in a polarization density \vec{P} of the permanent and induced electric dipole moment [29]

$$\vec{P} = \varepsilon_0 \chi^e \vec{E} \quad (2.37)$$

with electric susceptibility χ^e and permittivity in vacuum ε_0 . Depending on the strength of ε , defining the response of the material to the electric field, the charge distribution is shifted inducing electric dipoles resulting in a electric displacement field \vec{D} [59]

$$\vec{D} = \varepsilon_0 \vec{E} + \vec{P}. \quad (2.38)$$

In the isotropic phase is $\vec{P} \parallel \vec{D}$, so that the susceptibility is a scalar quantity. In the anisotropic liquid crystalline phase \vec{P} is not necessarily parallel to \vec{D} . The susceptibility

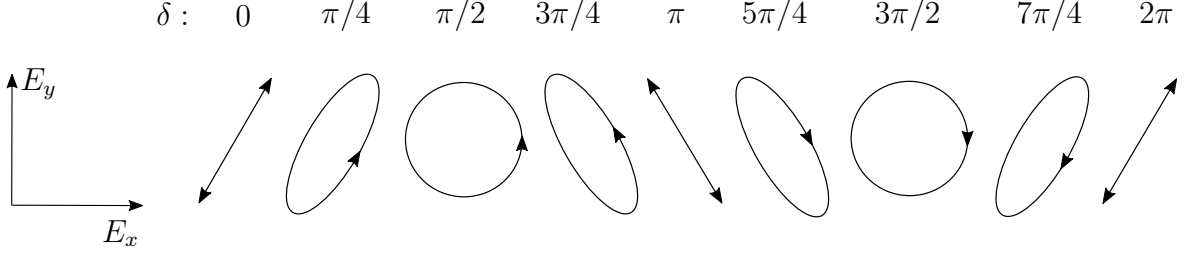


Figure 2.12.: For a phase difference $\delta > 0$ E_y lags behind E_x . Depending on δ either linear, circular or elliptical polarized light is present. When amplitudes $a_1 = a_2$ the light is circular polarized for $\delta = (2m + 1)\pi/2$. Inspired by [58].

is a symmetric and diagonal tensor of rank two. If the director \hat{n} is chosen to be along the z -axis that tensor reads [29]

$$\chi^e = \begin{pmatrix} \chi_{\perp}^e & 0 & 0 \\ 0 & \chi_{\perp}^e & 0 \\ 0 & 0 & \chi_{\parallel}^e \end{pmatrix}. \quad (2.39)$$

The induced polarisation \vec{P} now depends on the direction of the applied field relative to the symmetry axes of the liquid crystal. In an uniaxial system the susceptibility χ_{\parallel}^e parallel to the director \hat{n} differs compared to the susceptibility χ_{\perp}^e perpendicular to it. Considering a more general form, where the director \hat{n} forms an angle θ with the z -axis and lies in the yz -plane, eq. (2.39) transforms to [29]

$$\chi^e = \begin{pmatrix} \chi_{\perp}^e & 0 & 0 \\ 0 & \chi_{\perp}^e \cos^2(\theta) + \chi_{\parallel}^e \sin^2(\theta) & (\chi_{\parallel}^e - \chi_{\perp}^e) \sin(\theta) \cos(\theta) \\ 0 & (\chi_{\parallel}^e - \chi_{\perp}^e) \sin(\theta) \cos(\theta) & \chi_{\perp}^e \cos^2(\theta) + \chi_{\parallel}^e \sin^2(\theta) \end{pmatrix}. \quad (2.40)$$

The difference in the susceptibilities appearing in the off-diagonal terms yields the susceptibility anisotropy that is proportional to the order parameter S [29]

$$\Delta\chi^e = \chi_{\parallel}^e - \chi_{\perp}^e. \quad (2.41)$$

By placing such an anisotropic dielectric material between two plates of a capacitor its capacitance increases resulting from the dielectric permittivity ε of the liquid crystal. The dielectric permittivity ε is related to χ^e by [29]

$$\varepsilon = I + \chi^e \quad (2.42)$$

with I being a unit 3×3 matrix. The capacitance measurement will yield a value ε_{\parallel} (ε_{\perp}) when the director \hat{n} is parallel (normal) to the capacitors plates. The dielectric

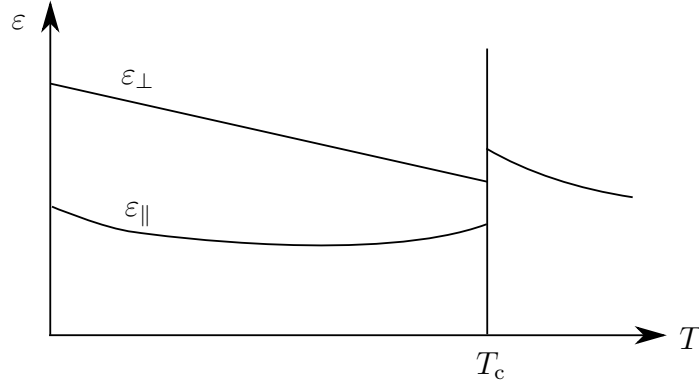


Figure 2.13.: Temperature dependence of the dielectric permittivity parallel ε_{\parallel} and perpendicular ε_{\perp} to the applied electric field for a thermotropic liquid crystal with $\Delta\varepsilon < 0$. When the temperature reaches the clearing temperature T_c the anisotropy vanishes. Inspired by [28].

anisotropy [29]

$$\Delta\varepsilon = \varepsilon_{\parallel} - \varepsilon_{\perp} \quad (2.43)$$

may be positive or negative depending on which direction is more easily to polarize [27]. In DLCs this direction is oriented perpendicular to the unit vector \vec{u} , see fig. 2.2(a), and thus lies in the plane of the disk shaped molecules. The molecule can be easily polarized by an electric field along this direction. In contrast to that, a field parallel to \vec{u} only weakly polarizes the molecule. Thus for DLCs $\varepsilon_{\parallel} < \varepsilon_{\perp} \Rightarrow \Delta\varepsilon < 0$. An exemplary plot of the dielectric permittivity as a function of the temperature is plotted in fig. 2.13. The anisotropic behavior vanishes at T_c .

2.3.2. Optical anisotropy

In an isotropic non-magnetic medium the refraction index n of light depends on the dielectric permittivity [59]

$$n = \sqrt{\varepsilon} = \frac{c}{v} \quad (2.44)$$

with speed of light c and velocity v . Resulting from eq. (2.43) anisotropic materials have two refraction indices, $n_{\perp} = \sqrt{\varepsilon_{\perp}}$ and $n_{\parallel} = \sqrt{\varepsilon_{\parallel}}$. This effect is also known as double refraction or linear birefringence.

Consider an electric field \vec{E} with two components linear polarized perpendicular/parallel to the optical axis, traversing a birefringent sample, see fig. 2.14. The optical axis is the direction along which the material behaves as if it was isotropic. Each plane containing this direction is called principal plane. In general, a wave traversing a birefringent sample is divided into two emerging beams, the ordinary and extraordinary beam³. The component polarized perpendicular to this plane and thus the optical axis “sees” the so

³For a very thin sample having a small anisotropy both beams still overlap and can thus interfere. This fact is utilized in the optical polarimetry measurements described in section 3.2.2.

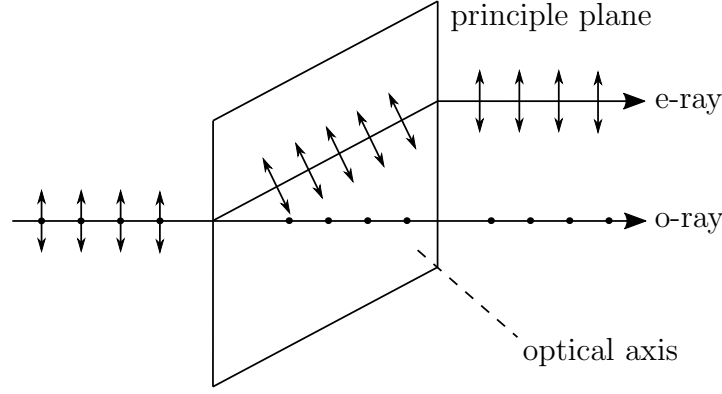


Figure 2.14.: Light with two orthogonal field components traversing a birefringent sample. The parallelogram marks the principal plane including the optical axis. The extraordinary beam (e-ray) sees n_{\parallel} , while the ordinary beam (o-ray) sees n_{\perp} . Inspired by [58].

called ordinary refraction index $n_o = n_{\perp}$. According to eq. (2.44) these waves expand into the crystal in all directions with speed v_{\perp} . In contrast to that, waves polarized in plane of the principal plane have a perpendicular and parallel component with respect to the optical axis. The part polarized parallel to the optical axis “sees” the extraordinary refraction index $n_e = n_{\parallel}$ and thus propagates with velocity v_{\parallel} . Birefringence is defined as the difference between ordinary and extraordinary refractive index [29]

$$\Delta n = n_e - n_o. \quad (2.45)$$

Combining eq. (2.44) and eq. (2.45) the ordinary (extraordinary) beam travels faster than the extraordinary (ordinary) if $\Delta n > 0$ ($\Delta n < 0$). Thus, depending on the sign of the dielectric anisotropy in eq. (2.43) the sample is either an optical positive or negative sample.

Splitting up the components of the dielectric permittivity, and hence the refractive index, in Cartesian coordinates gives the ellipsoid of wave normals also known as optical indicatrix [59]

$$\frac{x^2}{n_x^2} + \frac{y^2}{n_y^2} + \frac{z^2}{n_z^2} = 1. \quad (2.46)$$

The length of its principal axes yield the refraction indices along the corresponding direction. For isotropic materials the indicatrix turns into a circle, or in three dimensions into a sphere, since the propagation speed, and hence the refraction index, is identical in every direction. It is oblate for optical negative and prolate for optical positive birefringent materials. Along the optical axis light propagates with velocity v_o , hence, experiences n_o . In the xy -plane perpendicular to z it travels with v_e , hence, experiences n_e . Thus, the indicatrix contains bivalve areas [60]

$$\left(\frac{x^2 + y^2 + z^2}{n_o^2} - 1 \right) \left(\frac{x^2 + y^2}{n_e^2} + \frac{z^2}{n_o^2} - 1 \right) = 0 \quad (2.47)$$

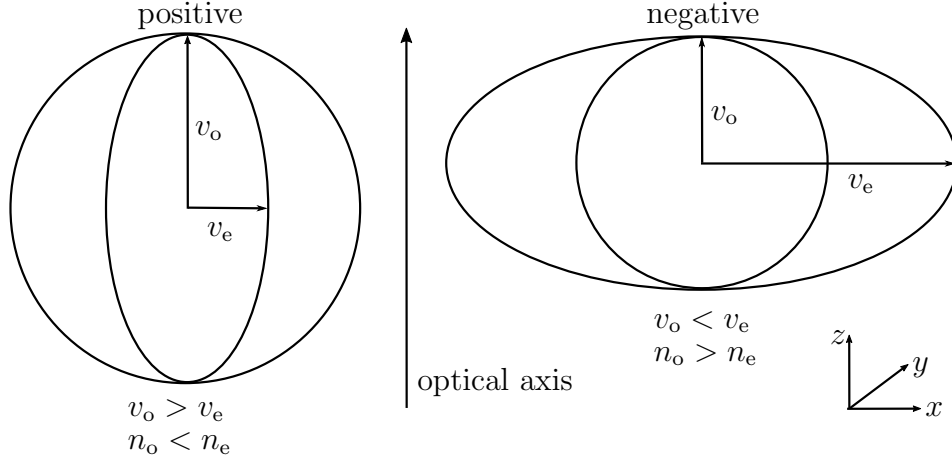


Figure 2.15.: Phase velocity surfaces, see eq. (2.47), for an optical positive or negative uniaxial crystal giving the refractive indices $n_o = v_o^{-1}$ and $n_e = v_e^{-1}$.

illustrated in fig. 2.15. Taking a principal plane containing the optical axis, e.g. the xz -plane and thus $y = 0$ eq. (2.47) yields [60]

$$x^2 + z^2 = n_o^2 \quad (2.48)$$

$$\frac{x^2}{n_e^2} + \frac{z^2}{n_o^2} = 1 \quad (2.49)$$

and hence a circle with radius n_o for the ordinary beam and an ellipse with principal axes n_e and n_o for the extraordinary beam. In contrast to that choosing a plane perpendicular to the optical axis, and thus $z = 0$, results in two concentric circles with radius n_o (n_e) for the ordinary (extraordinary) beam [60]

$$x^2 + y^2 = n_o^2 \quad (2.50)$$

$$x^2 + y^2 = n_e^2. \quad (2.51)$$

Refractive indices along a direction tilted by an angle θ with respect to the optical axis can be calculated in accordance with eq. (2.40) by [60]

$$n = \frac{n_e n_o}{\sqrt{n_e^2 \cos^2(\theta) + n_o^2 \sin^2(\theta)}}. \quad (2.52)$$

3. Materials & techniques

The following chapter describes in detail the used materials, i.e. the discotic liquid crystal and confining hosts, as well as the utilized measurement techniques. The sample preparation, optical polarimetry and X-ray diffraction measurements, see section 3.2, are explained in detail. Experimental techniques used to characterize the samples, see section 3.1, are only addressed briefly.

3.1. Sample characteristics

3.1.1. Discotic liquid crystal

The thermotropic DLC 2,3,6,7,10,11-hexakis[hexyloxy]triphenylene (HAT6) was purchased from SYNTHON Chemicals GmbH & Co. KG. Its synthesis is described in ref. [61]. It consists of a triphenylen core linked by six oxygen atoms to surrounding flexible alkyl chains ($\text{C}_{54}\text{H}_{84}\text{O}_6$), see fig. 3.1, resulting in a molar mass of $m_{\text{mol}} = 829.21 \text{ g/mol}$. In its bulk state HAT6 shows a Col_h phase inbetween 372 K and 342 K [62]. Next to the π - π -interaction, being the driving force for the molecular custom-assembly into columns, van-der-Waals forces are the dominant intermolecular interactions [63]. While the alkyl tails prefer to stay close to the aromatic cores, the rotation of the cores with respect to each other is limited. They tend to slide over each other into positions where the aromatic rings are superimposed to each other [64]. However, slow diffuse rotations on the

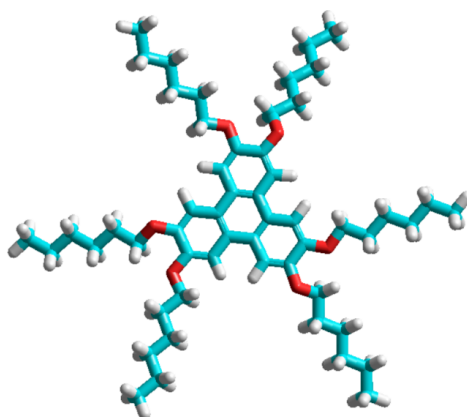


Figure 3.1.: Chemical structure of HAT6 including carbon (turquoise), hydrogen (white) and oxygen (red) atoms. Reprinted with permission from [49]. Copyright American Physical Society 2018.

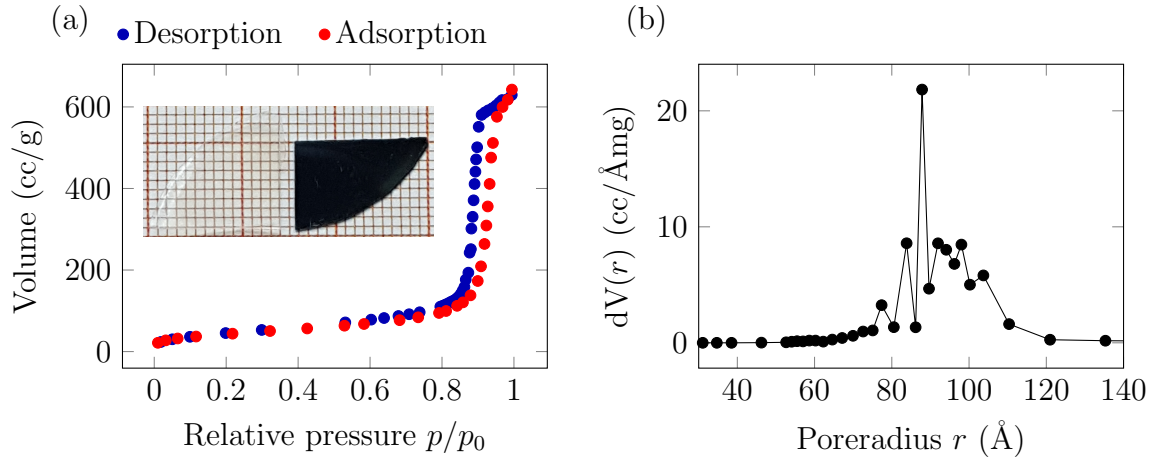


Figure 3.2.: (a) Volumetric nitrogen sorption isotherm of pSiO₂ showing the N₂ filling degree as a function of the relative pressure p/p_0 . Inset: Photograph of an optical transparent pSiO₂ membrane (left) prepared by thermal oxidation of pSi (right). (b) Pore size distribution showing the variation of the measured pore volume as a function of the pore radius.

nanosecond scale are possible. As determined from XRD measurements the molecule is about 0.3 nm thick and has a diameter of 1.8 nm leading to a hexagonal lattice constant of $a = 2.11$ nm [24, 62]. Its density can then be determined to $\rho = 1527.5$ kg/m³.

3.1.2. Confining hosts

In this study mesoporous silica (pSiO₂) as well as meso- and macroporous¹ anodized aluminum oxide (AAO) are used as confining hosts, hereinafter called membranes. The pores are assumed to be cylindrical. However, deviations due to surface roughness and meandering of the pores are realistic. Specifications of each membrane type discussed in detail in this section can be found in table A.1 in appendix A.

Mesoporous silica

Highly p-doped <100> silicon wafer with a resistivity of $R = 0.01 - 0.02$ Ωcm in combination with an electrolyte consisting of 40 % hydrofluoric acid (48 % concentrated) and 60 % ethanol are used to fabricate pSiO₂ [66–69]. Resulting from oxidation processes a passivating SiO₂ layer on top of the wafer necessitates the use of hydrofluoric acid. Its large electronegativity enables splitting of the strong Si-O bonds and thus dissolution of the passivating layer. Afterwards hydrogen atoms protect the surface from further nucleophilic attacks. A current density of $J = 13.3$ mA/cm² running from the anode (wafer) to a platinum electrode is applied. This current results in migration of holes towards the surface generating a series of nucleophilic attacks as described in detail in [70]. As a result

¹According to the IUPAC convention porous solids can be classified into microporous (pore diameter $d < 2$ nm), mesoporous ($2 \text{ nm} < d < 50$ nm) and macroporous ($d > 50$ nm) [65].

a silicon atom is dissolved from the surface. This changes the surface geometry leading to an enhanced electric field in this region increasing the current density and thus the tunnel probability of the charge carriers. The lateral dimensions of the pore walls lead to the quantum wire effect resulting in the formation of parallel pores with their axis perpendicular to the wafer surface [68]. The electrochemical process is stopped after an etching time of 8 h. Therefore, the current density is increased, so that the 360 μm porous silicon (pSi) layer is removed from the wafer via electrolytic polishing. Afterwards not only the surface, but the entire pSi volume, is thermally oxidized at 800 $^{\circ}\text{C}$ for 48 h resulting in an optical transparent membrane, see inset in fig. 3.2(a). Thereby the temperature is slowly increased and subsequently decreased with 0.3 K/min to prevent cracking. Nevertheless, the membranes and thus the pores exhibit a small curvature up to a few degrees, see fig. 3.3.

To determine the pore diameter and porosity, volumetric N_2 sorption isotherms² are performed measuring the adsorption and subsequent desorption of N_2 molecules. For statistics multiple measurements are performed on each membrane. The measurement starts with an empty sample in an evacuated aperture. The isotherm shown in fig. 3.2(a) shows a typical behavior for a sample with a mesoporous morphology. Plotted is the adsorbed N_2 volume as a function of the relative pressure p/p_0 , where p_0 is the saturation vapor pressure of the gas. In order to measure the adsorption part (red line) the gas pressure is subsequently increased up to $p/p_0 = 1$. After an adsorption of a single monolayer, N_2 multilayers form on the surface. A strong increase in the absorbed N_2 volume around $p/p_0 = 0.8$ is characteristic for capillary condensation in the nanometer scaled pores. When the pores are completely filled and the relative pressure is increased further nitrogen can condense outside the sample. Upon desorption (blue line) the sample is subsequently emptied resembling the curve of the adsorption except for a hysteresis. This hysteresis originates in the shape of the mesopores. Upon adsorption the pores fill by adding multilayers from the surface towards the pore center resulting in a liquid front of cylindrical shape [71]. In contrast during desorption the adsorbent is removed starting from the pore wall towards the pore center so that the receding liquid phase is hemispherical. This asymmetry of both processes results in the hysteresis loop. Its shape thereby strongly depends on the pore diameter and surface tension of the liquid.

The evaluation of the desorption isotherm, that is the thermodynamically more stable state [72], yields a pore size distribution. Assuming cylindrical mesopores and two adsorption mechanisms, physical adsorption on the pore walls and capillary condensation in the pore volume, this pore size distribution can be calculated following the BJH method developed by Barrett, Joyner and Halenda [73, 74]. Figure 3.2(b) shows this increase in pore volume as a function of pore radius resulting from the BJH analysis. The pore

²The measurements are performed with the autosorb iQ gas sorption system from Quantachrome Instruments.

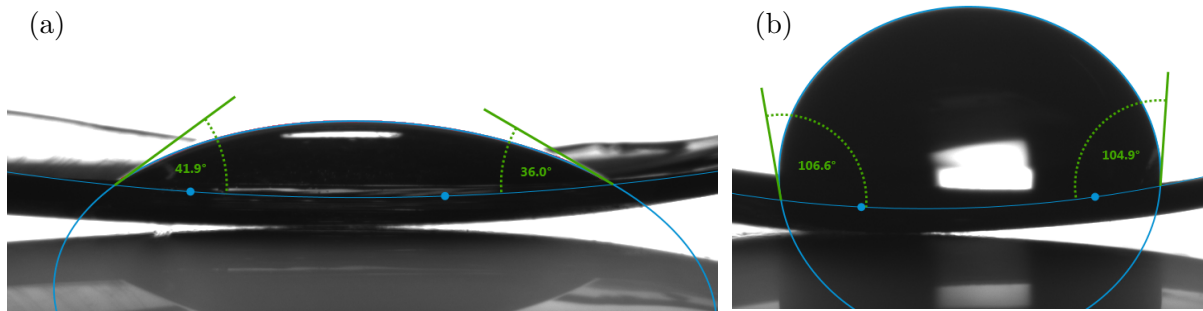


Figure 3.3.: Water contact angle (green) at the surface of (a) native and (b) dimethylchlorosilan-trichlormethan (DMCS-T) modified pSiO₂. Blue line shows fit performed in order to determine the contact angle.

radius is then determined as the point of maximal increase in pore volume. However, a sizable distribution of the pore radius is present. The porosity is calculated by comparing the amount of adsorbed N₂ to the lateral dimension, hence, the volume, of the membrane. The average pore diameters and porosities vary between $d = 15.6 - 17.4$ nm and $P = 44 - 50$ %, see table A.1 in appendix A.

After thermal oxidation the native pSiO₂ surface is hydrophilic due to Si-O-Si and Si-OH surfaces species [71]. This characteristic can be quantified by measuring the contact angle of water with the pSiO₂ surface, see fig. 3.3(a)³. The contact angle is thereby defined as the angle between a line tangential to the surface of the water drop (green line) and the solid that the drop contacts [71]. An angle smaller than 90°, in the case of pSiO₂ it is about 40°, identifies the surface to be hydrophilic. Treatment with a 1:9 dimethylchlorosilan-trichlormethan (DMCS-T) solution for 2 h replaces the hydrophilic hydroxyl groups by hydrophobic methyl groups resulting in Si-O-Si(CH₃)₂-O-Si surface species [71, 75]. This chemical modification enhances the hydrophobicity and thus the surface contact angle of water up to 105°, see fig. 3.3(b).

Meso- and macroporous anodized aluminum oxide

AAO membranes are purchased from SmartMembranes GmbH (SM) and InRedox LLC (IR), as well as provided by the research group of M. Steinhart University of Osnabrück (OS). Experimental details on the manufacturing process can be found in refs. [76–80]. Aluminum is oxidized to porous alumina during an electrochemical anodization process. Due to a field-enhanced oxide dissolution at the oxide/electrolyte interface and oxide growth at the metal/oxide interface pores grow perpendicular to the surface. The self-ordering into an hexagonal lattice of the pores thereby results from repulsive forces between neighboring pores due to mechanical stress [79]. Depending on the pore diameter different electrolytes are used, see table A.1. The smallest pores can be produced with the lowest pH-value, hence, the strongest acid. The optimum porosity for self-ordered AAO

³Measurements are performed with the Krüss Drop Shape Analyzer DSA100.

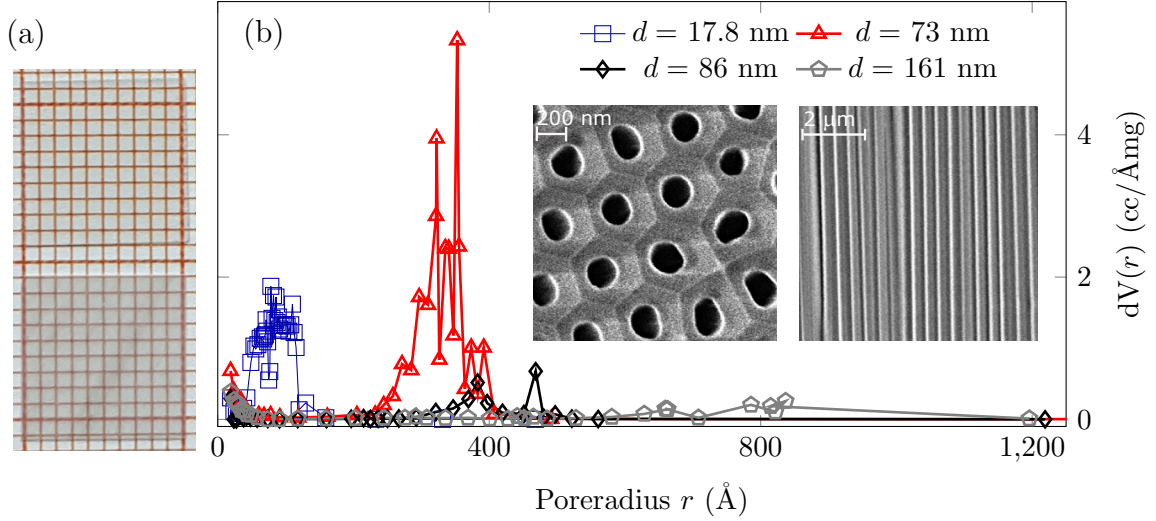


Figure 3.4.: (a) Photograph of two $10 \times 10 \text{ mm}^2$ sized AAO membranes with (top) $d = 16.7$ nm and (bottom) $d = 161$ nm. (b) Four exemplary pore size distributions of AAO showing the variation of the measured pore volume as a function of the pore radius. Inset: Scanning electron micrograph showing top (left) and side view (right) of an AAO membrane with $d = 161$ nm.

independent of the used electrolyte is 10 %, that results in an optimum interpore distance d_{int} for self-ordered AAO. Other porosities result in less ordered AAO pores [80]. Depending on the electrolyte three different interpore distances for three different pore diameters can be achieved: $d_{\text{int}} = 65$ nm for H_2SO_4 , $d_{\text{int}} = 125$ nm for $\text{C}_2\text{H}_2\text{O}_4$, $d_{\text{int}} = 480$ nm for H_3PO_4 . The difference in the interpore distance manifests itself in the difference of the optical transparencies of the membranes. The smaller the interpore distance, the smaller is the pore diameter resulting in a more transparent membrane, see fig. 3.4(a). Membranes with a porosity much higher than 10 % are produced by chemical pore widening. Hence the interpore distance is maintained while the porosity and pore diameter increase. To recheck the pore sizes and porosities indicated by the producer volumetric N_2 sorption isotherms are performed resulting in pore diameters varying from 16.7 nm to 161 nm and porosities from 7 % to 37 %, see table A.1. Figure 3.4(b) shows four exemplary pore size distributions. Corresponding isotherms can be found in appendix A in fig. A.1. For pores larger than 80 nm the condensation pressure is close to the bulk condensation pressure. Thus, the measurement technique is not sensitive in this regime as can be also seen from the large error values of the pore diameters in table A.1. To eliminate this inaccuracy multiple sorption isotherms are performed. In addition, the pore sizes are rechecked in scanning electron micrographs. A top and side view scanning electron micrograph of a membrane with the largest pore diameter is shown in the inset in fig. 3.4(b)⁴.

Similar to pSiO_2 the native hydrophilic AAO surface can be rendered to be more hydrophobic. However, diffraction measurements on self-assembled monolayers (SAMs) made up of silane and highly ordered sapphire (Al_2O_3) revealed an incomplete silane-sapphire sur-

⁴Images taken with Leo Gemini 1530 FEG-REM.

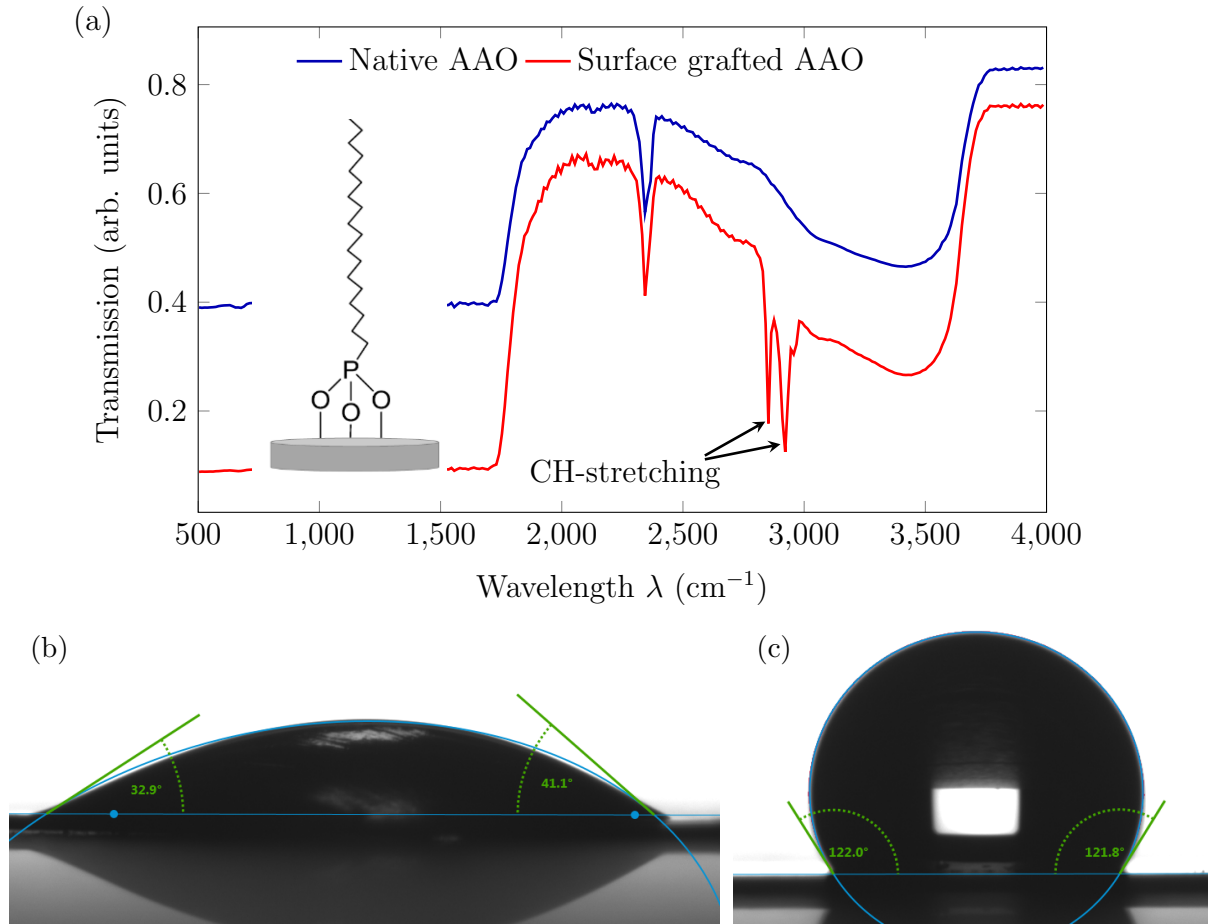


Figure 3.5.: (a) Fourier-transform infrared spectrum of a native (blue line) and surface grafted (red line) AAO membrane with $d = 38$ nm. The inset illustrates P-O₃-(CH₃)₁₈ surface species in surface grafted AAO. (b, c) Water contact angle (green) at the surface of (b) native and (c) ODPA surface grafted AAO. Blue line shows the fit performed in order to determine the contact angle.

face bonding [81]. In contrast to that, investigations of SAMs consisting of phosphonic acids on aluminum showed an increased packing density compared to SAMs made up of silans [82]. Additionally, SAMs of phosphonic acids on alumina showed a homogeneous layer formation. The longer the used molecule, the denser the layer packing [83]. Hence, functionalization of the AAO surface by phosphonic acid is more stable in comparison to silanization. Therefore the AAO surface is altered by chemical treatment with octadecylphosphonic acid (ODPA)⁵ [84]. As a first step the surface is activated in a 30 % aqueous H₂O₂ solution for 2 h at 45 °C and then dried at 120 °C for 15 min. Afterwards AAO is placed in a 4.2 mM solution of ODPA and 5:1 cyclohexan/isopropyl solution for 48 h at room temperature. The surface grafted AAO is then washed and sonicated with the cyclohexan/isopropyl solution to remove any remaining ODPA. During the process hydrophilic O-H surface species are replaced by hydrophobic P-O₃-(CH₃)₁₈ surface species, see inset in fig. 3.5(a), enhancing the water contact angle from approximately 35° to 120°, see fig. 3.5(b,c). The efficiency of the surface treatment is additionally checked with Fourier-transform infrared spectroscopy (FTIR)⁶. Two exemplary AAO spectra are shown in fig. 3.5(a). The transmission intensity of the infrared beam as a function of its wavelength is plotted for a native (blue line) and surface grafted (red line) AAO membrane. The adsorption peak at $\lambda = 2343\text{ cm}^{-1}$ results from carbon oxide in the surrounding air, i.e. C-O stretching. Clearly two absorption lines characteristic for the asymmetric ($\lambda = 2930\text{ cm}^{-1}$) and symmetric ($\lambda = 2850\text{ cm}^{-1}$) C-H stretching resulting from the P-O₃-(CH₃)₁₈ surface species are present in the spectrum of the surface grafted AAO membrane, while absent in that of native AAO indicating a successful surface treatment. Additionally, sorption isotherms were performed on the modified membranes. Comparing the resulting pore diameters with that of unmodified AAO yields an ODPA molecule length of approximately 2.2 nm in agreement with theoretical calculations.

3.2. Experimental techniques

3.2.1. Sample preparation

To enable prospective conduction measurements the filling procedure of the membranes is performed in a protective argon atmosphere⁷. Prior to filling, the membranes are outgassed at 200 °C for 20 h to remove water residues. To ensure complete filling the filling process is performed for 48 h at a temperature slightly above the bulk isotropic-liquid crystalline transition temperature [85]. Thereby, resulting from capillary forces, the membrane's pores are filled with the liquid crystal via spontaneous imbibition. Afterwards

⁵Octadecylphosphonic acid (ODPA) was purchased from Sigma-Aldrich.

⁶Measurements are performed with a Vertex 70 FTIR from Bruker Corporation.

⁷Sample preparation is performed in an UNilabPLUS Glove Box Workstation from M. Braun Inertgas-Systeme GmbH.

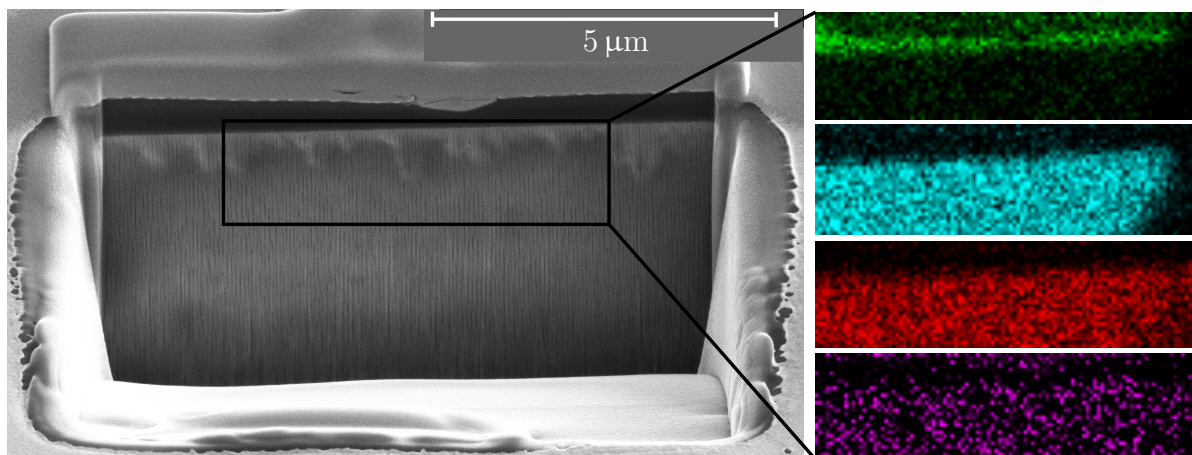


Figure 3.6.: Left: Crosscut scanning electron micrograph of AAO ($d = 16.7$ nm) membrane filled with HAT6. Right: Energy dispersive X-ray spectroscopy map performed in region marked left. From top to bottom: carbon (green), oxygen (blue), aluminum (red), sulfur (purple).

the membranes surface is carefully scratched to remove any remaining material on top. Nevertheless, a small bulk film can remain on top of the membranes, due to e.g. high surface roughness. Prior and after filling, the membranes are weight to determine the amount of the liquid crystal inside the pores. After being filled the pore diameter of surface modified membranes is assumed to be that of the native membranes since the ODPA/DMCS-T molecules are pressed flat to the surface.

Figure 3.6 shows an energy dispersive X-ray spectroscopy (EDX) map of a crosscut⁸ of a HAT6 filled AAO membrane. An electron beam excites atoms in the sample, which then emit element characteristic X-rays that can be detected. Besides the expected elements (carbon, aluminum, oxygen due to AAO and HAT6), fig. 3.6 shows that sulfur atoms are situated in the sample. This proves, that despite thoroughly rinsing, up to 5 wt% anions of the used acids, in this case sulfuric acid see table A.1, are integrated into the amorphous AAO structure.

3.2.2. Optical polarimetry setup⁹

In order to determine the temperature dependent strength of the birefringence of a sample a measurement setup utilizing modulation polarimetry is used as shown in fig. 3.7 and fig. 3.8(a). During the course of this thesis the temperature sample cell was replaced from a self-built copper cell, see fig. A.2 in appendix A, to a nitrogen cooled TSH600 heating/-cooling chamber¹⁰ allowing temperatures inbetween -196 °C to 600 °C. The temperature scans are performed with cooling/heating rates of 0.03 K/min for bulk samples and 0.15 K for confined DLCs. An existing LabView program enabling the communication between used hardware and computer is extended and adjusted, see appendix A.2.

⁸The crosscut is produced using a focused ion beam (FEI Helios NanoLab G3).

⁹Parts of this section will be published in reference [86].

¹⁰Chamber was purchased from RESULTEC analytic equipment.

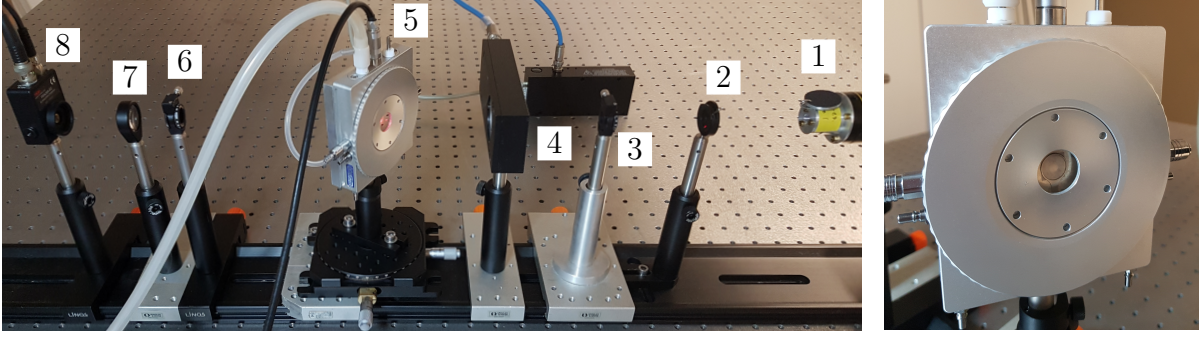


Figure 3.7.: (Left) Photograph of the optical setup used to measure the linear optical birefringence: (1) He-Ne laser, (2) iris diaphragm to stop reflected laser beams, (3) polarizer, (4) photoelastic modulator and controller, (5) sample cell, (6) analyzer, (7) lens and (8) photodiode. (Right) The sample is fixed inside the sample cell by a vertical ring-shaped holder.

The polarimetry setup similar to that described in refs. [45, 87] consists of a He-Ne-laser ($\lambda = 632.8 \text{ nm}$) emitting linearly polarized light. After being linearly polarized 45° to the direction of propagation by a polarizer the light passes through an optical photoelastic modulator (PEM). The PEM exhibits a time dependent birefringence due to the photoelastic effect [88]

$$\Delta n_{\text{PEM}} = \Delta n_0 \sin(\Omega t). \quad (3.1)$$

This results in a temporal modulated retardation

$$\delta_0 = \Delta n_0 d_M \sin(\Omega t) \quad (3.2)$$

with thickness of optical slab d_M , retardation amplitude $\delta_0 = \Delta n_0 d_M = 0.383\lambda$ and resonant frequency of the optical element $\Omega = 50 \text{ kHz}$. The transparent and optical isotropic element is resonantly exposed to mechanical stress by a quartz piezoelectric transducer. Is the optical element relaxed the 45° linearly polarized light passes through the PEM unchanged. If it is compressed or stretched it exhibits birefringence, so that either the horizontal or vertical component of the electromagnetic wave travels faster, leading to a phase difference called retardation. The retardation depends on the strength of the birefringence, and hence on the strength of the applied stress, which oscillates at $\Omega = 50 \text{ kHz}$. Due to the resulting time dependent phase difference the electromagnetic wave is either linearly, circular or elliptically polarized after passing the PEM. Also, the rotation direction of the polarization vector changes from left to right handed or *vice versa* during one period. In addition to this time dependent birefringence, the laser light exhibits the static, temperature dependent birefringence Δn_x of the sample. Afterwards, the light passes an analyzer, that is set crossed to the polarizer, and then focused on a photo diode. The photo diode is connected to two Lock-Ins and detects the intensity of the first and second harmonic wave of the laser light. Therefore, considering a static birefringent sample inbetween crossed polarizer/analyzer, the emerging wave vector projected on the

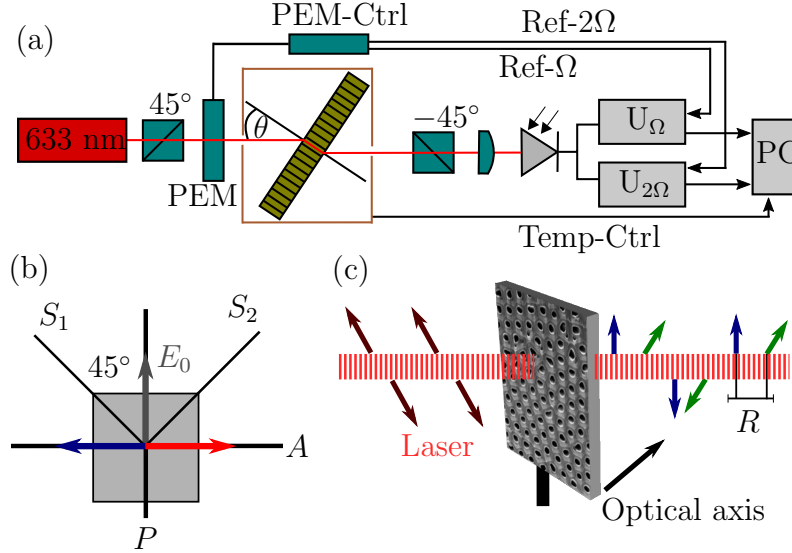


Figure 3.8.: (a) Schematic of optical retardation setup with (from left to right): He-Ne laser, polarizer (+45°), photoelastic modulator (PEM) with modulation frequency Ω , temperature cell, analyzer (−45°), lense, photodiode and Lock-In amplifiers. (b) Simplified projection of polarization axes of polarizer and analyzer with respect to the anisotropic sample axes. (c) Alignment of sample at angle $\theta \approx 40^\circ$ with respect to the laser beam. Arrows show polarization of laser before and after passing the sample resulting in an optical retardation R .

analyzer axis, see fig. 3.8(b), is given by

$$\begin{aligned} E &= \frac{\sqrt{2}}{2} E_0 \cos(45^\circ) \sin(\omega t) - \frac{\sqrt{2}}{2} E_0 \cos(45^\circ) \sin(\omega t - \delta) \\ &= \frac{1}{2} E_0 [\sin(\omega t) - \sin(\omega t - \delta)] \end{aligned} \quad (3.3)$$

with $\delta = \Delta n d$ and thickness d of birefringent plate. Thereby the angle between incident laser light and anisotropic sample axis S_1 and S_2 is approximately 40° as illustrated in fig. 3.8(a) and (c). By taking the time average the intensity detected at the photo diode can be expressed by

$$I \sim \overline{E^2} \sim \overline{[\sin(\omega t) - \sin(\omega t - \delta)]^2} = 1 - \cos(\delta). \quad (3.4)$$

Considering the time dependent retardation δ_0 induced by the PEM, see eq. (3.1), and temperature dependent birefringence of the sample δ_x , eq. (3.4) can be expanded in Fourier series including Bessel functions J_n

$$I = 1 - \cos[\delta_x - \delta_0 \sin(\Omega t)] \quad (3.5)$$

$$= 1 - \cos(\delta_x) \cos[\delta_0 \sin(\Omega t)] + \sin(\delta_x) \sin[\delta_0 \sin(\Omega t)] \quad (3.6)$$

$$= 1 - \cos(\delta_x) \left(J_0(\delta_0) + 2 \sum_{m=1}^{\infty} J_{2m}(\delta_0) \cos(2m\Omega t) \right)$$

$$+ \sin(\delta_x) \left(2 \sum_{m=0}^{\infty} J_{2m+1}(\delta_0) \sin[(2m+1)\Omega t] \right). \quad (3.7)$$

The modulation amplitude is chosen so that $J_0(\delta_0) = 0$. The total signal can then be resolved as ac components at Ω and 2Ω . The Lock-In technique eliminates the time dependency, so that the dc components of the intensity of the first and second harmonics are

$$I_{\Omega} \sim J_1(\delta_0) 2 \sin(\delta_x) \quad I_{2\Omega} \sim J_2(\delta_0) 2 \cos(\delta_x) \quad (3.8)$$

$$\Rightarrow \frac{I_{\Omega}}{I_{2\Omega}} = \frac{J_1(\delta_0)}{J_2(\delta_0)} \tan(\delta_x) \quad (3.9)$$

$$\Leftrightarrow \delta_x = \arctan \left(\frac{U_{\Omega} \cdot J_2(\delta_0)}{U_{2\Omega} \cdot J_1(\delta_0)} \right) = R \quad (3.10)$$

The contributions of the Bessel function are constants of the experimental setup; $J_2(\delta_0)/J_1(\delta_0) = 0.83$.

Equation 3.10 is only defined for a retardation R inbetween 0° and 90° . Data of samples that exhibit retardation effects of more than 90° need to be recalculated according to that. When the optical retardation R hits 0° or 90° the phase of either the 1st or 2nd harmonic, as adjusted by the Lock-Ins, experiences a 180° jump. By performing reference measurements these jumps can be calibrated. A sample of known birefringence, e. g. positive geometrical birefringence (AAO $d \leq 80$ nm), is rotated starting from perpendicular incident of the laser beam with respect to the sample surface. As the angle between laser beam and long pore axis increases the geometric birefringence starts to set in. Depending on the phase values the retardation either increases or decreases upon starting to rotate, see table A.2 in appendix A. This calibration can then be applied to the measured temperature curve of the optical retardation. Depending on this the sample either shows positive or negative retardation.

For a tilted sample geometry as shown in fig. 3.8 the measured optical retardation R can be converted to the optical birefringence Δn using Berek's equation [59, 89], see derivation in appendix A.3,

$$R = \frac{2\pi t(\bar{n} - \Delta n/3)}{\lambda} \cdot \left\{ [1 - (\bar{n} + 2\Delta n/3)^{-2} \sin^2(\theta)]^{1/2} - [1 - (\bar{n} - \Delta n/3)^{-2} \sin^2(\theta)]^{1/2} \right\} \quad (3.11)$$

with sample thickness t , average refractive index $\bar{n} = (2n_o + n_e)/3$ and angle $\theta \approx 40^\circ$ between laser beam and long pore axis. The optical birefringence is approximately proportional to the order parameter defined in eq. (2.5) [45]. However, eq. 3.11 only depends on parameters that are experimental constants. So it is sufficient to analyze the optical retardation R in order to make statements about the molecular orientation. Neverthe-

less, considering an effective medium model the optical birefringence can be recalculated from the measured optical retardation using eq. 3.11. Therefore, the porous membranes are considered having a volume fraction $1 - P$, with porosity P determined by sorptions isotherms discussed in section 3.1.2. The nanopores are represented as cylindrical inclusions with volume fraction P . Assuming completely filled pores the average refractive index \bar{n} can be estimated by solving the generalized Bruggemann equation [45, 90]

$$P \frac{\varepsilon_{\text{LC}} - \varepsilon_{\parallel,\perp}^{\text{ef}}}{\varepsilon_{\parallel,\perp}^{\text{ef}} + L_{\parallel,\perp}(\varepsilon_{\text{LC}} - \varepsilon_{\text{j}}^{\text{ef}})} = (P - 1) \frac{3(\varepsilon_{\text{AAO}} - \varepsilon_{\parallel,\perp}^{\text{ef}})}{2\varepsilon_{\parallel,\perp}^{\text{ef}} + \varepsilon_{\text{AAO}}} \quad (3.12)$$

with pore permittivity $\varepsilon_{\parallel,\perp}$ parallel or perpendicular to the long pore axis and depolarization factor $L_{\parallel} = 0$ and $L_{\perp} = 0.5$. The average refractive index is then given by

$$\bar{n} = \sqrt{(1 - P)\varepsilon_{\text{AAO}} + P\varepsilon_{\text{LC}}} = \frac{2\sqrt{\varepsilon_{\perp}} + \sqrt{\varepsilon_{\parallel}}}{3}. \quad (3.13)$$

In principle, the effective medium model discussed above can be used to analyze the effective optical properties of a metamaterial made up of at least two components with different optical properties. Such a metamaterial is made up of often periodic artificially “metaatoms” with a typical size $s = 10 \text{ nm} - 100 \text{ nm}$ [4]. Compared to the wavelength of visible light ($\lambda \approx 380 \text{ nm} - 740 \text{ nm}$) these metaatoms are considerably smaller, hence, $s \ll \lambda$ ¹¹. Therefore, the closely packed metaatoms still form a material that is continuous at the scale of λ and can be attributed an effective refractive index \bar{n} , see eq. (3.13).

3.2.3. X-ray diffraction

X-ray diffraction is a useful method to measure the translational order of condensed matter, in this case the translational ordering of DLCs in the liquid crystalline phase. The liquid crystalline structure is in the order of a few nanometer, see sec. 3.1.1. Hence, the used X-ray wavelength λ needs to be close to the lattice constant.

Considering only elastic scattering, X-rays that are refracted at a series of lattice layers experience constructive interference if the Bragg equation

$$\Delta s = 2d \sin(\theta) = n\lambda \quad n = 1, 2, 3, \dots \quad (3.14)$$

holds, with lattice layer distance d , refraction angle θ and wavelength λ . The path difference Δs needs to be multiples of the used wavelength in order to achieve constructive interference. Equivalent to this condition is the Laue equation. An incoming planar wave

¹¹In contrast to that, photonic crystals modulate the refractive index at the scale $s \approx \lambda$. They are designed to have photonic bandgaps often realized by adding structural defects like points to trap light or dislocations to guide light [4]. An effective medium theory can not be applied to photonic crystals.

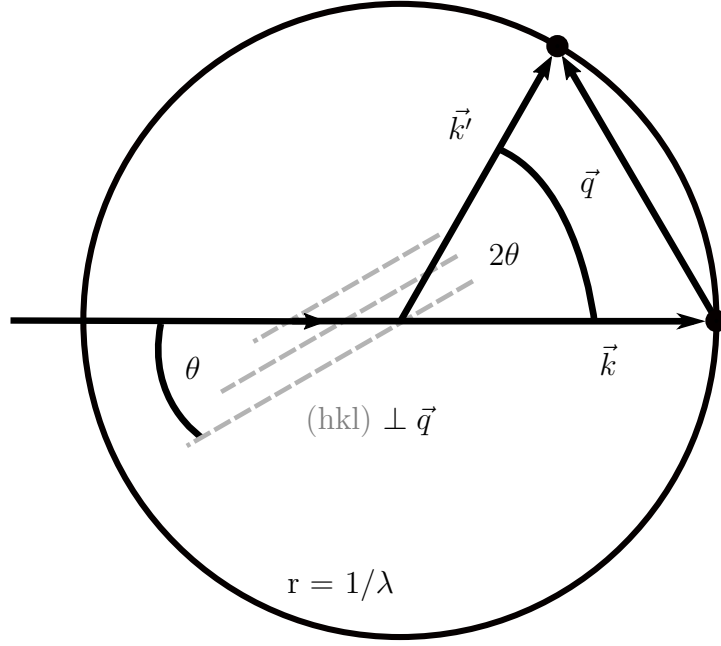


Figure 3.9.: Elastic scattering illustrated by the Ewald sphere construction. \vec{k} and \vec{k}' are the incoming and outgoing beam, $\vec{q} = \vec{k}' - \vec{k}$ is a reciprocal lattice vector.

$\Psi(\vec{r}) = \Psi_0 \exp(i\vec{k}\vec{r})$ with wave vector \vec{k} and space coordinates \vec{r} is refracted at atoms located at series of lattice points generating spherical waves that have a specific path difference. Bragg peaks occur only if the difference of the wave vectors of the refracted beam \vec{k}' and incoming beam \vec{k} equals that the lattice vector \vec{q}

$$\vec{k}' - \vec{k} = \Delta K = \vec{q}. \quad (3.15)$$

Considering only elastic scattering the wave vector's modulus of the incoming beam equals that of the refracted beam

$$|\vec{k}| = |\vec{k}'|. \quad (3.16)$$

This scattering condition can be illustrated with the Ewald sphere as shown as a 2D projection in fig. 3.9. The vector $-\vec{k}$ starts at an arbitrary point of the reciprocal lattice. The ending point of the vector is the center of the Ewald sphere with radius $r = 2\pi/\lambda$. A Bragg peak occurs when the Ewald sphere intersects with a reciprocal lattice point resulting in a refracted beam in the direction $\vec{k}' = \vec{k} + \vec{q}$. By changing the value of \vec{k} or its direction this refraction condition can always be achieved.

The recorded diffraction pattern yields information about the peak position, its intensity and shape characterized by the full width at half maximum $\text{FWHM} = \Delta Q$. Using the Scherrer equation the coherence length ξ giving information about the average crystal or domain size can be extracted from ΔQ [91]

$$\xi = \frac{2\pi}{\Delta Q} = \frac{K \cdot \lambda}{\Delta\theta \cdot \cos(\theta)} \quad (3.17)$$

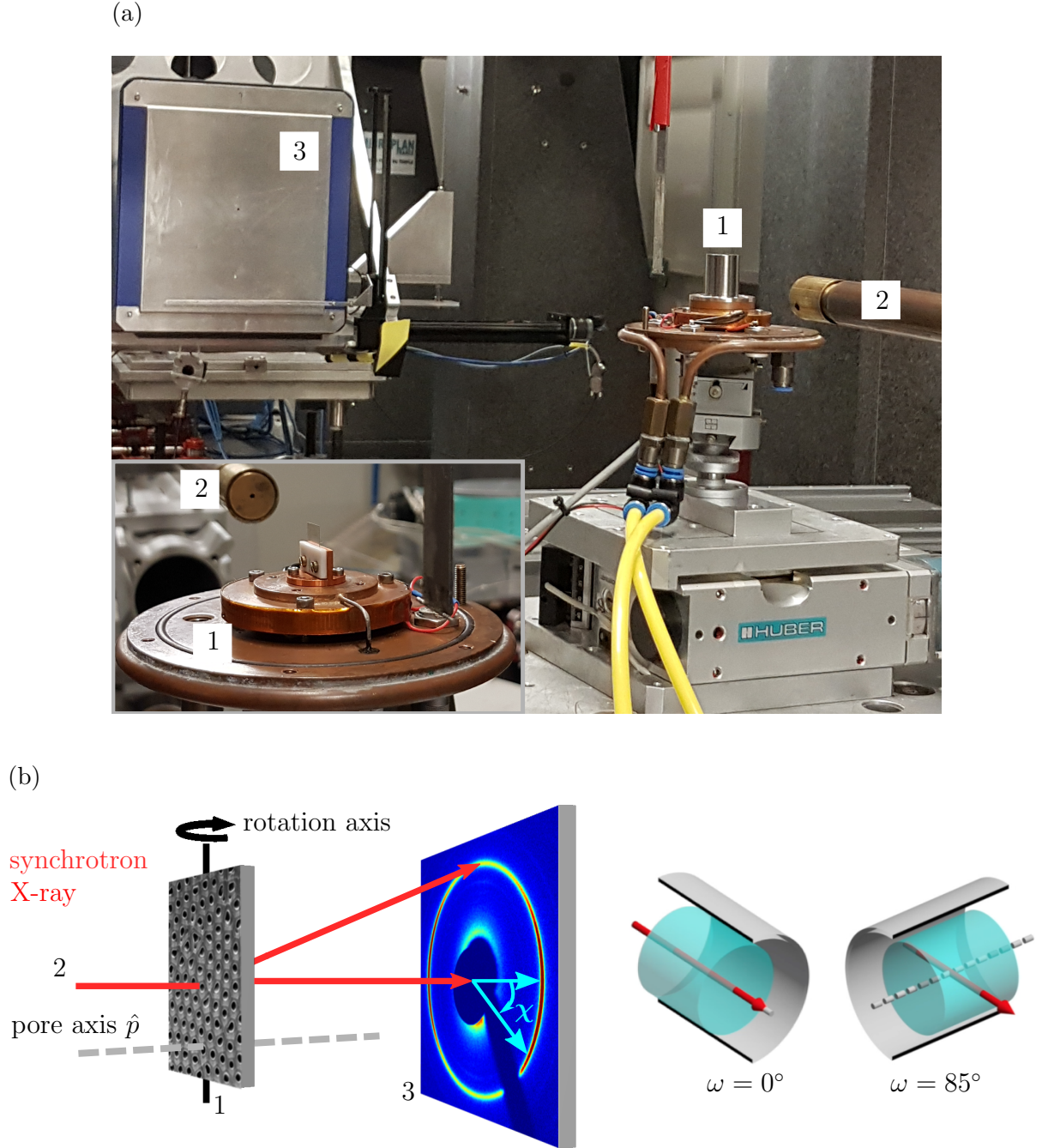


Figure 3.10.: (a) Photograph (taken at ID31 beamline at ESRF) and (b) schematic of the X-ray transmission experiment. The incoming X-ray beam exiting the beam tube (2) traverses the sample mounted on copper temperature cell (1) at an angle ω with respect to the membrane surface normal. For $\omega = 0^\circ(85^\circ)$ the X-ray beam is parallel (almost perpendicular) to the long pore axis \hat{p} (gray dashed line). During measurements the sample is covered by a beryllium dome to ensure a stable temperature environment. The diffraction pattern is detected by an area detector (3). The cyan arrows in (b) indicate the azimuth angle χ along the diffraction ring.

with used wavelength λ , Bragg angle θ and FWHM expressed in degree $\Delta\theta$. $K = 0.9$ is an empirical proportionality factor. ΔQ or $\Delta\theta$ can be determined by performing a Gaussian fit to the Bragg peak, which is usually a superposition of the scattering from the sample and instrumental resolution. Hence, the peak width needs to be corrected accordingly.

In this thesis, transmission synchrotron X-ray experiments were performed at PETRA III at Deutsches Elektronen-Synchrotron (DESY) [92], the European Synchrotron Radiation Facility (ESRF) and the National Synchrotron Light Source (NSLS II), see details in table A.3 in appendix A and illustrations of setup in fig. 3.10. Compared to lab sources X-rays generated by synchrotrons have several advantages. Their high brilliance, that is the ratio of number of photons produced per second with respect to their angular divergence, the beam cross-sectional area and the photons falling within a bandwidth (BW) of 0.1% of the used wavelength, reduces the exposure time for one diffractogram from a few hours to several seconds. In addition, energies of a few 10 keV are necessary in order for the X-ray beam to pass the membranes without being adsorbed entirely.

A schematic and photograph of an exemplary setup used at the ID31 beamline at ESRF is shown in fig. 3.10. The setups at NSLS II and DESY were similar, see table A.3. To allow temperature dependent measurements the sample is placed in a copper temperature cell. It can be heated by a heating foil, while a PT-100 sensor connected to a Lakeshore temperature controller reads the sample temperature. Temperature scans are performed with a cooling/heating rate of 1 K/min. To enable a stable sample environment the copper cell is constantly cooled with water (18°C). It is placed on a Huber stage, that allows translation along the beam direction and perpendicular to it. Additionally, a rotation of the cell is possible. The inset in fig. 3.10(a) shows the configuration for $\omega = 85^\circ$. The incoming X-ray beam exiting the beam tube is almost perpendicular to the surface normal of the membrane and thus to the pores. Hence, the incident wavevector \vec{q}_i is almost perpendicular to the direction of the long axis of the nanochannels \hat{p} , hence, $q_i \perp \hat{p}$. Thus, the translational molecular order within cross-sections aligned along \hat{p} and the vertical direction is probed. Consequently, $\omega = 0^\circ$ is the configuration with beam direction parallel to the surface normal and thus parallel to the pores, hence, $q_i \parallel \hat{p}$. Exiting the pore the diffracted beam is then detected by an area detector. The data analysis is performed within MATLAB. A typical diffraction pattern is shown in the schematic in fig. 3.10(b). The diffraction patterns are described with respect to the meridian and equator: the meridian is vertical and the equator horizontal. Additionally, the diffraction patterns are characterized by their azimuth angle χ indicated by cyan arrows. Thereby $\chi = 0^\circ$ (360°) equals the direction along the equator. Going in the mathematically positive direction the azimuth angle increases, so that $\chi = 90^\circ$ and 270° lie along the meridian line and $\chi = 180^\circ$ again along the equator.

4. Quantized self-assembly of discotic rings in nanoconfinement¹

Hydrophilic and hydrophobic pSiO₂ is prepared by an electrochemical etching and subsequent oxidation process and subsequently filled with the DLC HAT6 as described in sections 3.1.2 and 3.2.1. To correlate orientational and translational ordering the samples are investigated by temperature dependent optical birefringence and X-ray diffraction measurements as described in section 3.2.2 and section 3.2.3. To prove reproducibility multiple samples were prepared showing the same experimental results that will be discussed below.

As a reference measurement the temperature dependence of the optical retardation $R(T)$ of bulk HAT6 in between two glass plates is shown in fig. 4.1(a). At high temperature in the isotropic phase no retardation, hence, no molecular orientation is present. Slowly cooling down, the molecules start to orient at $T_{\text{bulk}}^{\text{ci}} = 371 \text{ K}$ ² resulting in a drastic drop in $R(T)$ to negative values. This means that, in agreement with the negative dielectric anisotropy of DLCs, see section 2.3, the molecules orient with their director dominantly perpendicular to the glass surface [21]. So for this configuration a negative birefringent material is realized with $\Delta R \sim \Delta n < 0$. Hence, it indicates a formation of a face-on orientation at the glass surface and thus column formation along the surface normal as shown in the inset in fig. 4.1(a). Upon heating, $R(T)$ vanishes in a more gradual way and equals zero at $T_{\text{bulk}}^{\text{ci}}$. Additionally, a small temperature hysteresis is present. This indicates that, even in the bulk cell, the thermotropic pathways differ upon cooling and heating [21]. Upon cooling presumably small clusters of the Col_h phase occur over the whole sample volume. Whereas upon heating a phase transition front separates larger isotropic and columnar domains. Additionally, surface-molecular interactions can delay the occurrence of the columnar phase upon cooling.

The temperature dependencies $R(T)$ of HAT6 imbibed in hydrophilic and hydrophobic pSiO₂ are shown in figs. 4.2(a) and 4.1(b) respectively. The results are reproducible in subsequent multiple cooling/heating cycles. Compared to the bulk behavior the first-order phase transition is rendered by the geometrical constraints to a more gradual one show-

¹Parts of the results discussed in this chapter are published in reference [49] and reused with permission from the American Physical Society Copyright 2018.

²Upon cooling surface-molecule interactions can delay the isotropic-columnar phase transition. To eliminate this influence $T_{\text{bulk}}^{\text{ci}}$ is determined by $R(T_{\text{bulk}}^{\text{ci}}) = 0$ upon heating.

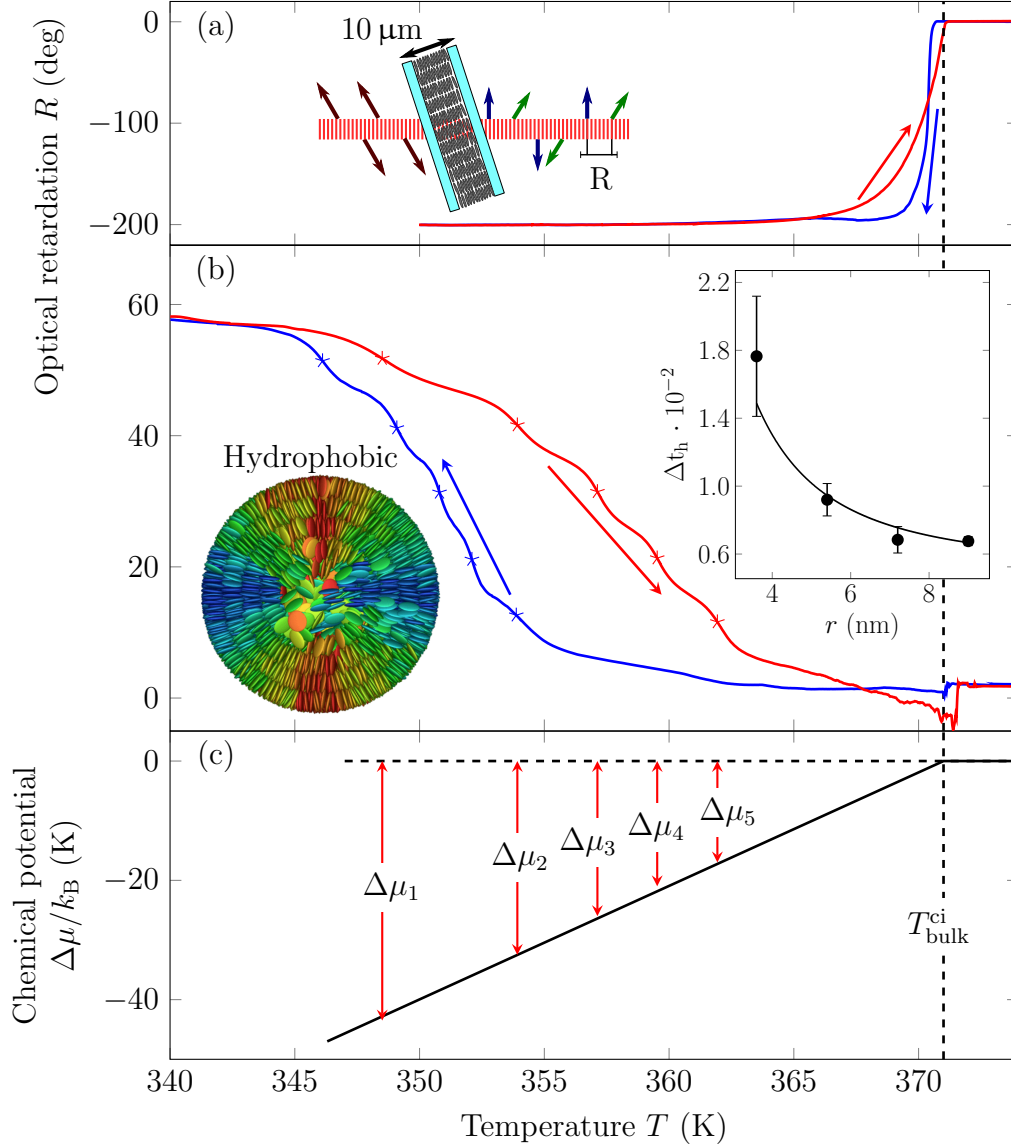


Figure 4.1.: Temperature evolution of the retardation $R(T)$ of HAT6 in the (a) bulk state and (b) confined in hydrophobic pSiO₂ with pore diameter $d = (17.4 \pm 0.3)$ nm and porosity $P = (50 \pm 1.9)\%$. Shown are a cooling (blue) and subsequent heating run (red). Insets: (a) Schematic illustration of the bulk cell with a 10 μm gap where the molecules orient face-on, hence, with their director perpendicular to the glass surface. (b) Normalized supercooling isotropic-columnar transition temperature of each ring with curvature radius r along with a r^{-2} fit. Top view of pSiO₂ pore containing concentric columnar rings (extracted from Monte Carlo simulations). The color code of the LC molecules indicates the molecular alignment with respect to the horizontal axis: blue means 0° and red 90°. (c) Chemical potential $\Delta\mu$ -temperature T phase diagram of HAT6 showing the excess energy $\Delta\mu_n$ of a molecule in ring n . It is indicated by arrows at the supercooling temperatures T_n ($n = 1 \dots 5$) in panel (b). Adapted and reprinted with permission from [49]. Copyright American Physical Society 2018.

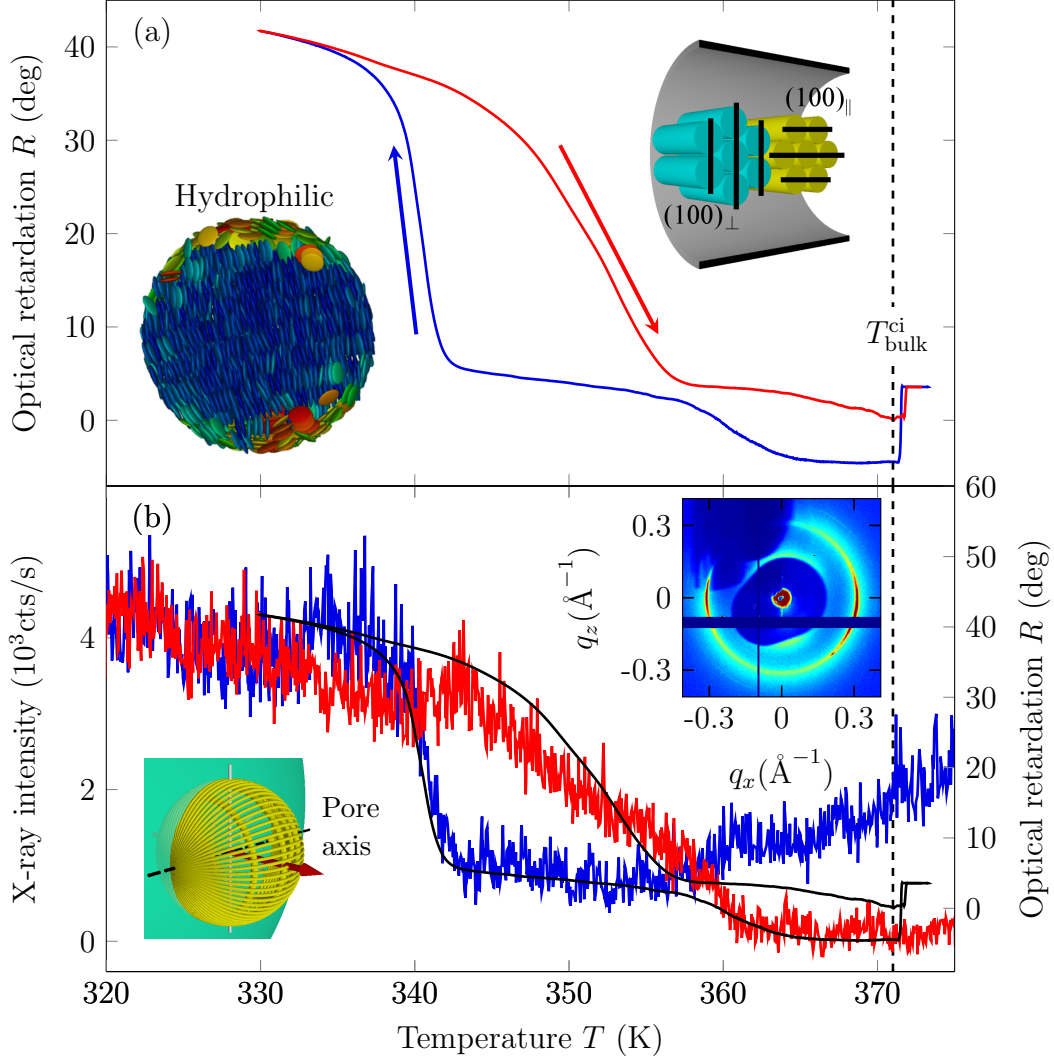


Figure 4.2.: (a) Temperature dependent optical retardation $R(T)$ of HAT6 in hydrophilic pSiO₂ with $d = (15.6 \pm 1.9)$ nm and $P = (44.0 \pm 0.1)$ %. The transition temperatures are determined to $T_{\text{cool}}^{\text{ci}} = (340.7 \pm 0.07)$ K and $T_{\text{heat}}^{\text{ci}} = (352.7 \pm 0.3)$ K. Insets: (left) Top view of the logpile molecular orientation inside a pSiO₂ pore extracted from Monte Carlo simulations. The color code of the molecules represents the relative orientation of the molecules with respect to the horizontal axis, where blue means 0° and red 90° alignment. (Right) Schematic of molecular orientation inside the pores indicating the $(100)_{\parallel}$ and $(100)_{\perp}$ direction. (b) Temperature dependent evolution of the (10) Bragg ring for a cooling/heating cycle. $R(T)$ from (a) serves as a guide to the eye. Insets: Enlarged reciprocal space and diffraction pattern focusing on the (10) Bragg ring at $T = 320$ K and $\omega = 85^\circ$.

ing a temperature hysteresis. Additionally, $R(T)$ increases with decreasing temperature towards positive values in both confined cases. So for both cases a positive birefringent material is realized with $\Delta R \sim \Delta n > 0$. Again, resulting from the negative dielectric anisotropy, this behavior indicates an alignment of the molecular director \hat{n} perpendicular to the pore axis [21].

These considerations are in agreement with the radial, logpile or circular concentric configuration, see detailed description in section 2.2.1. Which molecular orientation occurs strongly depends on the surface anchoring conditions. Hydrophilic pSiO₂ results in face-on anchoring and thus a radial or logpile configuration, while a hydrophobic surface leads to an edge-on and thus circular concentric configuration. To fulfill edge-on anchoring in hydrophobic pSiO₂ the columns could also align axially without the necessity of bent columns. However, this configuration results in substantial excess elastic energies originating from the distortions of the 2D hexagonal column lattice at the curved pore surfaces, see eq. (2.28) [24]. As a consequence, the circular concentric configuration is favored.

For HAT6 in hydrophilic pSiO₂ a radial or logpile configuration in agreement with face-on surface anchoring is possible. The corresponding transition temperatures are determined to $T_{\text{cool}}^{\text{ci}} = (340.7 \pm 0.07) \text{ K}$ and $T_{\text{heat}}^{\text{ci}} = (352.7 \pm 0.3) \text{ K}$ ³. The drastic drop/increase in $R(T)$ around 371 K results from the isotropic-columnar phase transition of a bulk film on top of the membrane. Upon subsequent cooling/heating $R(T)$ continuously increases/decreases accompanied by a pronounced temperature hysteresis of 12 K. The hysteresis results from distortions inside the molecular configuration for the logpile as well as for the radial orientation. For the radial configuration the splay distortions are highest in the pore center resulting in an isotropic core [20, 21]. Upon cooling the phase transition starts at the pore wall where surface molecular interactions delay the appearance of the Col_h phase. Upon heating the phase transition starts in the pore center where the isotropic core acts as a nucleation center. One might suggest that distortions for the logpile configuration are largest at the pore wall, so that the isotropic phase is supercooled at that position compared to the center. However, simulations show, that the column formation upon cooling, indeed, starts at the pore wall propagating towards the pore center [50]. This may result from surface-molecule interactions that induce column formation at the pore wall. Then, upon heating, the isotropic phase starts to nucleate in the pore center. To fulfill the surface anchoring conditions in this configuration an isotropic layer at the pore wall is present, see inset in fig. 4.2(a). Which configuration is realized in hydrophilic pSiO₂ can only be determined by extracting the coherence length along the pore diameter from the X-ray diffraction experiment as discussed later.

In contrast to hydrophilic pSiO₂, $R(T)$ does not evolve in a monotonous manner for HAT6

³Characteristic transition temperatures as determined by e.g. differential scanning calorimetry (DSC) correspond to the fastest temperature variation of the order parameter and thus the optical retardation R [20]. Hence, the maximum of the derivative dR^2/dT gives the transition temperatures $T_{\text{cool/heat}}^{\text{ci}}$.

embedded in hydrophobic pSiO₂, see fig. 4.1(b). In agreement with edge-on anchoring the column formation, and thus the direction of \hat{n} , follows the curvature of the pore surface resulting in a circular concentric configuration. Upon cooling/heating a sequence of small plateaus, separated by five pronounced changes in $R(T)$ are present. This results in a staircase-like transition, that is reproducible in subsequent cooling-heating cycles. Compared to the pore diameter roughly ten HAT6 molecules, see dimensions in section 3.1.1, fit into the pore. Coming from the high-temperature isotropic phase the molecules closest to the pore wall start to orient with their director parallel to the pore wall, but still perpendicular to the pore axis. Resulting from the cylindrical confinement they form a bent columnar concentric ring, see inset in fig. 4.1(b). Similar findings were reported for DLCs confined in larger nanopores [24, 25, 93]. Upon decreasing temperature this order propagates to the pore center. Five concentric columnar rings with increasing ring curvature are generated. Thereby each layer contributes to the increase of $R(T)$ at distinct temperatures as marked in fig. 4.1(b). Again a pronounced cooling-heating hysteresis is present. Random nucleation processes at the pore wall delay column formation upon cooling leading to a supercooling of the isotropic phase. Upon heating, resulting from the large curvature and geometric frustration at the pore center, the disordered high temperature phase is nucleated at that position [20]. It expands layer-by-layer towards the wall resulting in a quantized decrease in $R(T)$. Resulting from the laser beam size $R(T)$ corresponds to an averaging of the molecular orientation over multiple nanopores. Typically a not negligible pore size distribution is present leading to variations in the layer transition temperatures. Hence, $R(T)$ does not appear with sharp but rather smeared transition points.

The insets in figs. 4.2(b) and 4.3(e) show X-ray diffractograms of HAT6 in the liquid crystalline phase in hydrophilic and hydrophobic pSiO₂ respectively. The diffractograms will be described with respect to the vertical axis called meridian, and horizontal axis called equator. The incident angle of incoming X-ray beam is chosen, so that the diffraction is sensitive to translational ordering in cross-sections aligned parallel to the long pore axes ($\omega = 75^\circ - 85^\circ$), see diffraction geometry in fig. 3.10. Higher incident angles are not possible because of the absorption of X-rays in the pSiO₂ membrane. Resulting from the lateral dimensions of the HAT6 molecule, see section 3.1.1, Bragg peaks can be observed at a wave vector transfer $q_{(10)} = (0.34 \pm 0.01) \text{ \AA}^{-1}$, typical of the (10) Bragg reflection of hexagonal intercolumnar order. In addition, halos at $q_{dd} = (1.77 \pm 0.01) \text{ \AA}^{-1}$ characteristic of the intracolumnar disk-disk stacking can be observed, see fig. 4.3(d). The hexagonal order can have {100} planes parallel, hence, only (100)_{||} domains, or perpendicular, hence, only (100)_⊥ domains, to the long pore axis as illustrated in the inset of fig. 4.3(a). Complete randomization around the pore diameter leads to (100) domains, hence, {100} planes along every direction with respect to the pore axis.

The X-ray diffractograms in figs. 4.2(b) and 4.3(e) look very similar. Both show a (10)

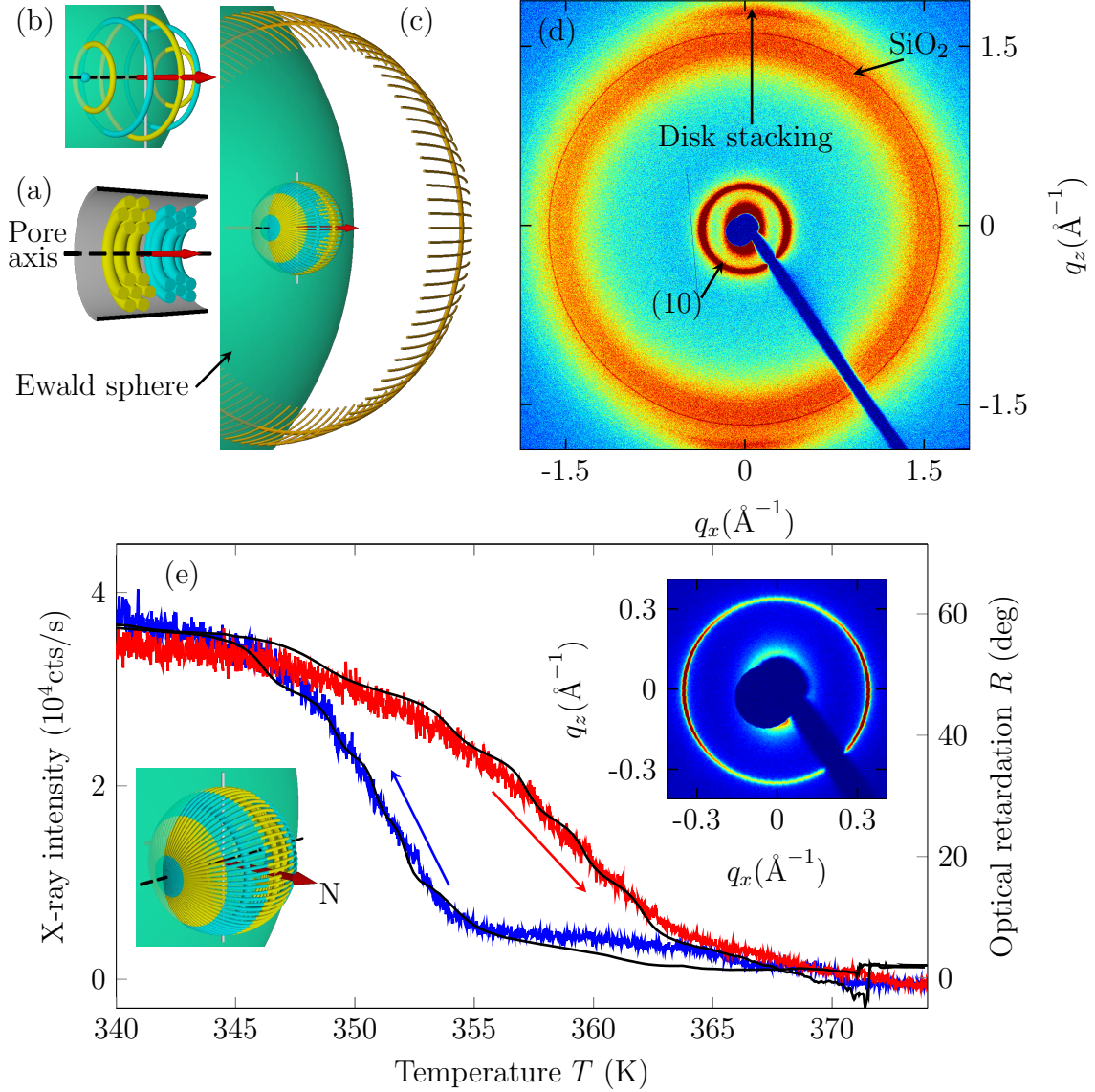


Figure 4.3.: (a) Circular columnar domains with $(100)_{\parallel}$ (yellow) and $(100)_{\perp}$ (green) wall orientation in a cylindrical pore and reciprocal space maps ($\omega = 90^\circ$) assuming (b) perfect aligned and (c) a randomization of the domain orientations by maximal 15° with regard to the mean pore axis direction. (d) X-ray diffraction pattern of HAT6 ($T = 340$ K, $\omega = 75^\circ$) confined in hydrophobic pSiO₂ nanopores. (e) Temperature evolution of the (10) Bragg ring for a cooling/heating cycle. $R(T)$ from fig. 4.1(b) serves as a guide to the eye. Insets: Enlarged reciprocal space and diffraction pattern focusing on the (10) Bragg ring. Reprinted with permission from [49]. Copyright American Physical Society 2018.

diffraction ring with intensity maxima close to the equator, but are asymmetric with respect to the equator. This tilt is a direct result of the curved pSiO₂ membrane, see fig. 3.3. Hence, the X-ray beam is not perfectly aligned to the sample resulting in a tilt of the diffractogram of a few degrees. An idealized schematic of the reciprocal space of HAT6 in hydrophilic and hydrophobic pSiO₂ is shown as an inset in figs. 4.2(b) and 4.3(e) for an idealized diffraction geometry ($\omega = 90^\circ$). Despite the similarity the explanation of the diffraction pattern's origin differ.

The only way to distinguish between radial or logpile configuration in hydrophilic pSiO₂ is by determining the coherence length ξ_\perp perpendicular to the long pore axis [25]. Resulting from the large splay distortion the radial configuration leads to ξ_\perp smaller than the pore diameter. In contrast to that, a logpile configuration only shows minor distortions close to the pore wall. Hence, ξ_\perp is expected to be close to the pore diameter. From the diffractogram shown in fig. 4.2(b) a coherence length $\xi_\perp \approx 23$ nm is determined using the Scherrer equation, see eq. (3.17). This value is even larger than the pore diameter ($d = (15.6 \pm 1.9)$ nm) resulting from a large pore size distribution and inaccuracies in the Scherrer equation. Nevertheless, a logpile configuration is present in hydrophilic pSiO₂. Hence, the columns are perpendicular to the pore axis. However, the column direction can differ randomly from pore to pore [25]. Then, only columns that happen to lie parallel to the X-ray beam, hence, the $(100)_\parallel$ domains in the inset in fig. 4.2(a), contribute to a reciprocal ring tangential to the Ewald sphere. All other pores with randomly oriented columns, hence, the $(100)_\perp$ domains and all domains inbetween \parallel and \perp , contribute meridional rings. These rings cut the Ewald sphere at the poles resulting in a maximum intensity at that position.

An enlarged diffraction pattern of HAT6 in hydrophobic pSiO₂ is shown in fig. 4.3(d). The corresponding idealized illustration of the reciprocal space can be found in fig. 4.3(c). The two equatorial intensity streaks represent the quasi-Bragg peaks resulting from a cutting of the Ewald sphere into the Bragg ring of intracolumnar stacking. In contrast to hydrophilic pSiO₂, a coexistence of only two circular concentric domains is present: the $(100)_\perp$ and $(100)_\parallel$ domain orientations, see fig. 4.3(a). When the Ewald sphere cuts in the corresponding (10) rings a twelve-fold diffraction pattern appears, see fig. 4.3(b) and diffractogram of HAT6 in AAO with a pore diameter of $d = 86$ nm shown in table 5.1 in chapter 5. Nevertheless, this twelve fold diffraction pattern is not present. However, the (10) ring can be explained by a randomization of the domain orientations with regard to the averaged pore direction of at least 15° . This randomization results from a sizable tortuosity of single nanopores, similarly as assumed from capillary filling experiments on the untransformed silicon nanopores [94]. It leads to an apparent isotropization of the (10) orientations with a densification towards the poles, see fig. 4.3(c). When the Ewald sphere cuts into the resulting (10) sphere, a Bragg ring with azimuthal intensity maxima at the equatorial poles, in agreement with the observation, is expected. The above described

large tilt is in agreement with the large azimuthal width of the intrastacking peaks at q_{dd} , see fig. 4.3(d). These broad halos are present only at the meridian. This position is in accordance with the circular concentric configuration. There the molecular stacking is dominantly perpendicular to the pore axis following the pores curvature, see fig. 4.3(c). Only at the meridional poles the Ewald sphere cuts into the resulting broad reciprocal ring. The powder like diffraction ring at q values slightly smaller than q_{dd} results from scattering of the amorphous pSiO₂ and is thus a temperature independent background. As described above a logpile configuration with randomly oriented (10) domains results in the same diffraction pattern. However, that configuration wouldn't agree with the discrete layer formation and the edge-on anchoring.

Upon cooling and heating the appearance/vanishing of the $q_{(10)}$ intensity ring in hydrophilic as well as in hydrophobic pSiO₂ can be observed, see figs. 4.2(b) and 4.3(e). Both temperature dependencies follow remarkably well the optical retardation, both in the onset and in the hysteresis width. Only the staircase behavior is barely visible in hydrophobic pSiO₂. However, Monte Carlo simulations, that will be discussed later, suggest that an additional broadening of the steps in the diffraction pattern is present compared to the optical signal. This broadening results from defect healing/formation and reorientation processes in the hexagonal order of the already or still present rings. This leads to continuous (10) intensity change, additionally to the stepwise changes upon layer formation/vanishing. Since the optical retardation is, in contrast to X-ray diffraction, only sensitive to the orientational order it is insensitive to these structural changes. Despite these differences the conclusions drawn for the orientational ordering, extracted from the optical measurements, and translational ordering, extracted from the X-ray diffraction measurements, are conclusive.

Taking a look at the dominant energy contribution of the composite system consisting of HAT6 and hydrophobic pSiO₂ its thermodynamics can be analyzed. Therefore a chemical potential $\Delta\mu$ - temperature T phase diagram, similar to fig. 2.11 and ref. [95], of the confined system with respect to the bulk system close to the bulk transition is shown in fig. 4.1(c). The bulk isotropic liquid chemical potential $\mu_{\text{bulk}}^{\text{iso}}$ (solid line) and its metastable extension for $T < T_{\text{bulk}}^{\text{ci}}$ (dashed line) are plotted at $\Delta\mu = 0$ as a reference. At $T_{\text{bulk}}^{\text{ci}}$ the chemical potential of the bulk columnar phase, whose slope is given by the entropy change ΔS between the isotropic and the columnar phase, intersects with $\mu_{\text{bulk}}^{\text{iso}}$. Measuring the latent heat H of the isotropic-columnar transition [22]

$$\frac{\partial \mu_{\text{bulk}}^{\text{col}}}{\partial T} = -\Delta S = \frac{H}{T_{\text{bulk}}^{\text{ci}}} \quad (4.1)$$

can be determined. Due to supercooling of the isotropic phase inside the pores, the isotropic to columnar phase transition occurs at lower temperatures compared to bulk. These transition temperatures T_n for each ring with $n = 1 \dots 5$ are extracted from the

heating path of the optical retardation measurements in fig. 4.1(b) (marked by red asterix)⁴ and normalized to

$$\Delta t_{h,n} = \frac{T_n - T_{\text{bulk}}^{\text{ci}}}{T_{\text{bulk}}^{\text{ci}}}. \quad (4.2)$$

Then, the chemical potential per molecule in the n th ring can be calculated

$$\frac{\Delta \mu_n^{\text{col}}}{\mu_B} = \frac{\Delta t_{h,n} H m_{\text{mol}}}{N_A k_B} \quad (4.3)$$

with molar mass m_{mol} of HAT6, Avogadro constant N_A , Boltzmann constant k_B and Bohr magneton μ_B . Hence, the transition temperatures mark the energy differences between the metastable bulk liquid and confined columnar phase. The transition in each annular layer n occurs when the excess energy due to the confinement is balanced out by the corresponding supercooling energies.

The dominant mechanism contributing to the excess energy of the rings, and thus to the supercooling of the isotropic phase, is given by the strong bend of the columns, see discussion of resulting excess energy in section 2.2.1. Lattice distortions at the pore wall or at domain walls are neglected in this model. Hence, only the Frank bend elastic energy density per unit length f_{bend} with bend elastic constant K_3 should contribute significantly to the excess energy. Combining eqs. (2.23) and (2.26), given in section 2.2.1, the bending energy for ring n with radius r_n reads

$$f_{\text{bend}} = \frac{K_3}{2} (\hat{n} \times \nabla \times \hat{n})^2 = \frac{K_3}{2} r_n^{-2}. \quad (4.4)$$

The corresponding supercooling energies can be calculated from the normalized temperature differences between subsequent rings i with $i = 1 \dots 4$

$$f_E = \frac{T_i - T_{i+1}}{T_{\text{bulk}}^{\text{ci}}} H \cdot \rho = \Delta t_{h,i} \cdot H \cdot \rho. \quad (4.5)$$

As described above, as soon as the supercooling energy balances out the excess energy the phase transition in each ring occurs. Combining eqs. (4.4) and (4.5) yields

$$\Delta t_{h,i} = \frac{K_3}{2H\rho_{\text{HAT6}}} r_i^{-2}. \quad (4.6)$$

These normalized temperature differences are plotted versus ring radii r_i in the inset of fig. 4.1(b). Performing a fit with eq. (4.6) to the data gives a good agreement with the r^{-2} scaling. In addition, the bend elastic constant $K_3 = (2.7 \pm 0.7)$ pN can be extracted as a fit parameter. It is in reasonable agreement with the one reported for the chemically closely related HAT7 $K_3 = 4$ pN [96]. This otherwise hard to determine material constant

⁴Here the heating path is chosen because less interactions between molecules and pore surface alter the phase transition compared to the cooling path.

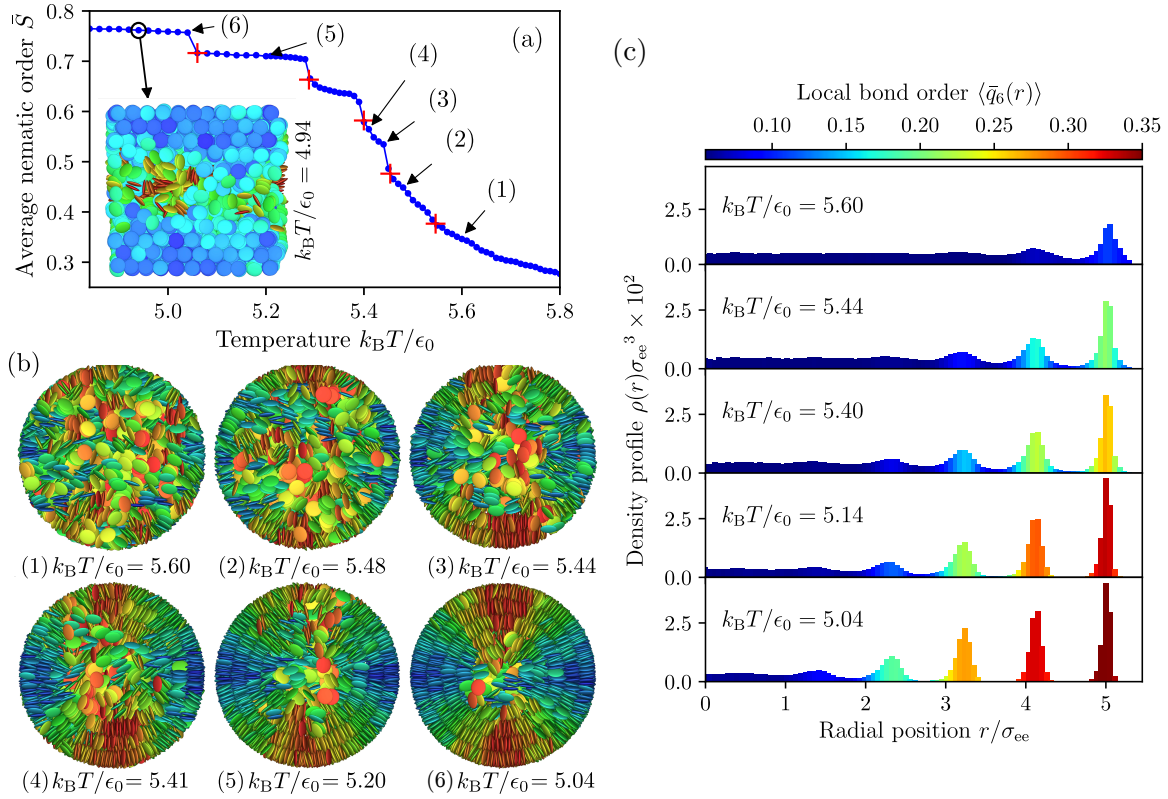


Figure 4.4.: Monte Carlo simulations. (a) The average nematic order parameter \bar{S} as a function of the temperature shows discontinuous steps marked with red crosses. Inset: Cross-section of the molecular arrangement in one pore. (b) Top-view snapshots of the molecular orientation at the temperatures marked as (1...6) in panel (a). (c) Local density $\rho(r)$ and bond orientational order parameter \bar{q}_6 as a function of the radial position shown at five different temperatures along the quantized phase transition. With decreasing temperature five distinct concentric rings appear. Reprinted with permission from [49]. Copyright American Physical Society 2018.

gives a value for the stiffness of the columns, e.g. how easy they bend.

To obtain a microscopic picture of the molecular ordering in hydrophobic pores parallel-tempering Monte Carlo simulations were performed by our collaborators at the MPI in Göttingen [50]. Employing a Gay-Berne-II model, N DLC molecules in the isothermal-isobaric ensemble expanded by temperature were simulated, see details of the simulation method in the supplemental of [49]. The temperature dependence of the so simulated average order parameter \bar{S} , see fig. 4.4(a), can be directly compared to the optical retardation measurement, see section 3.2.2. In agreement with the experimentally determined molecular ordering in fig. 4.1(a), a stepwise increase in the simulated orientational order is present as the temperature decreases. Additionally, fig. 4.4(b) shows typical molecular configurations extracted from the Monte Carlo simulations at different temperatures marked in (a). These snapshots, showing top views along the long pore axis, are in accordance with the circular concentric configuration determined by the experiments. Upon decreasing temperature $k_B T / \epsilon_0$, whereby ϵ_0 represents the fluid-fluid interaction energy, ring by ring appears only leaving a disordered core in the pore center. This can also be

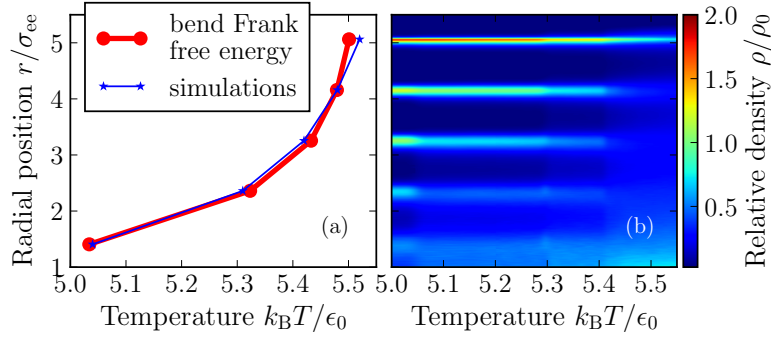


Figure 4.5.: (a) The ring's radial position as a function of the transition temperatures. The Monte Carlo simulations agree with the r^{-2} -scaling of the bend Frank free energy. (b) Temperature dependence of density profile. With decreasing temperature five distinct regions of large density appear, corresponding to the circular concentric layers. Reprinted with permission from [49]. Copyright American Physical Society 2018.

seen in the cross-section snapshot in fig. 4.4(a). Figure 4.4(c) shows the radial density profile $\rho(r)$ and local bond order parameter $\bar{q}_6(r)$, determining the extend of columnar hexagonal ordering, as a function of the radial position r/σ_{ee} inside the pore for five different temperatures with σ_{ee} representing the molecules diameter. Both parameters are closely connected. As soon as a concentric ring emerges, the orientations within it are strongly correlated. As can be seen in fig. 4.4(c) a paranematic state is present at high temperature. With decreasing temperature ring after ring emerges, see larger values of \bar{q}_6 . Note that the appearance of new rings leads to an increase in the bond orientational order of the already present rings resulting from widespread disappearances of defects. This supports the interpretation of the differences in the X-ray and optical experiments made above. As the temperature decreases below the fifth transition at $k_B T/\epsilon_0 = 5.06$, strong orientational order permeates the system. Only the pore center stays a defect region. So upon decreasing temperature the molecules become much more localized within circular concentric configurations and form hexagonal columnar arrangements, see inset in fig. 4.4(b). Each new ring results in an increased density in the previous layers, so that at lowest temperature five regions of enhanced density are visible, corresponding to the circular concentric configurations.

The temperature dependence of the radial ring position r/σ_{ee} extracted from the temperature evolution of the density profile is plotted in fig. 4.5(a). Since the pore center shows a defect with a strong gradient of local nematic order a term proportional to $(\nabla S)^2$ as well as the dependence $K \propto S^2$ are included in the calculation of the Frank free energy. The plot shows that the simulations support the model that the ring curvatures cause the quantized transition since the bend Frank free energy prediction of a r^{-2} -scaling is in good agreement with the simulation.

All in all, the experimental and simulation data for HAT6 in hydrophobic pSiO₂ complement each other perfectly. Small differences result from the fact, that the experiments

always cover multiple nanopores. Hence, the results are affected by local and global geometry variations. Only prospective single-pore experiments could yield results on how these different disorder contributions result in a smearing of the observed compared to the theoretically expected quantization.

5. Tailoring photonic metamaterial properties by discotic self-assembly in nanopores¹

The DLC HAT6 is filled in nanoporous AAO with hydrophilic and hydrophobic pore surfaces as described in 3.2.1. The samples are investigated by temperature dependent optical birefringence, X-ray diffraction measurements and by complementary differential scanning calorimetry (DSC) and dielectric spectroscopy (DS) measurements performed at Bundesanstalt für Materialforschung (BAM) in Berlin [97]. To prove reproducibility, also in cooperation with BAM, up to six samples per pore diameter and surface anchoring were prepared.

In the following sections the phase transition behavior is first analyzed by the optical measurements detecting solely orientational ordering. The results are supported by DSC and DS measurements and afterwards correlated with X-ray diffraction experiments giving detailed information about the translational ordering. Finally, the metamaterial photonic properties of the resulting configurations are analyzed and discussed.

5.1. Phase transition, supercooling and hysteresis

Figure 5.1 shows the optical retardation $R(T)$ as a function of temperature for multiple pore diameters in (a)-(j) hydrophilic and (k)-(t) hydrophobic AAO directly opposed allowing a direct comparison. The surface modification in order to achieve edge-on anchoring in hydrophobic AAO is described in detail in section 3.1.2. All $R(T)$ curves in fig. 5.1 are normalized by the thickness and porosity of the membranes, see table A.1 in appendix A. Starting from the isotropic phase, above the isotropic-columnar phase transition temperature $T_{\text{bulk}}^{\text{ci}}$ marked by the dashed line, $R(T)$ either decreases or increases with decreasing temperature. Similar to the measurements discussed in chapter 4 an increase (decrease) with decreasing (increasing) temperature indicates, in agreement with the negative dielectric anisotropy of DLCs, an orientation of the columns and thus the director perpendicular to the pore axis ($\hat{n} \perp p$) [21]. A positive birefringent material with

¹Parts of the results discussed in this chapter will be published in reference [86].

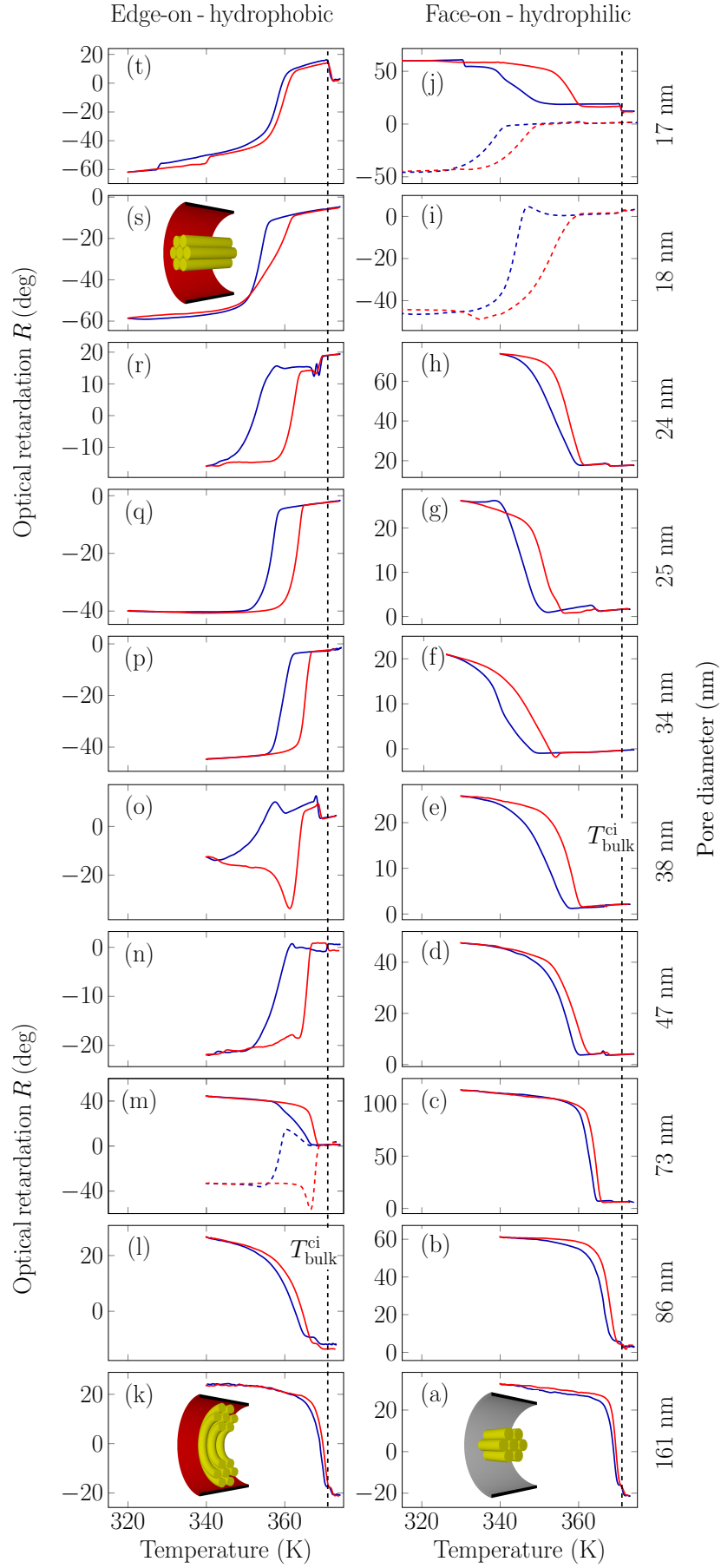

 Figure 5.1: *continued*

Figure 5.1.: Temperature dependent optical retardation $R(T)$ of HAT6 confined in (a)-(j) hydrophilic (face-on anchoring) and (k)-(t) hydrophobic (edge-on anchoring) AAO for pore diameters in between 17 nm - 161 nm. The dashed line indicates the bulk isotropic to columnar phase transition temperature $T_{\text{bulk}}^{\text{ci}}$ determined from the measurement shown in fig. 4.1. The insets in (a), (k) and (s) show the logpile, circular concentric and axial molecular orientation respectively.

$\Delta R \sim \Delta n > 0$ is realized. Again three different configurations described in detail in section 2.2.1 are possible: the logpile configuration with lattice distortions at the periphery of the wall [25], the radial configuration with splay distortions that are highest in the center of the pore [20] and the circular concentric configuration with bend distortion that are also highest in the pore center [24, 49]. Which configuration occurs strongly depends on the surface anchoring conditions and can ultimately only be distinguished by the coherence lengths extracted from X-ray diffraction experiments [25]. A decrease (increase) with decreasing (increasing) temperature indicates, again in agreement with the negative dielectric anisotropy of DLCs, an orientation of the columns and thus the director \hat{n} parallel to the pore axis p ($\hat{n}_{\parallel p}$), i. e. an axial orientation. A negative birefringent material with $\Delta R \sim \Delta n < 0$ is realized. The dominant distortions present in this configuration are lattice distortions at the periphery of the pore.

In hydrophilic AAO the optical retardation increases (decreases) with decreasing (increasing) temperature for pore diameters down to 24 nm, see fig. 5.1(a-h). As described above this behavior indicates a molecular orientation with the director and thus the columns perpendicular to the pore axis comparable to the data reported in ref. [21]. Resulting from the face-on anchoring condition a radial or logpile configuration is possible [20, 25]. The radial configuration has only been reported for pores smaller than 20 nm [20]. Thus, more likely the logpile configuration is present here, see inset in fig. 5.1(a).

Interestingly, for pore diameters smaller than 24 nm the molecular orientation switches from logpile to axial, see dashed lines in fig. 5.1(i,j). There the optical retardation decreases (increases) with decreasing (increasing) temperature. However, this axial orientation is not consistent with the face-on surface anchoring. Additionally, the orientational transition is accompanied by a color change of the membranes. During the filling procedure described in section 3.2.1 they become brown-colored, see fig. A.3 in appendix A. The longer the filling time and the smaller the pore diameter the darker becomes the membrane. Inbetween filling times of 8 h and 15 h the molecular orientation switches from logpile to axial, see fig. A.3 in appendix A and solid line in fig. 5.1(j). The membranes' color changes are not observed in hydrophobic AAO, where surface species cover the bare AAO surface. As described in section 3.2.1 up to 5 wt% anions of the acids used during preparation are integrated into the amorphous AAO. Pores with diameters $d \leq 34$ nm are produced using sulfuric acid (H_2SO_4). Resulting from its highly polar ends sulfuric acid is hygroscopic. Since the native hydrophilic AAO surface is covered by -OH and H_2O

molecules the HSO_4^- anions can react with these surface species changing the membranes' color to brown. The long preparation time, in addition to the high preparation temperature, might enhance this reaction. More importantly it influences the hydrophilicity of the native AAO surface to be more hydrophobic. The smaller the pore diameter, the higher is the surface-to-volume ratio and, hence, the surface molecule interaction. Because of the unknown surface anchoring conditions the two measurements shown in fig. 5.1(i,j) (dashed lines) will not be included in further analysis. Only the measurement performed after 8 h filling is further analyzed, see straight line in fig. 5.1(j). Since the pores are smaller than 20 nm also a radial orientation is possible [21].

In hydrophobic AAO the optical retardation increases (decreases) with decreasing (increasing) temperature for pore diameters down to 73 nm. In accordance with the edge-on anchoring a circular concentric configuration with the director perpendicular to the pore axis but parallel to the pore wall is present, see inset in fig. 5.1(k). Resulting from large geometric frustration an isotropic core is present in the pore center. However, the dashed curve in fig. 5.1(m) already indicates an orientational transition to a new regime.

Down to a pore diameter of 38 nm the optical retardation first increases upon cooling down from the isotropic phase followed by a strong decrease. This behavior indicates that a mixture of axial and circular concentric orientations is present. Thereby the axial orientation is present in the center of the pore where the geometric frustration from the circular concentric configuration would be highest and is thus replaced. Upon heating the optical retardation strongly decreases indicating again an orientational transition from circular concentric to axial. Hence, the axial core expands. As soon as also the axial core melts, the optical retardation strongly increases again. This co-existence is supported by differential scanning calorimetry measurements performed at identical samples at BAM in Berlin. The measured endotherm peaks split up into two or three satellite peaks that can be assigned to phase transitions of different configurations close to the pore wall (circular concentric) and in the pore center (axial) [97]. Such a behavior and orientational transition within one pore size has to our knowledge not been reported before.

Taking a look at the pore size dependence of the respective excess energies a critical pore diameter d_c for the orientational transition in between axial and circular concentric configuration can be determined, see section 2.2.1. The excess energy increases linearly with $d/2$ for the axial configuration, but proportional to $\ln(d/2)$ for the circular concentric configuration [24]. Hence, the critical pore diameter can be determined to $d_c = 73$ nm. For pores larger than d_c a pure circular concentric configuration is favored. The transition regime to the axial configuration exceeds down to $d = 38$ nm. This indicates that for these pore sizes only small energy differences exist inbetween both orientational configurations. For even smaller pore diameters starting at 34 nm solely an axial orientation is present. The optical retardation decreases (increases) with decreasing (increasing) temperature. Pure axial orientation of neat HAT6 in AAO has to our knowledge never been achieved

before. Even chemical modification with silanes, i. e. silanization, in order to favor edge-on anchoring did not achieve this configuration [24]. This proves, that functionalization by phosphonic acid is more stable in comparison to silanization as discussed in section 3.1.2. The above described orientational configurations of HAT6 in hydrophilic and hydrophobic AAO are in agreement with complementary dielectric spectroscopy² measurements performed at identical samples at BAM in Berlin [97].

In addition, preliminary conductivity measurements of HAT6 confined in hydrophobic pores with $d = 38$ nm were performed. As discussed above, this pore size yields a dominantly axial orientation necessary for a potentially measurable conductivity along the pore channel. Therefore, both sample sides were sputtered with approx. 100 nm gold. However, neither measurements using a standard volt meter nor measurements employing a simple lock-in technique revealed any significant conductivity. This indicates, that the resistance is higher than 10 G Ω . This is supported by preliminary conductive atomic force microscopy (AFM) measurements performed on a HAT6 filled hydrophobic sample with $d = 161$ nm, see ?? in appendix A. This sample, not having the axial orientation, shows an increased current of only a few hundred nanovolt inside the pores compared to the surrounding amorphous AAO structure. Note, however, that all conductivity measurements were performed at room temperature, hence, in the crystalline phase. Additionally, preliminary single pore X-ray diffraction measurements at the P10 beamline at DESY suggest that even in the liquid crystalline phase the pore space may not be filled completely. This will, especially in the low temperature crystalline phase, hamper the conductivity.

All phase transitions in fig. 5.1 show a temperature hysteresis of varying width between cooling and heating path. For the circular concentric and radial configurations the hysteresis' origin can be found in the location of the distortions present in the structural organization of the molecules giving rise to an increase in its free energy. An isotropic core is present in the pore center due to large geometric frustration that prohibits the formation of columns. Upon cooling the phase transition starts at the pore wall propagating towards the isotropic center. Surface-molecule interaction can delay the appearance of the columnar phase leading to a supercooling of the isotropic phase [20]. Upon heating the phase transition is nucleated in the isotropic core expanding towards the pore wall. In the logpile and axial orientation lattice distortions are present at the periphery of the pore wall. That is why one might suggest that the pathway is the opposite compared to the circular concentric and radial configuration. As already discussed in chapter 4 Monte Carlo simulations showed that the pore wall also imposes some kind of ordering [50]. This surface induced ordering results in suppressing of molecular fluctuations and thus triggers the columnar phase to appear close to the pore wall. Hence, also for the

²Applying an external electric field parallel to the long pore axis allows to measure the complex dielectric permittivity. This technique is sensitive to the dipole orientation that lies within the plane of the disk shape molecules. Hence, the orientational order can be probed by monitoring the dipole orientation. More details can be found in [97].

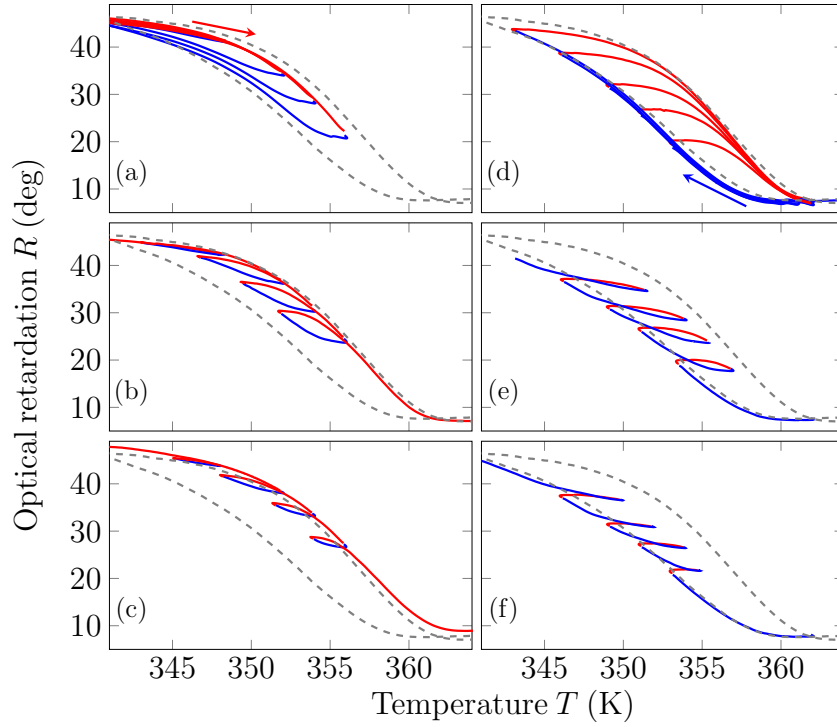


Figure 5.2.: Small temperature hystereses corresponding to the same sample shown in fig. 5.1(e). Effects are shown for the (a-c) heating and (d-f) cooling paths for varying step sizes ($\Delta T = 1 - 4$ K). The dashed gray line indicates a full hysteresis.

axial and logpile configurations the phase transition starts at the pore wall upon cooling and propagates towards the pore center. Again upon heating it starts in the pore center expanding towards the pore walls.

To further investigate the temperature hysteresis, small temperature hystereses are performed on hydrophilic AAO with 38 nm pores, see fig. 5.2. As discussed above the optical retardation in combination with the hydrophilic pore surface suggest a logpile configuration. Multiple hystereses with varying step sizes ($\Delta T = 1 - 4$ K) upon heating, see fig. 5.2(a-c), and cooling, see fig. 5.2(d-f), are conducted. Upon heating the phase transition starts in the pore center. Hence, the curve starts to follow the full hysteresis path (gray dashed line). Subsequent cooling back to the initial temperature results in small hysteresis effects. The larger the temperature step the more propagates the phase transition towards the pore wall. Hence, the pore wall surface's influence increases resulting in a larger hysteresis. Not going back to the initial temperature results in small hystereses that get broader the higher the temperature and the step size get, see fig. 5.2(b,c). Upon cooling down from the isotropic phase the phase transition starts at the periphery of the pore wall. The hysteresis again follows the full hysteresis path, see fig. 5.2(d). Upon subsequent heating back to the initial temperature hystereses of almost same width independent of the turning point are present. Not going back to the initial temperature and for smaller temperature step sizes the hysteresis almost vanishes, see fig. 5.2(e,f). All these effects support the picture that the phase transition is strongly influenced by surface

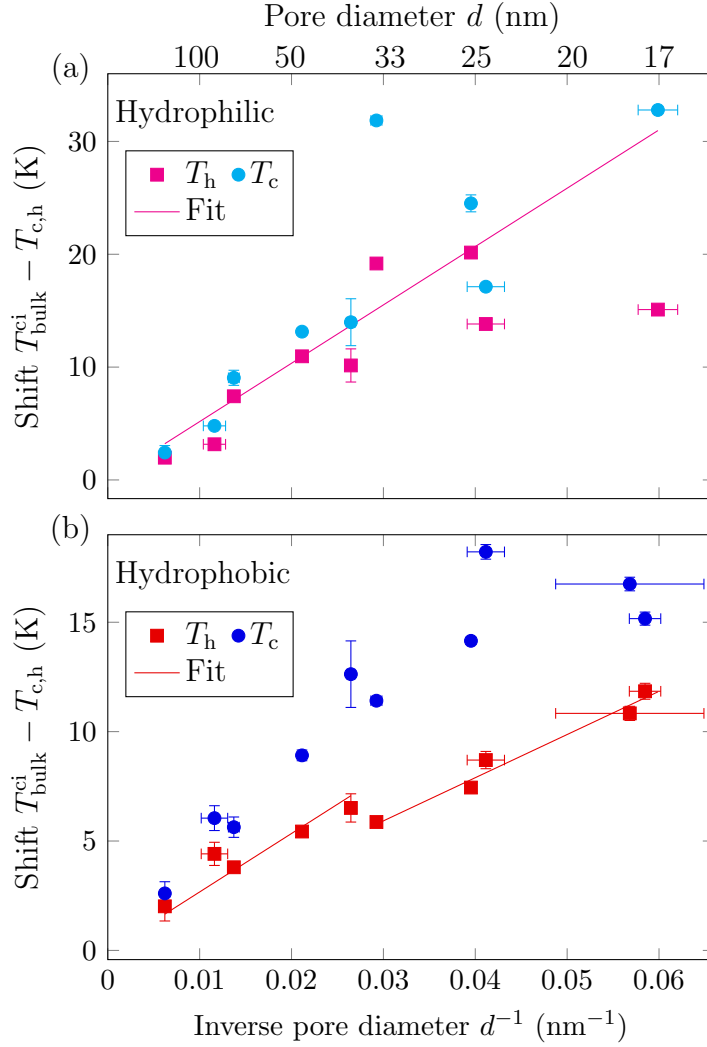


Figure 5.3.: Phase transition temperatures shift $T_{\text{bulk}} - T_{\text{c,h}}$ of HAT6 embedded in (a) hydrophilic and (b) hydrophobic AAO plotted as a function of the inverse pore diameter d^{-1} compared to bulk behavior. For clarity also the pore diameter d is indicated. The straight lines are fits according to the Gibbs-Thompson equation, see eq. (2.34). The phase transition temperature values $T_{\text{c,h}}$ are averaged values extracted from optical retardation measurements in fig. 5.1 and additional measurements (not shown) to prove reproducibility.

molecule interactions, especially in hydrophilic AAO where no surface species cover the pore wall and soften the geometric constraints.

The $R(T)$ curves in fig. 5.1 can be used to determine the isotropic-columnar transition temperatures by taking the maximum of the derivative dR^2/dT [20]. In all pore sizes and for both surface anchoring conditions the phase transition is shifted to lower temperatures compared to the bulk transition at $T_{\text{bulk}}^{\text{ci}}$ indicated by the vertical dashed lines in fig. 5.1. Theoretically this decrease with decreasing pore diameter d can be described within the Gibbs-Thomson model, see eq. (2.34). The determined phase transition temperature shifts with respect to the bulk transition temperature $T_{\text{bulk}}^{\text{ci}} - T_{\text{c,h}}$ is plotted depending on the inverse pore diameter in fig. 5.3 for (a) hydrophilic and (b) hydrophobic AAO. Shown are the extracted average values for all samples investigated within three subsequent cooling,

giving T_c , and heating paths, giving T_h . The larger the shift, the greater differs the phase transition temperature compared to bulk. Inversely, $T_{\text{bulk}}^{\text{ci}} - T_{\text{c,h}} = 0 \text{ K}$ means equality. For HAT6 in hydrophilic AAO the transition temperature shift continuously increases with decreasing pore diameter down to $d = 38 \text{ nm}$. At $d = 34 \text{ nm}$ the shift strongly increases. The only difference of membranes with pore diameters $d \geq 38 \text{ nm}$ and $d \leq 34 \text{ nm}$ is the acid used during the preparation procedure, see table A.1 in appendix A. So the strong deviation from the theoretically d^{-1} dependence is attributed to the influence of the sulfur ions implemented into the amorphous AAO structure, see EDX measurement in fig. 3.6. Since upon cooling the phase transition starts at the pore wall the interaction between molecules and pore surface strongly influences the phase transition behavior. Thus, the above described trend is less pronounced in the phase transition temperature extracted from the heating path. Further decrease in pore size leads again to an increased temperature shift, followed by a decrease at $d = 17 \text{ nm}$. Note that the latter sample was prepared with a filling time of only 8 h, see fig. A.3 in appendix A. So a direct comparison has to be treated with care. Additionally, an orientational transition at 20 nm from logpile to radial is possible [21].

The phase transition temperature shift appears in a more continuous way in hydrophobic AAO, see fig. 5.3(b). This fact supports the strong surface influence in hydrophilic AAO described above. Since the AAO surface is now covered by a rather thick layer of surface species more stable surface anchoring conditions are present that are not influenced by any atoms inside the amorphous AAO structure. The phase transition temperature shift extracted from the heating path continuously increases with decreasing pore diameter down to $d = 38 \text{ nm}$. At $d = 34 \text{ nm}$, coinciding with the orientational transition from a circular concentric to axial configuration, the shift first slightly decreases followed by a continuous increase for even smaller pore diameters. Again, this trend is much more pronounced upon heating.

In general the phase transition shift is much smaller in hydrophobic than in hydrophilic AAO. Additionally, for the smallest pore diameter the hysteresis almost vanishes in hydrophobic compared to hydrophilic AAO. Thus, the modification softens the geometric constraints at the periphery of the wall.

Since the heating path for hydrophobic/hydrophilic AAO shows the least influence of surface molecular interactions a fit according to the Gibbs-Thompson model is performed to this data for each orientation respectively. Since the molecules' density ρ and T_{Bulk} are independent of the confinement, only the surface tension σ and phase transition enthalpy ΔH are chosen as fit parameters. The fits deliver $(\sigma/\Delta H)_{\text{axial}} = (0.2027 \pm 0.003) \text{ mg/m}^2$ and $(\sigma/\Delta H)_{\text{CC}} = (0.2692 \pm 0.007) \text{ mg/m}^2$ for HAT6 in hydrophobic and $(\sigma/\Delta H)_{\text{logpile}} = (0.532 \pm 0.049) \text{ mg/m}^2$. Assuming that the phase transition enthalpy in confinement equals that of bulk ($\Delta H = (7.1 \pm 0.3) \text{ J/g}$) [22]) the resulting surface tensions are $\sigma_{\text{axial}} = (1.43 \pm 0.02) \text{ mN/m}$, $\sigma_{\text{CC}} = (1.91 \pm 0.67) \text{ mN/m}$ and $\sigma_{\text{logpile}} = (3.76 \pm 0.35) \text{ mN/m}$. These

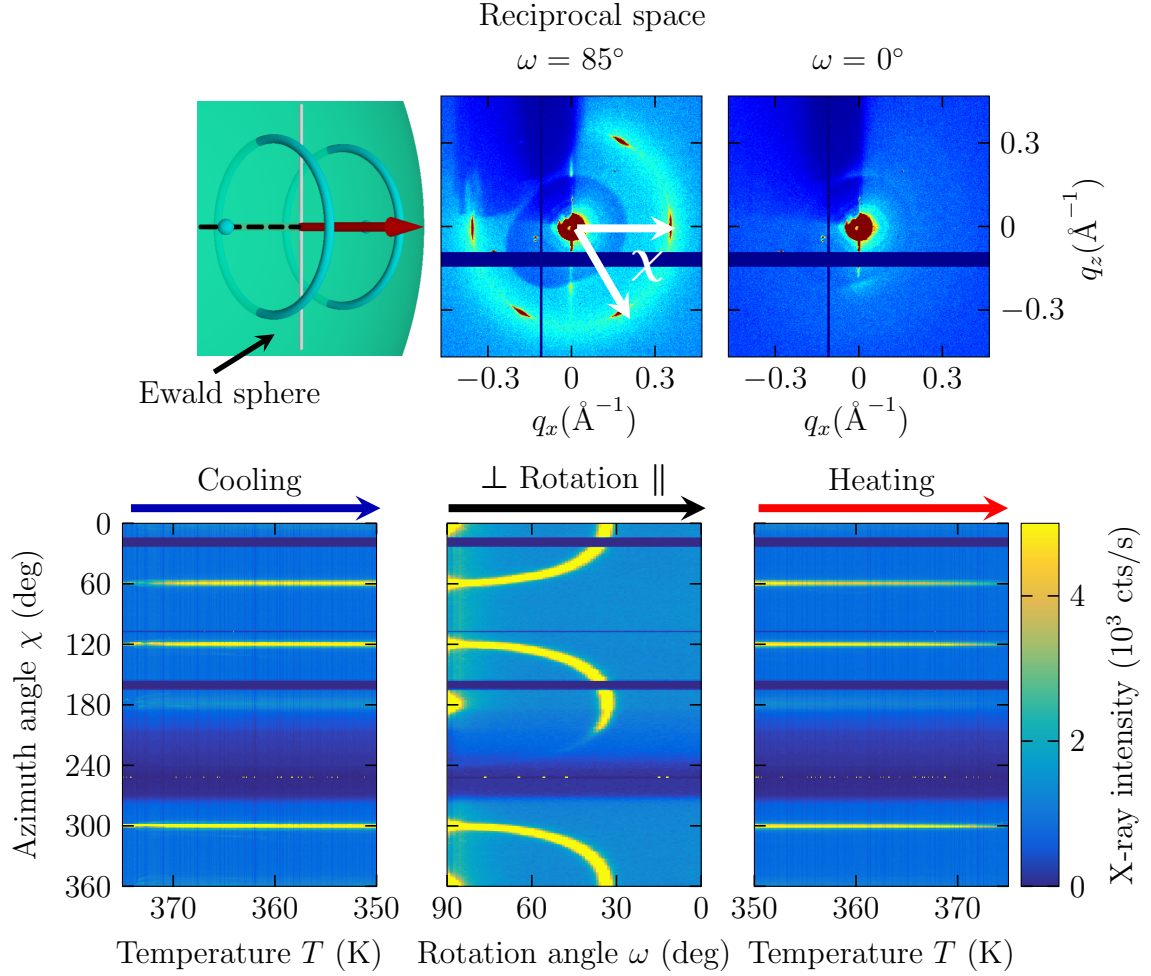


Figure 5.4.: Exemplary data set of HAT6 in hydrophilic AAO pores with $d = 161$ nm. (Top) Illustration of reciprocal space at $\omega = 85^\circ$ and diffractograms showing Bragg intensities at $q_{(10)} = (0.34 \pm 0.01) \text{ \AA}^{-1}$ characteristic of columnar hexagonal phase for $\omega = 0^\circ$ and 85° . Also indicated is the definition of azimuth angle χ . (Bottom) Exemplary presentation of axis labeling for Bragg intensities shown in table 5.1. Plotted are intensities for a cooling ($\omega = 85^\circ$), sample rotation ($\omega = 90^\circ \rightarrow 0^\circ$) and heating ($\omega = 85^\circ$) scan extracted for each azimuth angle χ .

values are in good agreement with those extracted from differential scanning calorimetry measurements performed at Bundesanstalt für Materialforschung (BAM) in Berlin [97] and previous reported results [22] .

5.2. Structure analysis

The 2D diffraction patterns for HAT6 in hydrophilic and hydrophobic pores were recorded as described in section 3.2.3. Again resulting from the lateral dimensions of the HAT6 molecule, see section 3.1.1, Bragg peaks can be observed at a wave vector transfer $q_{(10)} = (0.34 \pm 0.01) \text{ \AA}^{-1}$, typical of the (10) Bragg reflection of hexagonal intercolumnar order. In addition, halos at $q_{dd} = (1.77 \pm 0.01) \text{ \AA}^{-1}$ characteristic of the intracolumnar disk-disk stacking can be observed.

Due to limited beam time five pore diameters showing distinct orientational ordering as discussed in section 5.1 are measured for each anchoring condition. Starting in the isotropic phase ($T > T_{\text{bulk}}^{\text{ci}} = 371.1 \text{ K}$) images were taken upon cooling/heating. Sample rotation angles close to 90° show strong adsorption effects. Hence the temperature scans were performed at $\omega = 85^\circ$. This configuration still probes the translational molecular order within cross-sections aligned along \hat{p} and the vertical direction along the pore diameter. Additionally, ω sample rotations, i.e. a rotation from a configuration with $q_i \perp \hat{p}$ ($\omega = 90^\circ$) to $q_i \parallel \hat{p}$ ($\omega = 0^\circ$) are performed after cooling down to the columnar phase. Using the Scherrer equation, see eq. (3.17), the diffraction patterns taken at lowest temperature at $\omega = 85^\circ$ are used to determine the coherence lengths along and perpendicular $\xi_{\parallel}/\xi_{\perp}$ to the long pore axis. Additionally, in order to study the kinetics of the self-assembly in confinement, cooling/heating rate (0.2 K/min and 1 K/min) dependent measurements on hydrophobic pores were performed. Again due to limit beam time only two pore diameters were investigated ($d = 17 \text{ nm}$ and 38 nm).

At first the structure of HAT6 in hydrophilic and hydrophobic AAO will be discussed separately. Afterwards, the results will be correlated to the orientational ordering obtained by the optical birefringence measurements discussed in section 5.1.

5.2.1. Face-on molecular anchoring in hydrophilic nanochannels

Table 5.1 shows X-ray diffraction measurements for a selected set of pore diameters for native, hydrophilic pore walls³. Diffractograms at $\omega = 85^\circ$, the resulting real and reciprocal space as well as a cooling, sample rotation and heating scan are shown. Exemplary the diffractogram of the largest pore diameter, $d = 161 \text{ nm}$, as well as the associate cooling, sample rotation and heating scans are shown enlarged in fig. 5.4. The diffractogram at $\omega = 0^\circ$, where the wave vector transfer q_i is parallel to the long pore axis \hat{p} , shows no diffraction peaks. Upon increasing sample rotation angle, close to $q_i \perp \hat{p}$, a six-fold diffraction pattern appears. This diffraction pattern results from one $\{100\}$ plane set perpendicular to \hat{p} . This $(100)_{\perp}$ domain is illustrated in table 5.1. The optical birefringence measurements discussed in the previous section suggest two possible configurations for a hydrophilic pore surface, either a logpile [25] or a radial orientation [20]. Both configurations can explain this diffraction pattern. The Bragg intensity distribution in reciprocal space, as illustrated in table 5.1, results from a randomization, hence, rotation, of an hexagon around \hat{p} for both cases leading to the formation of two reciprocal rings and two spots on the equatorial line⁴. For $\omega = 85^\circ$ the Bragg condition is fulfilled at six positions, where the Ewald sphere cuts in reciprocal space into this intensity distribution.

³The samples were cooled down to 350 K for $d = 161 \text{ nm}$, 86 nm and 73 nm, 340 K for $d = 38 \text{ nm}$ and 320 K for $d = 17 \text{ nm}$, see fig. 5.7.

⁴The meridian and equator are defined with respect to the rotation axis, i.e., meridian is vertical, equator horizontal.

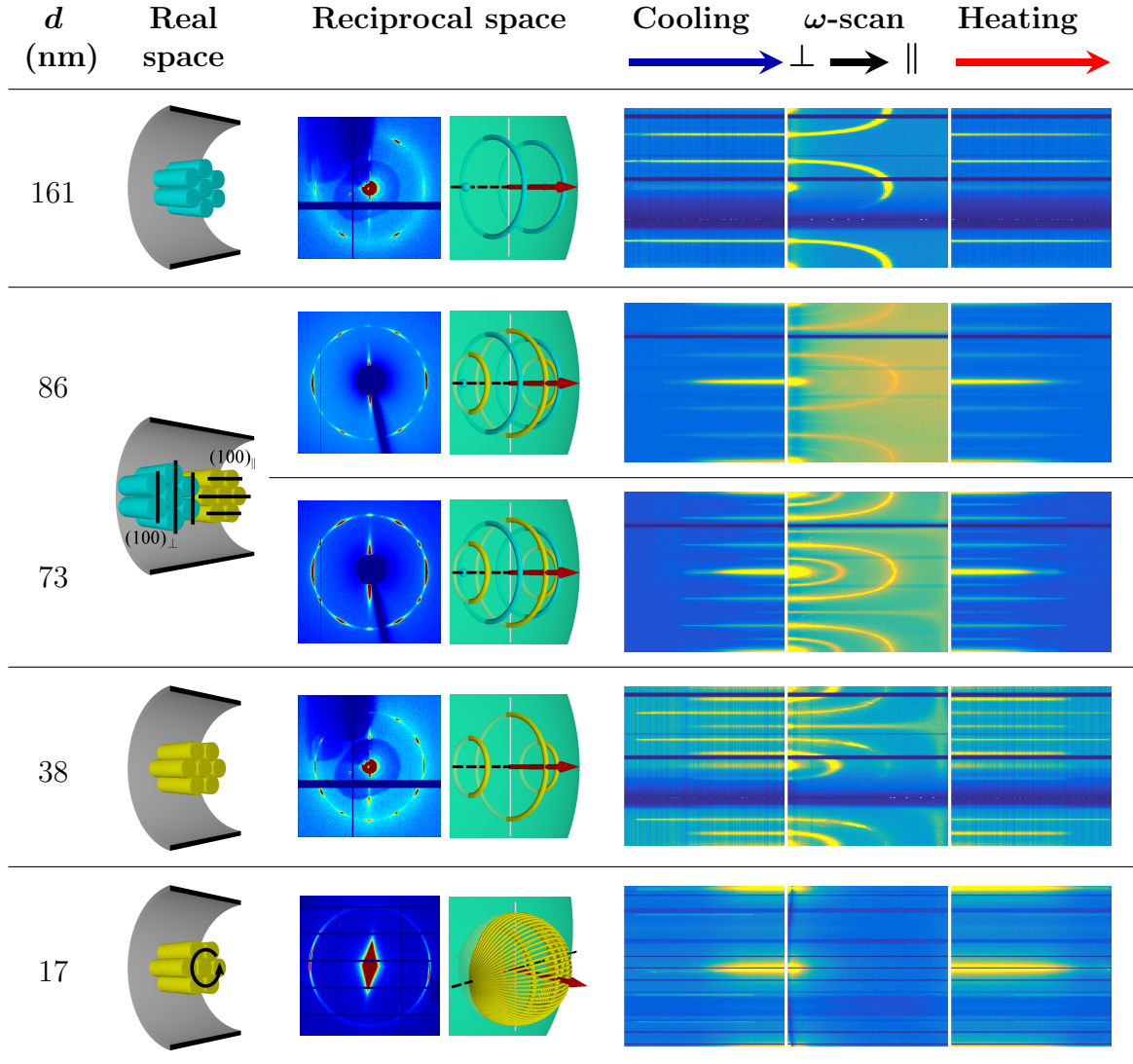


Table 5.1.: Self-assembly of discotic molecules in hydrophilic cylindrical nanopores (face-on molecular anchoring). (From left to right) Real and reciprocal space images and diffractograms of molecular order. The black dashed line represents the pore axis. Corresponding Bragg intensities as inferred from 2D reciprocal space mappings. Bragg intensities as a function of temperature for a cooling ($\omega = 85^\circ$), sample rotation ($\omega = 90^\circ \rightarrow 0^\circ$) and heating ($\omega = 85^\circ$) scan extracted for each azimuth angle χ . See definition of azimuth angle and axis labeling in fig. 5.4.

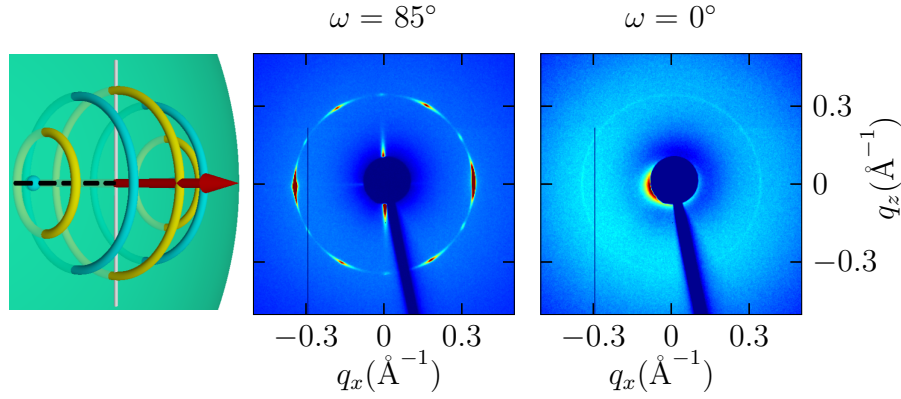


Figure 5.5.: Exemplary data set of HAT6 in hydrophilic AAO with $d = 86$ nm. Illustration of reciprocal space at $\omega = 85^\circ$ and diffractograms showing Bragg intensities at $q_{(10)} = (0.34 \pm 0.01) \text{ \AA}^{-1}$ characteristic of columnar hexagonal phase for $\omega = 0^\circ$ and 85° .

Upon rotation to $\omega = 0^\circ$ the Bragg condition is not fulfilled anymore, since no part of the reciprocal intensity distribution cuts the Ewald sphere. This is in agreement with the intensity contour plots of the ω -scan in fig. 5.4 and table 5.1. It shows the intensity at a wave vector transfer $q_{(10)}$ as a function of azimuthal angle χ and sample rotation angle ω starting from a $q_i \perp \hat{p}$ to $q_i \parallel \hat{p}$ orientation. Initially one observes six Bragg peaks in azimuthal direction as discussed above. Upon ω rotation the Bragg condition of the $(100)_\perp$ planes is not fulfilled any more. They vanish, whereas the χ position of the other plane sets starts to move towards the meridian and equatorial directions, respectively, in perfect agreement with a rotation of the ring structures depicted in table 5.1.

Whether a logpile or radial configuration is present can only be distinguished by calculating the coherence length along the equatorial line. In the case of the logpile structure the domain size, i. e. the coherence length perpendicular to \hat{p} , ξ_\perp should be on the order of the pore diameter [25]. Whereas in the case of radial columns it is expected to be much smaller. An analysis based on the (100) peaks, properly accounting for the instrumental broadening, results in $\xi_\perp = 153$ nm, see fig. 5.6. This value is only slightly smaller than the nominal pore diameter and thus indicates a logpile arrangement of the molecules.

Additionally, fig. 5.4 and table 5.1 show X-ray diffraction patterns upon cooling from, and subsequent heating back into the isotropic phase at $\omega = 85^\circ$. Again the Bragg intensity at a wave-vector transfer typical of the columnar self-assembly is plotted as a function of azimuthal angle χ and temperature. For $d = 161$ nm the appearance/disappearance of the Bragg intensities characteristic of $(100)_\perp$ domain can be observed as a function of temperature.

With decreasing pore diameter the pattern changes from a six-fold to a twelve-fold pattern at $\omega = 85^\circ$, see table 5.1. Again for clarity enlarged diffraction patterns for $d = 86$ nm are shown in fig. 5.5 for $\omega = 85^\circ$ and 0° . The diffraction pattern results from an appearance of a second orientational domain rotated by 30° with respect to the $(100)_\perp$ domain. Thus, this domain shows $\{100\}$ set of planes parallel to \hat{p} , i. e. a $(100)_\parallel$ domain. An illustration

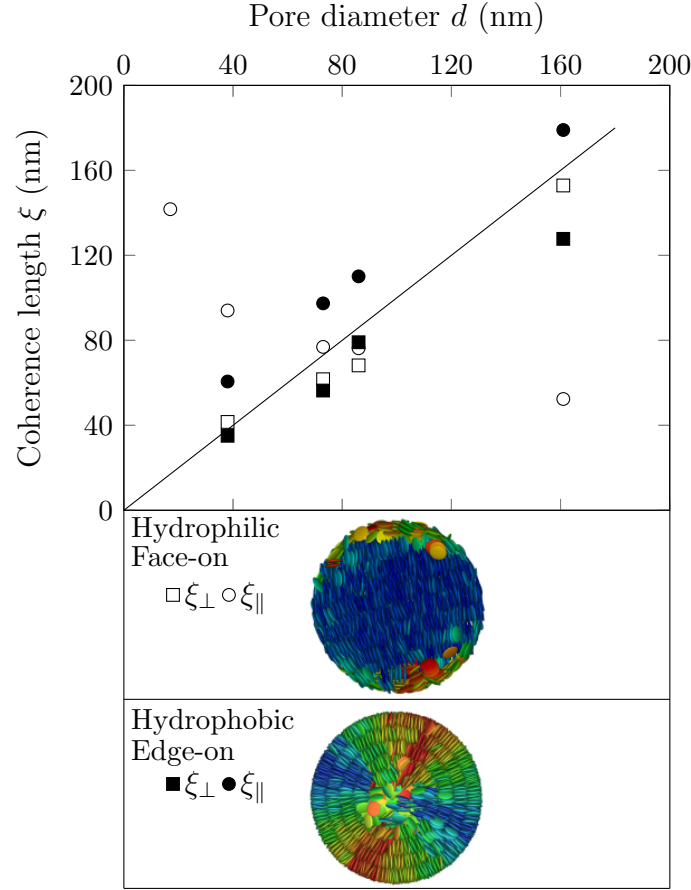


Figure 5.6.: Coherence lengths parallel ξ_{\parallel} and perpendicular ξ_{\perp} to the long pore axis as a function of channel diameter and hydrophobicity of pore walls. Shown are $\xi_{\perp/\parallel}$ for the logpile configuration in hydrophilic and the circular concentric configuration in hydrophobic pores. The straight line yields theoretical values for $\xi_{\perp} = d$.

of this texture characterized by the coexistence of two orientational domains is shown in table 5.1 along with the corresponding Bragg intensity distribution in reciprocal space. Again resulting from the rotation of both hexagonal domains around \hat{p} five diffraction rings and two spots on the equatorial line appear. Upon decreasing rotation angle the diffraction patterns change, so that only a powder like diffraction ring at $\omega = 0^\circ$ remains. In this configuration the Bragg condition is only fulfilled for the largest reciprocal ring that lies flat on the Ewald sphere. The ω -rotation contour plots in table 5.1 are compatible with the existence of these two domain states down to $d = 73$ nm. Again the correlation lengths are on the order of the pore diameter, see fig. 5.6. A logpile structure is established. Upon further decreasing the pore diameter, a transition from a twelve-fold pattern to a six-fold pattern is present. This means that only one of the orientational domains survives, i.e. the $(100)_{\parallel}$ domain. The correlation length and the ω -Bragg intensity contour map are again compatible with the logpile structure.

At the smallest pore diameter, a diffraction pattern with two strong intensity halos on the equatorial line is detected. Similar as discussed in chapter 4 it can be understood by

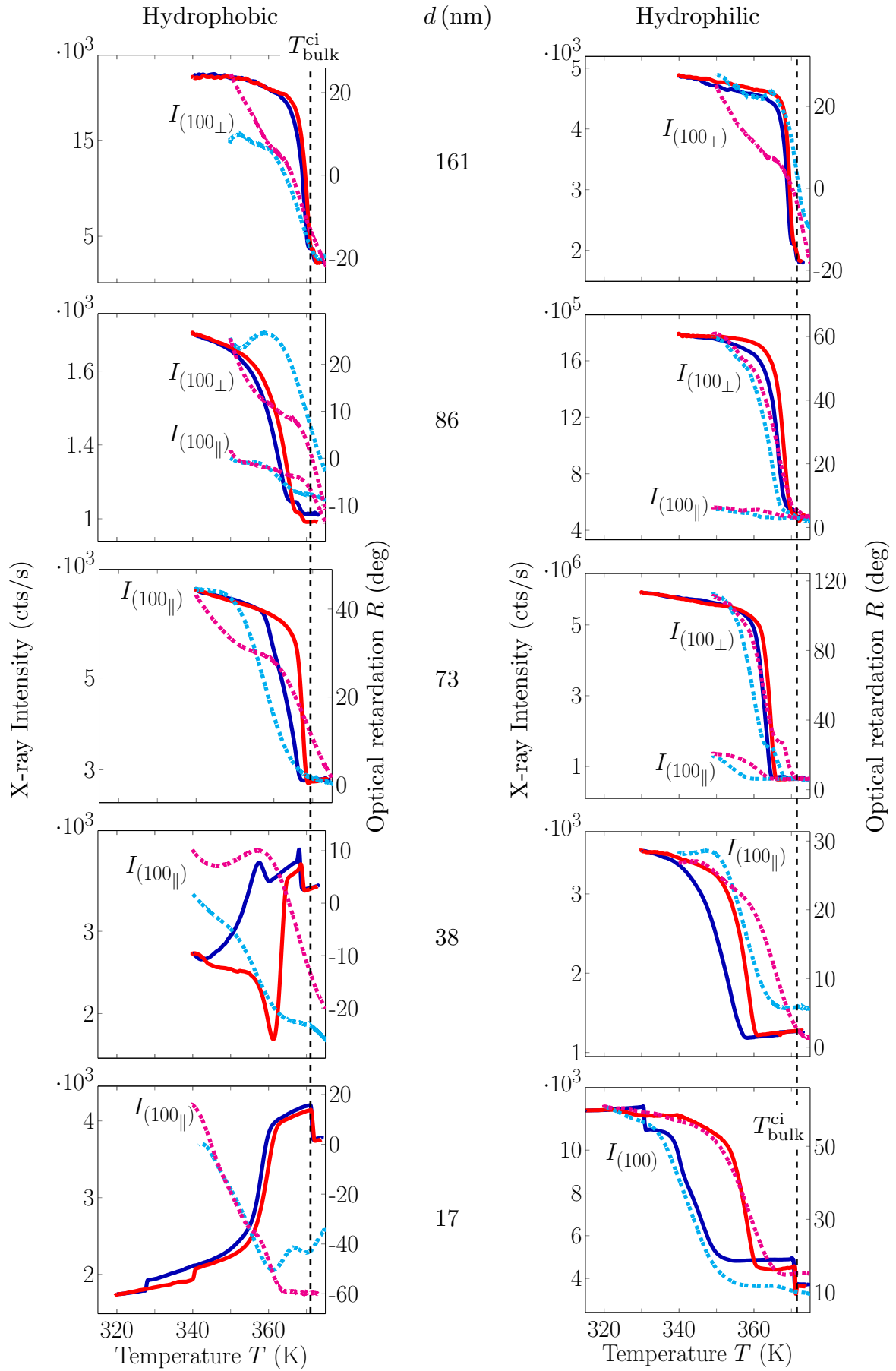

 Figure 5.7: *continued*

Figure 5.7.: Temperature evolution of the X-ray intensity (dashed lines) for hydrophilic and hydrophobic AAO typical of the hexagonal columnar translational order at $q_{(10)} = (0.34 \pm 0.01) \text{ \AA}^{-1}$ for pore diameters indicated in the center. The optical retardation measurements from fig. 5.1 (solid lines) are shown again allowing a direct comparison. The black dashed line indicates the bulk isotropic to columnar phase transition temperature $T_{\text{bulk}}^{\text{ci}}$ determined from the measurement shown in fig. 4.1.

a logpile structure along with a randomization of the $[\text{hk}0]$ directions with regard to the long pore axis. Not only $(100)_{\parallel}$ and $(100)_{\perp}$ domains, but also all domains inbetween are present. This effect results in a densification of the Bragg intensities towards the equatorial directions as is illustrated in table 5.1 [25].

In addition to the coherence length perpendicular to the pore diameter ξ_{\perp} , the coherence length along the long pore axis ξ_{\parallel} is calculated from the detected Bragg peaks. The smaller the pore diameter the larger it gets, see fig. 5.6. Hence, the increased confinement strength induces stronger hexagonal ordering resulting in large well ordered domains parallel to the pore axis.

The above described findings are in excellent agreement with the observations and interpretations of Zhang et al. [25]. In particular the logpile structures and the change of the orientational domain texture with regard to the long pore axis as a function of d . It has been established for crystallization in unidirectional confinement that extreme textures can arise resulting from the competition of fast growing crystallization along the long channel axis, i. e. Bridgman growth in narrow capillaries, with crystallization constraints and/or molecular anchoring at the pore walls. The $(100)_{\perp}$ orientation can presumably be traced to Bridgman growth, if one assumes that the $\langle 100 \rangle$ direction is a fast growing mode and thus is aligned along \hat{p} . As discussed in detail by Zhang et al. for the smaller pore diameters an increasing contribution of splay deformations at the pore walls sets in. These defect structures are also found in Monte Carlo simulation studies and can be more easily established in the $(100)_{\parallel}$ orientation [25, 49]. Thus, the above described orientational domain transition results from a transition from a Bridgman-growth determined to a splay-deformation determined orientational state as a function of reducing pore diameter.

Additionally, to the diffraction patterns discussed above, and complementary to the results published by Zhang et al. [24, 25], table 5.1 shows X-ray diffraction patterns upon cooling from, and subsequent heating back into the isotropic phase at $\omega = 85^{\circ}$. This temperature dependent translational self-assembly is compared to the temperature dependent optical retardation experiments regarding the evolution of the orientational order in confinement discussed in the previous section. Figure 5.7 shows the intensities of different Bragg peak sets, extracted from contour plots in table 5.1, corresponding to the characteristic domain states upon cooling (blue) and heating (red) in comparison with the optical retardation. The Bragg intensity evolves quite analogous to the optical retardation.

tion upon cooling and heating for all pore diameters. The confinement renders the phase transition to be more continuous than the abrupt first-order bulk transition. As discussed in the previous section the increase (decrease) with decreasing (increasing) temperature indicates an alignment of the columns perpendicular to the pore axis. This is in perfect agreement with the conclusion drawn from the X-ray diffraction experiments regarding the translational logpile order.

Especially for the smallest pore diameter, a large hysteresis between heating and cooling is present in the X-ray intensity. It is in excellent agreement with the evolution of the collective orientational concerning the hysteresis width as well as its onset. Moreover, the temperature-evolution indicates that the $(100)_{\parallel}$ domain appears much weaker and at lower temperatures compared to the $(100)_{\perp}$ orientation in the case of a coexistence of these domains. This is particularly obvious for pores with $d = 73 \text{ nm}$ ⁵. This behavior is in agreement with the assumption that the $(100)_{\perp}$ domain is the fast growing (Bridgman growth) mode and can thus be established more easily.

5.2.2. Edge-on molecular anchoring in hydrophobic nanochannels

Table 5.2 shows X-ray diffraction measurements for a selected set of pore diameters for surface-grafted, hydrophobic pore walls⁶. Again diffractograms at $\omega = 85^\circ$, the resulting real and reciprocal space as well as a cooling, sample rotation and heating scan are shown. For the largest pore diameter ($d = 161 \text{ nm}$) again a six-fold diffraction pattern, a $(100)_{\perp}$ domain, is recorded. This pattern, as well as the sample rotation contour plot, is identical to the one for the hydrophilic membranes. However, resulting from the hydrophobic, edge-on anchoring, and in agreement with positive birefringent properties detected by the optical retardation measurements, a circular concentric configuration with a single domain is realized here. In reciprocal space this again results in the formation of two reciprocal rings and two diffraction spots on the equatorial line that cut the Ewald sphere in the used scattering geometry ($\omega = 85^\circ$) at six points. The circular concentric configuration is also supported by the fact that the calculated coherence length ξ_{\perp} perpendicular to the pore axis is smaller than the pore diameter, see fig. 5.6. Resulting from the ring formation the hexagonal structure perpendicular to the pore is not as pronounced as it is for the logpile configuration.

For the next smaller pore diameter, again identical to the hydrophilic membranes, a twelve-fold diffraction pattern is detected. Again the ω -intensity contour plots can be understood as resulting from two orientational domains with regard to \hat{p} , a $(100)_{\parallel}$ and $(100)_{\perp}$ domain, as illustrated in table 5.2. In agreement with this configuration is the

⁵Note that for the 38 nm sample we observe significant scattering from a bulk film, presumably located at the outer membrane surface. This results in the appearance of Bragg peaks at temperatures much higher than for the confined liquid crystal and in the twelve-fold diffraction pattern.

⁶The samples were cooled down to 350 K for $d = 161 \text{ nm}$ and 86 nm and 340 K for $d \leq 73 \text{ nm}$.

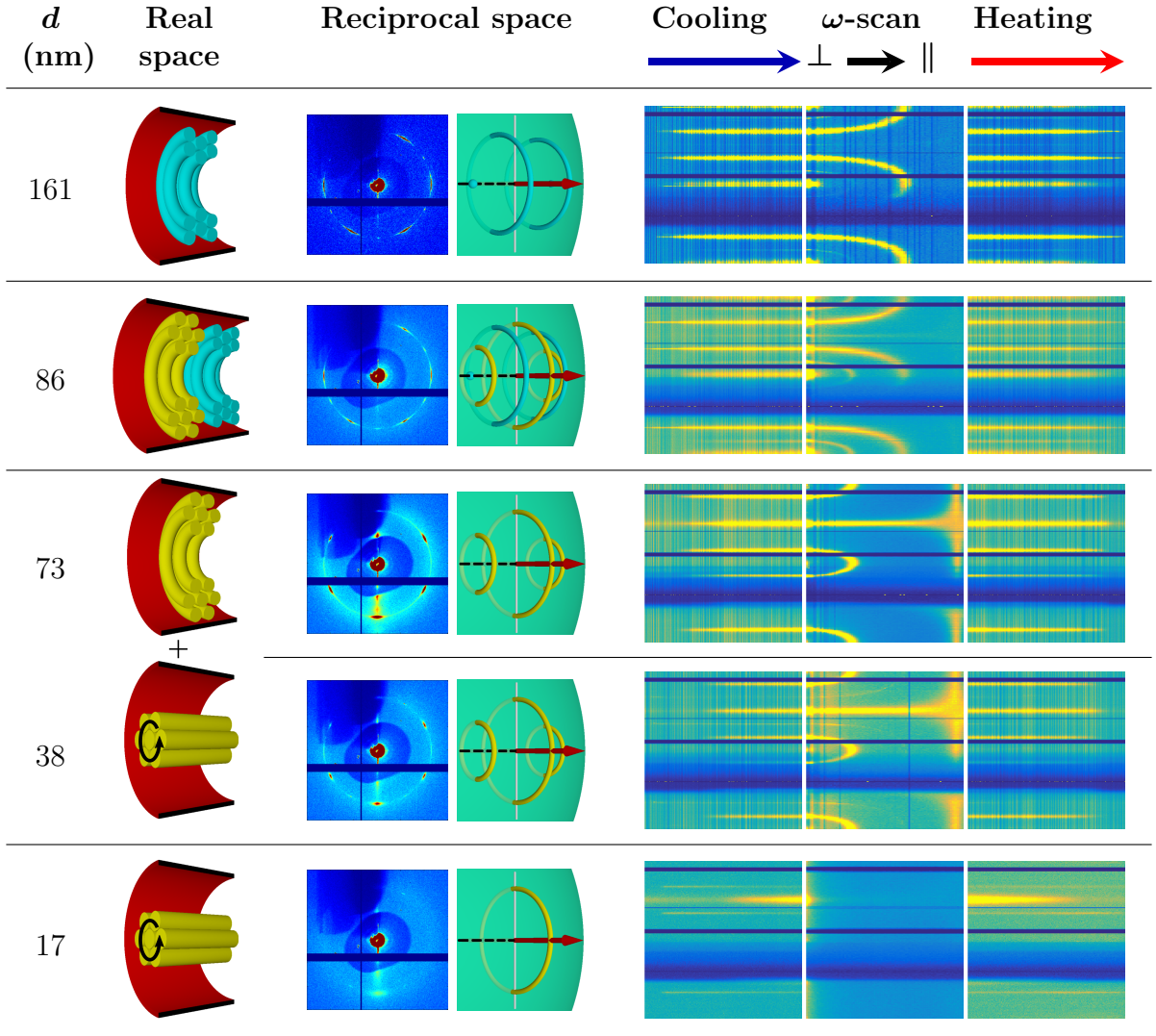


Table 5.2.: Self-assembly of discotic molecules in hydrophobic cylindrical nanopores (edge-on molecular anchoring at pore walls). (From left to right) Real and reciprocal space images and diffractograms of molecular order. The black dashed line represents the pore axis. Corresponding Bragg intensities as inferred from 2D reciprocal space mappings. Bragg intensities as a function of temperature for a cooling ($\omega = 85^\circ$), sample rotation ($\omega = 90^\circ \rightarrow 0^\circ$) and heating ($\omega = 85^\circ$) scan extracted for each azimuth angle χ . See definition of azimuth angle and axis labeling in fig. 5.4.

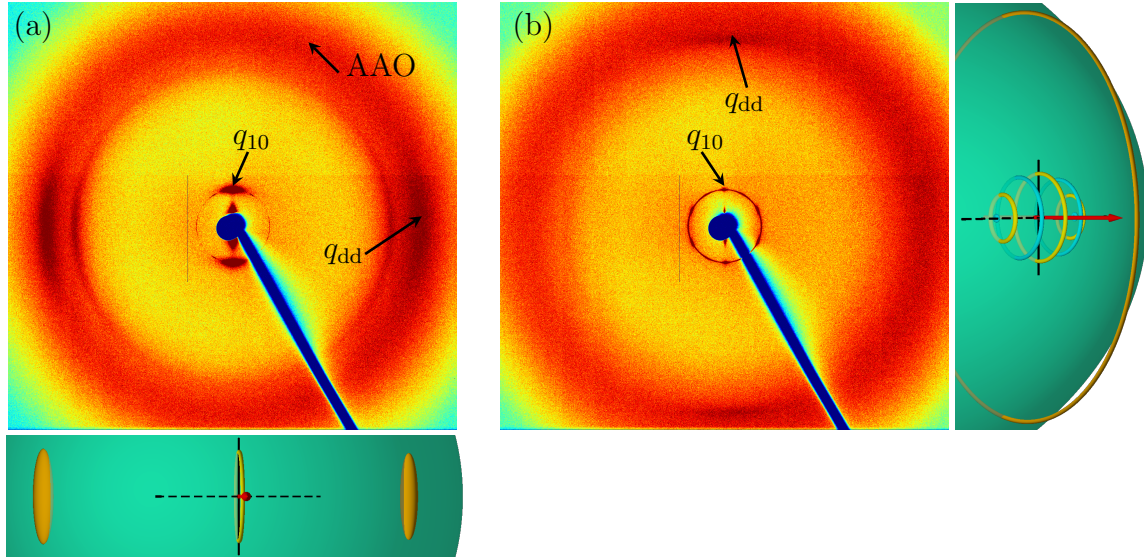


Figure 5.8.: Wide-angle diffractograms for hydrophobic AAO with (a) 17 nm and (b) 86 nm pores showing Bragg streaks at $q_{dd} = (1.77 \pm 0.01) \text{ \AA}^{-1}$ resulting from the disk-disk stacking (a) along the pore axis (on equator) and (b) perpendicular to it (on meridian). Additionally, schematics of the reciprocal space in the used scattering geometry idealized for $\omega = 90^\circ$ are shown. The temperature independent intensity distribution at large q -values present over the entire azimuth results from scattering inside porous AAO.

position of the intracolumnar disk-disk peak at $q_{dd} = (1.77 \pm 0.01) \text{ \AA}^{-1}$, see fig. 5.8(b). Resulting from the circular concentric configuration the molecular stacking is dominantly present perpendicular to the pore axis leading to broad halos on the meridional line.

For even small pore diameters down to $d = 38 \text{ nm}$ only a six-fold pattern remains, compatible with the existence of the $(100)_\perp$ orientation. More importantly, upon sample rotation to small angles the ω -contour plots evidence that a strong Bragg peak on the meridian at $\chi = 90^\circ$ occurs. At $\omega = 0^\circ$ this Bragg ring results in a powder like diffraction ring present over the entire azimuth. The additional scattering in the polar directions result from a domain state with columns parallel to \hat{p} , i.e. axial columns. Resulting from a complete randomization of the hexagonal structure around \hat{p} , see table 5.2, this axial domain leads to an additional Bragg ring that superimposes with that from the circular concentric configuration, leading to strong scattering on the meridional line. Hence, a coexistence of a circular concentric and axial configuration in agreement with the orientational ordering discussed in the previous section is present.

For the smallest pore diameter, $d = 17 \text{ nm}$, the hexagonal patterns are only marginally detectable. Polar intensities are present on the meridional line, hence, almost purely axial columnar arrangement is realized. Additionally, the coherence length ξ_\perp , see fig. 5.6, extracted for directions perpendicular to the pore axis is in excellent agreement with the pore dimension supporting the picture of pure axial alignment. This configuration results in diffraction spots condensed in one ring cutting the Ewald sphere at two spots on the vertical axis. This disk-disk stacking along the pore axis is confirmed by the position of

the intracolumnar disk-disk peak at $q_{dd} = (1.77 \pm 0.01) \text{ \AA}^{-1}$ on the equatorial line, see fig. 5.8(a).

Again it is interesting to compare the temperature dependence of these diffraction results with the optical experiments, see fig. 5.7. The qualitative behavior is almost similar to the observations in hydrophilic pores. A rather gradual evolution of the Bragg intensities compared to the sharp bulk transition is present. Moreover, the different domains occur and vanish at slightly different temperatures and a transformation from one domain state to the other is present. For the largest pores this competition occurs for pores in the size range between 86 nm and 161 nm just between positive birefringent contributions, i. e. between the $(100)_{\parallel}$ and $(100)_{\perp}$ domains. As discussed in the previous section the increase (decrease) with decreasing (increasing) temperature indicates an alignment of the columns perpendicular to the pore axis. This is in perfect agreement with the conclusion drawn from the X-ray diffraction experiments regarding the translational circular concentric order for pores down to 38 nm. However, in case of 38 nm and 73 nm pores axial and circular concentric order competes as can be seen in the optical retardation, by competing positive and negative contributions respectively, as well as in the X-ray intensities. This behavior also manifests itself in the coherence lengths ξ_{\parallel} parallel to the long pore axis, see fig. 5.6. With decreasing pore size, as soon as the competition between circular concentric and axial sets in, the coherence lengths and thus the domain size starts to decrease. This competition leads to a non-monotonous behavior both upon cooling and heating as can be seen in the optical retardation and in the X-ray intensities ($d = 38 \text{ nm}$). For the smallest pore diameter, in agreement with the negative birefringence, the X-ray intensities indicate an orientation of the in-plane disk orientation perpendicular to \hat{p} in excellent agreement with the formation of an almost purely axially aligned columnar state inferred from the diffraction experiments. Additionally, the temperature evolution and almost non-existent hysteresis in the X-ray intensities is in perfect agreement to the optical retardation.

In order to study the kinetics of the self-assembly in confinement, cooling/heating rate dependent measurements on hydrophobic pores were performed. Table 5.3 shows the intensity at q_{10} plotted as a function of azimuthal angle χ and temperature comparing directly the “slow” (0.2 K/min) and “fast” (1 K/min) cooling.

For the smaller pore diameter, $d = 17 \text{ nm}$, and the fast cooling rate a gradual but monotonous formation of the axial formation is observed, in agreement with the discussions above. By contrast, for the slow cooling rate upon temperature decrease the q_{10} peak is spread over the entire 360° azimuthal range, indicating a complete randomization of the columnar axis direction with regard to \hat{p} . Only below 350 K the axial orientation eventually starts to dominate and an almost pure axial configuration with the columnar axis parallel to the long pore axis is achieved. Upon heating this pure axial discotic texture melts to the isotropic state without a complete randomization. The axial textural state is also documented by the ω scans depicted in table 5.3, whose course is indepen-

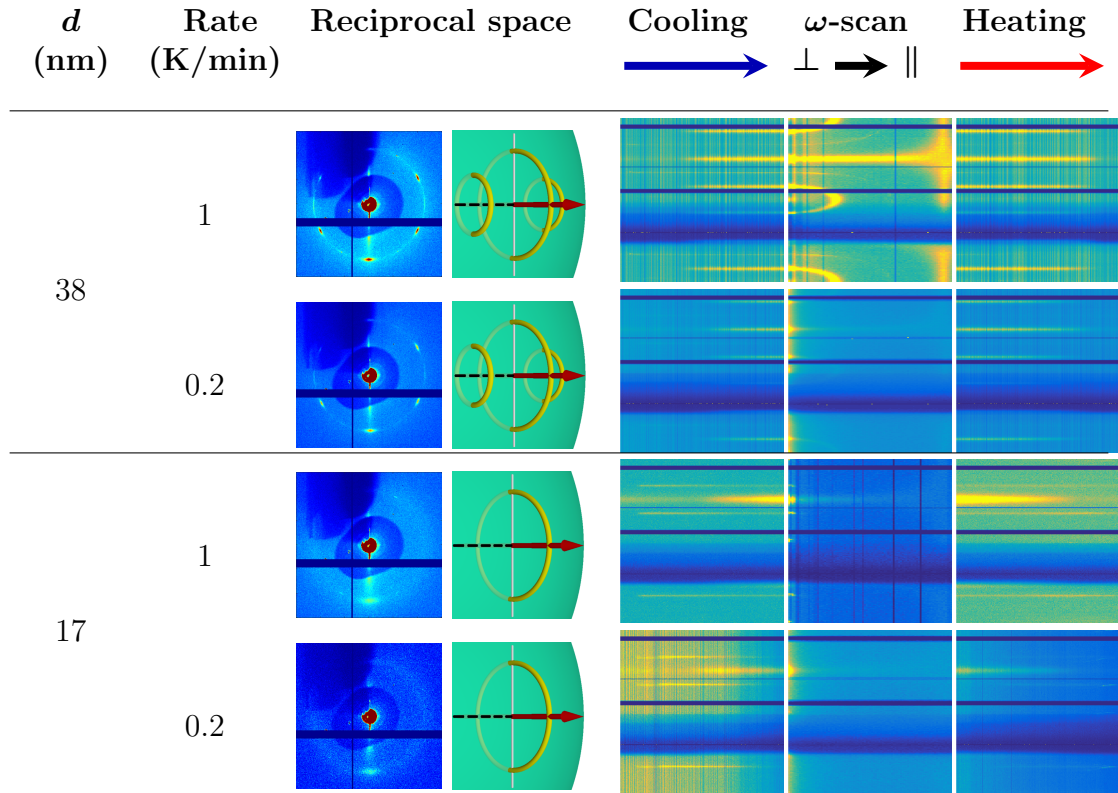


Table 5.3.: Temperature and rotation scans depending on the cooling/heating rate for HAT6 in hydrophobic AAO with two different pore diameters. (From left to right) Reciprocal space images and diffractograms of molecular order. Corresponding Bragg intensities as inferred from 2D reciprocal space mappings. Bragg intensities as a function of temperature for a cooling ($\omega = 85^\circ$), sample rotation ($\omega = 90^\circ \rightarrow 0^\circ$) and heating ($\omega = 85^\circ$) scan extracted for each azimuth angle χ . See definition of azimuth angle and axis labeling in fig. 5.4. The temperature scans were performed for each sample and cooling/heating rate inbetween 340 K \longleftrightarrow 370 K.

dent of the cooling/heating rate. This sensitivity of the self-assembly process is also nicely documented for the slightly larger channels, $d = 38 \text{ nm}$. For the fast cooling rate the coexistence of axial and circular concentric states, as discussed above, is observed. Remarkably, however, for the slow cooling regime an almost pure axial arrangement is induced, not observed so far for this large pore diameter. Only at high rotation angles close to $\omega = 90^\circ$ the reciprocal space agrees with a coexistence of circular concentric and axial configuration. However, taking a closer look the X-ray intensities suggest that this orientational domain is less pronounced for the fast cooling/heating rate.

Overall, the presented results indicate that the typical time-scales of the self-assembly process are well within typical experimental cooling rates in our experiments. To the best of our knowledge, there is barely any experimental or theoretical data on the self-assembly kinetics of bulk not to mentioned confined discotics [84, 98]. The few studies available rather consider the columnar-to-crystalline state. At least, the substantially slow transformation kinetics on the order of hours have been inferred from X-ray diffraction experiments [84]. Thus, these observations are not too surprising and highlight the importance of the consideration of cooling/heating rates with respect to tailoring columnar discotic order by nanotemplating.

5.3. Metamaterial properties

As discussed in section 3.2.2 a hybrid material made up of two components with different optical properties and structural dimensions at the wavelength of visible light can be considered a metamaterial. By employing an effective medium model an effective refractive index \bar{n} can be calculated, see eq. (3.13). Hence, the liquid crystal filled meso- and macropores of AAO ($d = 17 \text{ nm} - 161 \text{ nm}$) can be considered metaatoms of the resulting soft-hard metamaterial.

To analyze the above discussed results regarding their potential as metamaterial photonic materials, a brief summary of the found configurations and the resulting optical properties is given below. As discussed in detail in section 5.1 at low temperature in the columnar hexagonal phase hydrophilic pores solely yield positive retardations R , while hydrophobic pores yield sizeable positive and negative retardations, see fig. 5.1. To summarize this orientational order, in combination with the translational order determined by the X-ray diffraction experiments and the supercooling of the isotropic-to-columnar phase transition, two phase diagrams are shown in fig. 5.9. Shown is the pore size and temperature dependent formation of the columnar phase and the resulting optical anisotropy in confinement. At high temperature in the confined isotropic liquid phase the indicatrix representing the optical anisotropy, hence, birefringence, see section 2.3.2, is a sphere. Phase transition temperatures of the heating path of the optical retardation measurements are plotted again for the (a) logpile and (b) circular concentric and axial configuration. The solid

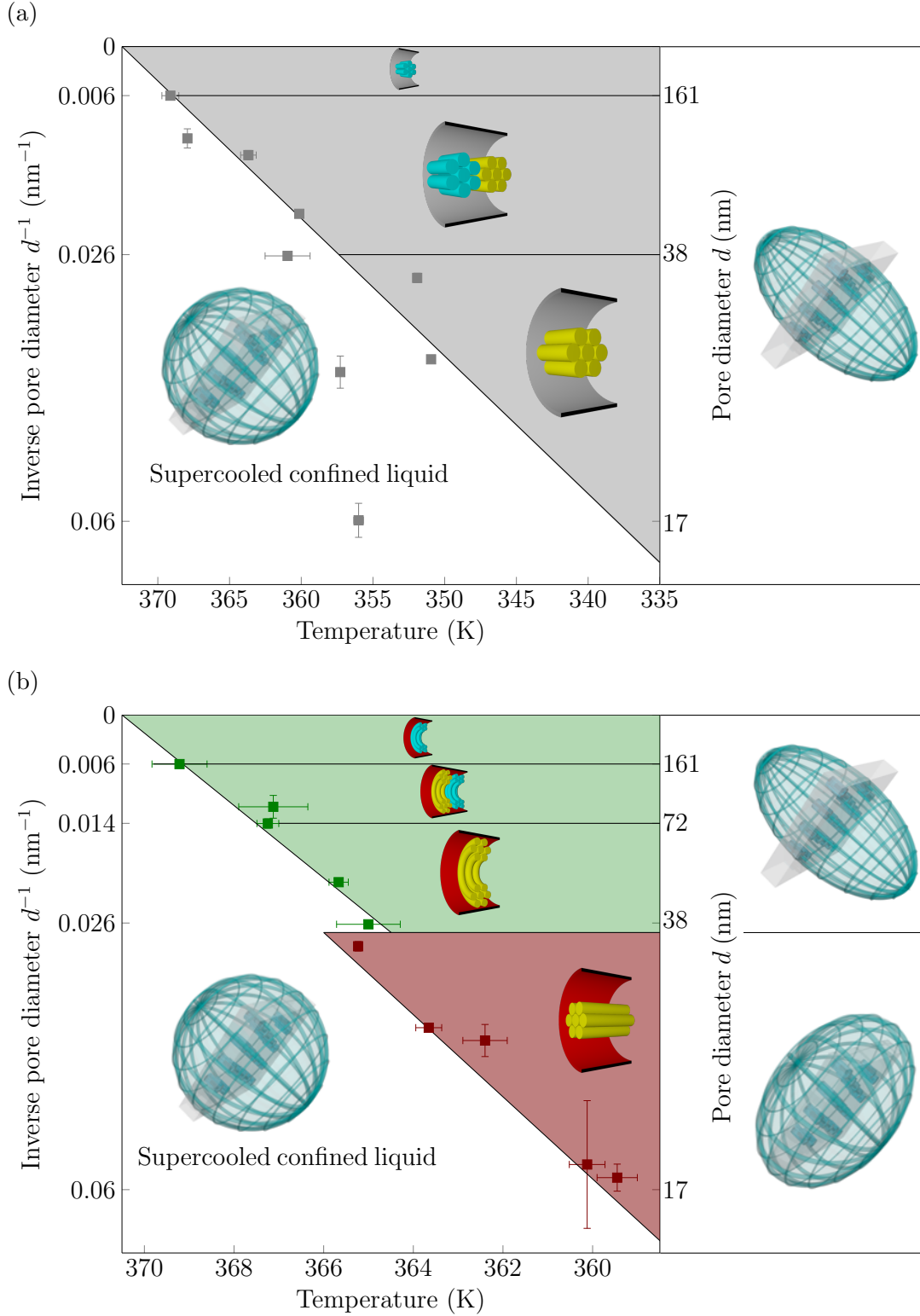


Figure 5.9.: Phase diagram and effective optical anisotropy as a function of pore size and temperature dependent resulting configurations in (a) hydrophilic and (b) hydrophobic AAO as determined from optical retardation and X-ray experiments. The symbols represent the columnar-to-isotropic phase transition temperatures T_h as determined from optical birefringence experiments. The solid diagonal line separating the supercooled confined liquid state and the confined columnar phase is a $1/d$ fit of T_h shown also in fig. 5.3. The insets represent sketches of the order in the single nanopores along with the resulting effective isotropy in the liquid and positive or negative optical birefringence in the liquid-crystalline state, i. e. spherical, prolate or oblate indicatrices, respectively.

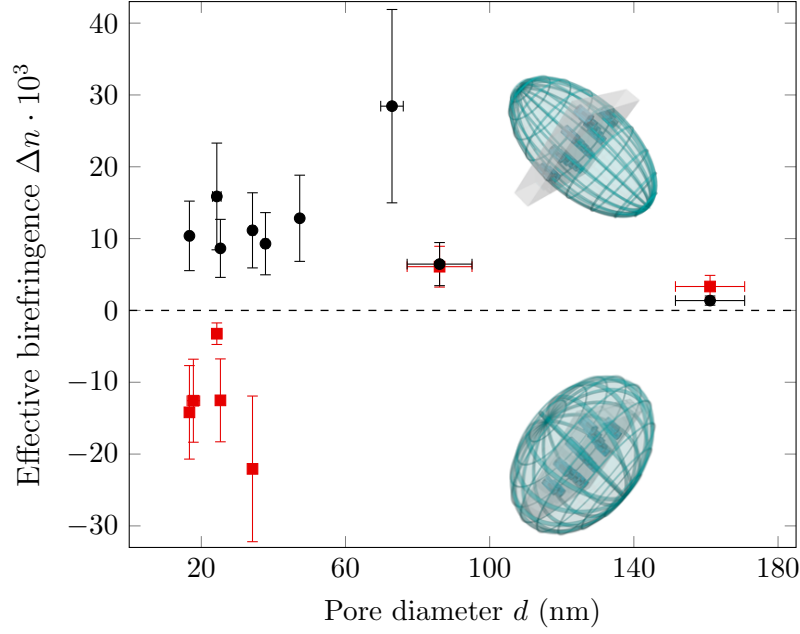


Figure 5.10.: Effective birefringence Δn of HAT6 filled AAO as a function of pore diameters for hydrophilic (black circles) and hydrophobic (red rectangles) nanopores in the liquid crystalline phase.

lines are the fits performed with the Gibbs Thompson equation. Figure 5.9(a) shows the formation of the logpile configuration and, with decreasing pore diameter, the transition in between the two dominant domains, $(100)_{\parallel}$ and $(100)_{\perp}$. Independent of pore size a positive birefringent material represented by a prolate indicatrix is realized. For hydrophobic pores with decreasing pore size fig. 5.9(b) shows the transition between $(100)_{\parallel}$ and $(100)_{\perp}$ circular concentric domains resulting solely in positive birefringent materials. Further decrease in pore diameter results in the axial configuration accompanied by a switch from positive to negative birefringent materials. The anisotropy of the later is represented by an oblate indicatrix.

As illustrated in the phase diagrams, by prolate and oblate optical indicatrices, the pore size and surface chemistry dependent self-assembly behavior results in tailorable optical anisotropy. The hydrophilic pores always exhibit a positive optical anisotropy resulting from the logpile configuration. For the hydrophobic pores the optical anisotropy at low temperature is negative for small pore diameter and positive for large pore diameters. Thus, the optical anisotropy can be switched between positive and negative, as collective molecular arrangement changes from circular concentric to axial. These structural transformations are absent in the bulk DLC and the manipulation of light takes place on the scale of the wavelength of visible light. Hence, this soft-hard hybrid material shows typical characteristics of a metamaterial [4].

A more quantitative analysis can be made by calculating the effective birefringence Δn of the resulting metamaterials as a function of pore surface grafting and, thus, molecular anchoring. Therefore, the retardation value in the columnar hexagonal phase, see fig. 5.1,

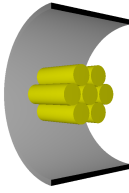
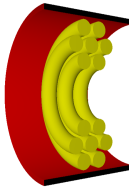
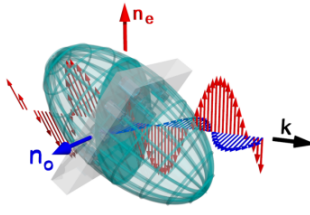
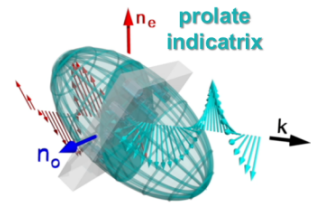
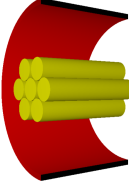
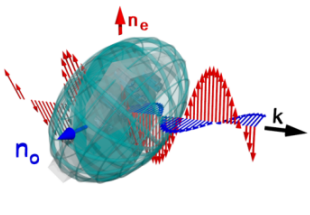
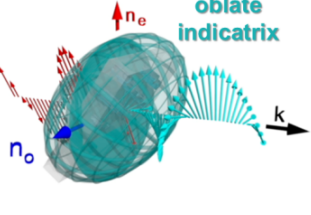
Self-assembly in single pore		Optical anisotropy of pore array	
Hydrophilic	Hydrophobic		
			
161 - 17 nm	> 73 nm	$\Delta n > 0$	
			
	< 73 nm	$\Delta n < 0$	

Table 5.4.: Self-assembly in a single nanopore and resulting optical anisotropy of pore array depending on the surface hydrophilicity and pore diameter. Positive birefringent materials yield left-handed elliptically light, while negative birefringent materials yield right-handed elliptically light after passing through the pore array.

will be used to calculate the pore diameter dependent effective birefringence $\Delta n(d)$.

Despite the fact that empty amorphous AAO is optical isotropic, the anisotropic collective arrangement of parallel cylindrical pores results in a small positive geometric birefringence [87, 99], see also fig. A.5 in appendix A. This form birefringence is on the order of $\Delta n \approx 0.02$ for the empty porous membranes. Upon filling the pores with an isotropic liquid this small form anisotropy is slightly reduced, because of the reduction in the refractive index difference between pore wall and pore filling.

The effective birefringence Δn for HAT6 filled AAO is plotted as a function of pore diameter in fig. 5.10. As expected the logpile configuration in the hydrophilic pore space results solely in positive birefringent properties. However, its strength increases with decreasing pore size up to values of $\Delta n \approx 0.015$. This optical effect can be directly correlated to the increased hexagonal order determined by X-ray diffraction, see fig. 5.6. In the hydrophobic case only samples with pure axial or circular concentric, hence, pure negative or positive optical anisotropy are considered. The strength of Δn in hydrophobic large pores basically equals that of the hydrophilic pores of same size. Upon transition to the pure axial configuration the birefringence switches to negative values. Its value is considerably larger than in the hydrophilic case.

All in all, by going to smaller pores and changing the surface chemistry to be more

hydrophobic, the optical anisotropy can be changed in controlled manner, i. e. adapted from positive to negative optical birefringence. Additionally, this optical anisotropy can be switched on or off as a function of temperature. Moreover, it is interesting to note that the circular concentric to axial transition results not only in a change of the optical anisotropy. For the used beam geometry and the observed retardations, the textures with collective circular concentric/logpile orientations yield left-handed elliptically polarized light while the axial state yields right-handed elliptically polarized light after passing through the pore array, respectively, see table 5.4.

6. Conclusion

The aim of this thesis was to investigate the influence of confinement on the nanoscale on the self-assembly behavior of a discotic liquid crystal (HAT6). Therefore, HAT6 was filled into mesoporous silica and meso- and macroporous anodized aluminum oxide by spontaneous imbibition. As a function of temperature, pore size and surface chemistry the liquid crystalline self-assembly in the cylindrical pores was probed. Orientational ordering, and thus optical properties, were measured using an optical polarimetry method, while the structural arrangements were analyzed by transmission X-ray diffraction experiments. Additionally, the results were analyzed regarding the potential to design a new soft-hard metamaterial with resulting effective optical properties.

By confining HAT6 in hydrophobic mesoporous silica a quantized phase transition was found. In combination with Monte Carlo simulations the experiments showed, that the stepwise transformation originates in the formation of circular concentric rings. This finding is reminiscent of the quantized nature of the isotropic-smectic transition reported for rod-like liquid crystals at planar interfaces [100–102]. However, in contrast to that, the quantization reported in this thesis is determined by the discreteness of the layers' excess bend deformation energies in comparison to the thermal energy. This phase transition quantization exemplifies in an impressive way how confinement can alter the physics of liquid crystals. Additionally, tracing back the layer formation solely to the bend elastic energy of the circular concentric discotic rings, the rarely measured bend elastic constant K_3 , giving a value on how easy the columns bend, was determined.

The same discotic liquid crystal was filled in meso- and macroporous anodized aluminum oxide. The self-assembly mechanism, in addition to effective metamaterial optical properties, was analyzed as a function of temperature, pore sizes and surface functionality. Independent of pore size, cylindrical hydrophilic pores lead solely to a logpile configuration in agreement with previous results [21, 24]. By varying the pore size two dominant hexagonal domains are realized, while a complete randomization of the hexagonal ordering is present in the smallest pore diameter investigated. These configurations solely result in a positive birefringent metamaterial. Its strength, as well as the hexagonal ordering, increases with decreasing confining space. This shows in a remarkable manner how confinement can induce stronger orientational and translational ordering.

By decreasing the size of hydrophobic pores again a crossover inbetween two dominant hexagonal domains, followed by an orientational transition from a circular concentric to

an axial configuration was found. The later has to the best of our knowledge never been achieved with confined HAT6 so far. However, prospective measurements suggest only a weak conductivity along the columnar axis. This could be increased by adding an electron donator as a dopant or employing DLCs with a larger aromatic core. Additionally, the reorientation process from circular concentric to axial is accompanied by a switch between optical positive and negative birefringence respectively allowing to adapt the polarization of light passing through the material in a controlled way. These findings, especially with regard to the temperature dependence and optical properties, go beyond, but also perfectly complement previous results of the same hybrid material system [25]. They also enqueue perfectly in results of versatile confined soft matter systems whose physics can still be described based on continuum, hence, effective medium theories [36–39].

Neither the phase transition quantization, nor the tailorable effective optical birefringence can be achieved within the bulk state. Additionally, all structural arrangements and reorientation processes described in this thesis take place on the nanoscale. Employing an effective medium model the effective metamaterial properties can be analyzed. Hence, combining mechanical solid membranes with a functional discotic liquid crystal enables the preparation of a new integrated material system with tunable photonic metamaterial properties. Its effective optical birefringence can be adapted in a versatile manner by a proper choice of temperature, size of confining space and pore surface chemistry. In particular, by varying the optical birefringence from positive to negative the polarization of light, traversing the newly designed metamaterial, can be switched between left-handed and right-handed elliptical.

From an application-oriented view this adjustability of optical properties by purely tuning collective molecular order and thus dielectric anisotropy along with the mechanical stability is particularly interesting to induce well-defined lateral phase shift gradients of electromagnetic waves in solid supports or surfaces [103–105]. In contrast to e.g. common retardation plates, which only allow a fixed phase shift between different polarization states of light, even so far impossible retardation values can be easily set by adjusting the systems temperature. Additionally, such phase gradients are at the core of transformative optical properties, such as negative refraction, optical cloaking, tuneable optical absorbers and metalenses capable of manipulating light by imparting local, space-variant phase changes on an incident electromagnetic wave [106].

In conclusion, this thesis shows that liquid-crystal-infused nanoporous solids allow for simple design of materials with adaptable multifunctionality especially with regard to newly designed photonic metamaterials.

Bibliography

- [1] Friedrich Reinitzer. „Beiträge zur Kenntniss des Cholesterins“. *Monatshefte für Chemie und verwandte Teile anderer Wissenschaften* 9 (1888). DOI: 10.1007/BF01516710.
- [2] Otto Lehmann. „Über fließende Krystalle.“ *Zeitschrift für physikalische Chemie* (1889). DOI: 10.1515/zpch-1889-0434.
- [3] Thomas Geelhaar et al. „125 Jahre Flüssigkristalle - die wissenschaftliche Revolution im Wohnzimmer“. *Angewandte Chemie* 125 (2013). DOI: 10.1002/ange.201301457.
- [4] Oleg D. Lavrentovich. „Liquid crystals, photonic crystals, metamaterials, and transformation optics“. *Proceedings of the National Academy of Sciences* 108 (2011). DOI: 10.1073/pnas.1102130108.
- [5] Muamer Kadic et al. „3D metamaterials“. *Nature Reviews Physics* (2019). DOI: 10.1038/s42254-018-0018-y.
- [6] Oleksandr Buchnev et al. „Electrically controlled nanostructured metasurface loaded with liquid crystal: Toward multifunctional photonic switch“. *Advanced Optical Materials* 3 (2015). DOI: 10.1002/adom.201400494.
- [7] Matthias Spengler et al. „Hydrogen-bonded liquid crystals in confined spaces-toward photonic hybrid materials“. *Advanced Functional Materials* (2018). DOI: 10.1002/adfm.201800207.
- [8] Tobias Wöhrle et al. „Discotic liquid crystals“. *Chemical Reviews* 116 (2016). DOI: 10.1021/acs.chemrev.5b00190.
- [9] Eva Kristina Fleischmann et al. „Liquid-crystalline ordering as a concept in materials science: From semiconductors to stimuli-responsive devices“. *Angewandte Chemie - International Edition* 52 (2013). DOI: 10.1002/anie.201300371.
- [10] Manish Kumar et al. „Liquid crystals in photovoltaics: A new generation of organic photovoltaics“. *Polymer Journal* 49 (2017). DOI: 10.1038/pj.2016.109.
- [11] Takashi Kato et al. „Transport of ions and electrons in nanostructured liquid crystals“. *Nature Reviews Materials* 2 (2017). DOI: 10.1038/natrevmats.2017.1.

- [12] Hari Krishna Bisoyi et al. „Stimuli directed alignment of self-organized one-dimensional semiconducting columnar liquid crystal nanostructures for organic electronics“. *Progress in Materials Science* (2019). DOI: 10.1016/j.pmatsci.2019.03.005.
- [13] Thomas Brunet et al. „Anchoring transition in confined discotic columnar liquid crystal films“. *Europhysics Letters* 93 (2011). DOI: 10.1209/0295-5075/93/16004.
- [14] Hatice Duran et al. „Arrays of aligned supramolecular wires by macroscopic orientation of columnar discotic mesophases“. *ACS Nano* 6 (2012). DOI: 10.1021/nn302937t.
- [15] Sylwia Całus et al. „Thermotropic interface and core relaxation dynamics of liquid crystals in silica glass nanochannels: A dielectric spectroscopy study“. *Physical Chemistry Chemical Physics* 17 (2015). DOI: 10.1039/c5cp03039k.
- [16] Seong Ho Ryu et al. „Liquid crystal phases in confined geometries“. *Liquid Crystals* 43 (2016). DOI: 10.1080/02678292.2016.1205674.
- [17] Mark Busch et al. „A ferroelectric liquid crystal confined in cylindrical nanopores: Reversible smectic layer buckling, enhanced light rotation and extremely fast electro-optically active Goldstone excitations“. *Nanoscale* 9 (2017). DOI: 10.1039/c7nr07273b.
- [18] G.P. Crawford et al. *Liquid crystals in complex geometries*. CRC Press, 1996.
- [19] Martin Steinhart et al. „Liquid crystalline nanowires in porous alumina: Geometric confinement versus influence of pore walls“. *Nano Letters* 5 (2005). DOI: 10.1021/nl0481728.
- [20] Andriy V. Kityk et al. „Thermotropic orientational order of discotic liquid crystals in nanochannels: An optical polarimetry study and a Landau-de Gennes analysis“. *Soft Matter* 10 (2014). DOI: 10.1039/c4sm00211c.
- [21] Sylwia Całus et al. „Molecular ordering of the discotic liquid crystal HAT6 confined in mesoporous solids“. *Microporous and Mesoporous Materials* 197 (2014). DOI: 10.1016/j.micromeso.2014.05.036.
- [22] Christina Krause et al. „Thermal properties and vibrational density of states of a nanoconfined discotic liquid crystal“. *Colloid and Polymer Science* 292 (2014). DOI: 10.1007/s00396-014-3247-3.
- [23] Sylwia Całus et al. „High-resolution dielectric study reveals pore-size-dependent orientational order of a discotic liquid crystal confined in tubular nanopores“. *Physical Review E - Statistical, Nonlinear, and Soft Matter Physics* 92 (2015). DOI: 10.1103/PhysRevE.92.012503.

-
- [24] Ruibin Zhang et al. „Columnar liquid crystals in cylindrical nanoconfinement“. *ACS Nano* 9 (2015).
- [25] Rui-bin Zhang et al. „Diverse configurations of columnar liquid crystals in cylindrical nano- and micropores“. *Soft Matter* 13 (2017). DOI: 10.1039/C7SM00620A.
- [26] Martin Bäker. *Funktionswerkstoffe*. Springer Vieweg, 2014.
- [27] P. G. de Gennes et al. *The physics of liquid crystals*. Oxford University Press, 1993.
- [28] Sandeep Kumar. *Chemistry of discotic liquid crystals*. CRC Press, 2011.
- [29] Satyendra Kumar. *Liquid crystals*. Cambridge University Press, 2001.
- [30] Lars Onsager. „The effects of shape on the interaction of colloidal particles“. *Annals of the New York Academy of Sciences* 51 (1949). DOI: 10.1111/j.1749-6632.1949.tb27296.x.
- [31] Wilhelm Maier et al. „Eine einfache molekular-statistische Theorie der nematischen kristallinflüssigen Phase. Teil II“. *Zeitschrift für Naturforschung A* 14 (1959). DOI: 10.1515/zna-1960-0401.
- [32] L. D. Landau et al. *Statistical physics*. Pergamon Press, 1959.
- [33] Pierre-Gilles de Gennes. „Short range order effects in the isotropic phase of nematics and cholesterics“. *Molecular Crystals and Liquid Crystals* 12 (1971). DOI: 10.1080/15421407108082773.
- [34] Masao Doi. *Soft matter physics*. Oxford University Press, 2013.
- [35] S. Chandrasekhar. *Liquid crystals*. Cambridge University Press, 1992.
- [36] Kurt Binder et al. „Confinement effects on phase behavior of soft matter systems“. *Soft Matter* 4 (2008). DOI: 10.1039/b802207k.
- [37] C. Alba-Simionesco et al. „Effects of confinement on freezing and melting“. *Journal of Physics Condensed Matter* 18 (2006). DOI: 10.1088/0953-8984/18/6/R01.
- [38] Patrick Huber. „Soft matter in hard confinement: Phase transition thermodynamics, structure, texture, diffusion and flow in nanoporous media“. *Journal of Physics Condensed Matter* 27 (2015). DOI: 10.1088/0953-8984/27/10/103102.
- [39] Kathrin Sentker et al. *Liquid crystals confined in nanoporous solids: From fundamentals to functionalities. Soft molecular matter under confinement: From planar interfaces to nanoporous media*. World Scientific, 2020.
- [40] Ping Sheng. „Phase transition in surface-aligned nematic films“. *Physical Review Letters* 37 (1976). DOI: 10.1103/PhysRevLett.37.1059.
- [41] A. Poniewierski et al. „Theory of the nematic-isotropic transition in a restricted geometry“. *Liquid Crystals* 2 (1987). DOI: 10.1080/02678298708086677.

- [42] Hiroshi Yokoyama. „Nematic-isotropic transition in bounded thin films“. *Journal of the Chemical Society, Faraday Transactions 2: Molecular and Chemical Physics* 84 (1988). DOI: 10.1039/F29888401023.
- [43] Zdravko Kutnjak et al. „Calorimetric study of octylcyanobiphenyl liquid crystal confined to a controlled-pore glass“. *Physical Review E - Statistical Physics, Plasmas, Fluids, and Related Interdisciplinary Topics* 68 (2003). DOI: 10.1103/PhysRevE.68.021705.
- [44] Zdravko Kutnjak et al. „Influence of finite size and wetting on nematic and smectic phase behavior of liquid crystal confined to controlled-pore matrices“. *Physical Review E - Statistical Physics, Plasmas, Fluids, and Related Interdisciplinary Topics* 70 (2004). DOI: 10.1103/PhysRevE.70.051703.
- [45] Andriy V. Kityk et al. „Continuous paranematic-to-nematic ordering transitions of liquid crystals in tubular silica nanochannels“. *Physical Review Letters* 101 (2008). DOI: 10.1103/PhysRevLett.101.187801.
- [46] Sylwia Calus et al. „Inhomogeneous relaxation dynamics and phase behaviour of a liquid crystal confined in a nanoporous solid“. *Soft Matter* 11 (2015). DOI: 10.1039/c5sm00108k.
- [47] C. W. Oseen. „The theory of liquid crystals“. *Transactions of the Faraday Society* 29 (1932).
- [48] F. C. Frank. „On the theory of liquid crystals“. *Discussions of the Faraday Society* 25 (1958).
- [49] Kathrin Sentker et al. „Quantized self-assembly of discotic rings in a liquid crystal confined in nanopores“. *Physical Review Letters* 120 (2018). DOI: 10.1103/PhysRevLett.120.067801.
- [50] Arne Wolf Zantop. „Computer simulations of discotic liquid crystals in nanoconfinement“. Bachelor thesis. Georg-August-Universität Göttingen, 2015.
- [51] R. Defay et al. *Surface tension and adsorption*. Longman, Green & Co LTD, 1966.
- [52] Hugo K. Christenson. „Confinement effects on freezing and melting“. *Journal of Physics-Condensed Matter* 13 (2001). DOI: 10.1088/0953-8984/13/11/201.
- [53] Wolfgang Nolting. *Grundkurs Theoretische Physik 4/2 Thermodynamic*. Springer Spektrum, 1997.
- [54] R. W. Batchelor et al. „The freezing point of adsorbed liquids“. *Transactions of the Faraday Society* 40 (1944). DOI: 10.1039/tf9444000300.
- [55] William Thomson. „On the equilibrium of vapour at a curved surface of liquid“. *Proceedings of the Royal Society of Edinburgh* 7 (1872). DOI: 10.1017/S0370164600041729.

-
- [56] J. Willard Gibbs. *The collected works of J. Willard Gibbs, volume I: thermodynamics*. Yale University Press, 1928.
- [57] Catheryn L. Jackson et al. „The melting behavior of organic materials confined in porous solids“. *The Journal of Chemical Physics* 93 (1990). DOI: 10.1063/1.459240.
- [58] Eugene Hecht. *Optics*. Addison Wesley, 2002.
- [59] Max Born et al. *Principle of optics*. Pergamon Press, 1959.
- [60] Bergmann L. et al. *Lehrbuch der Experimentalphysik Band 3 Optik*. Walter de Gruyter, 1955.
- [61] N. Boden et al. „The synthesis of triphenylene-based discotic mesogens new and improved routes“. *Liquid Crystals* 15 (1993). DOI: 10.1080/02678299308036504.
- [62] Christina Krause et al. „Vibrational density of states of triphenylene based discotic liquid crystals: Dependence on the length of the alkyl chain“. *Physical Chemistry Chemical Physics* 16 (2014). DOI: 10.1039/c3cp55303e.
- [63] Fokko M. Mulder et al. „Dynamics of a triphenylene discotic molecule, HAT6, in the columnar and isotropic liquid phases“. *Journal of the American Chemical Society* 125 (2003). DOI: 10.1021/ja029227f.
- [64] Xinliang Feng et al. „Towards high charge-carrier mobilities by rational design of the shape and periphery of discotics“. *Nature Materials* 8 (2009). DOI: 10.1038/nmat2427.
- [65] J. Rouquerolt et al. „Recommendations for the characterization of porous solids“. *Pure and Applied Chemistry* 66 (1994). DOI: doi:10.1351/pac199466081739.
- [66] Dennis R. Turner. „Electropolishing silicon in hydrofluoric acid solutions“. *Journal of The Electrochemical Society* 105 (1958). DOI: 10.1149/1.2428873.
- [67] V. Lehmann et al. „Formation mechanism and properties of electrochemically etched trenches in n-type silicon“. *Journal of The Electrochemical Society* 137 (1990). DOI: 10.1149/1.2086525.
- [68] V. Lehmann et al. „Porous silicon formation: A quantum wire effect“. *Applied Physics Letters* 58 (1991). DOI: 10.1063/1.104512.
- [69] Volker Lehmann. *Electrochemistry of silicon*. Wiley-VCH Verlag, 2002.
- [70] Mark Busch. „Optische Untersuchungen zum Kapillarsteigen von Flüssigkeiten in mesoporösen Festkörpern“. Diploma thesis. Universität des Saarlandes, 2012.
- [71] Michael J. Sailor. *Porous silicon in practice: preparation, characterization and applications*. Wiley-VCH Verlag, 2012.

- [72] Milton W. Cole et al. „Excitation spectrum and thermodynamic properties of liquid films in cylindrical pores“. *Physical Review Letters* 32 (1974). DOI: 10.1103/PhysRevLett.32.985.
- [73] Elliott P. Barrett et al. „The determination of pore volume and area distributions in porous substances. I. Computations from nitrogen isotherms“. *Journal of the American Chemical Society* 73 (1951). DOI: 10.1021/ja01145a126.
- [74] Quantachrome Instruments. „auto sorb iQ and ASiQwin GAS SORPTION SYSTEM“ (2013).
- [75] Simon Alexander Grüner. „Rheology and dynamics of simple and complex liquids in mesoporous matrices“. PhD thesis. Universität des Saarlandes, 2010.
- [76] G.E. Thompson et al. „Nucleation and growth of porous anodic films on aluminium“. *Nature* 272 (1978). DOI: 10.1038/272433a0.
- [77] Hideki Masuda et al. „Ordered metal nanohole arrays made by a two-step replication of honeycomb structures of anodic alumina“. *Science* 268 (1995).
- [78] O. Jessensky et al. „Self-organized formation of hexagonal nanopore arrays in anodic alumina“. *Applied Physics Letters* 72 (1989). DOI: 10.1088/1009-1963/10/3/309.
- [79] A. P. Li et al. „Hexagonal pore arrays with a 50-420 nm interpore distance formed by self-organization in anodic alumina“. *Journal of Applied Physics* 84 (1998). DOI: 10.1063/1.368911.
- [80] Kornelius Nielsch et al. „Self-ordering regimes of porous alumina: The 10 porosity rule“. *Nano Letters* 2 (2002). DOI: 10.1021/nl025537k.
- [81] H.-G. Steinrück et al. „Pseudorotational epitaxy of self-assembled octadecyltrichlorosilane monolayers on sapphire (0001)“. *Physical Review Letters* 113 (2014). DOI: 10.1103/PhysRevLett.113.156101.
- [82] Hagen Klauk et al. „Ultralow-power organic complementary circuits“. *Nature* 445 (2007). DOI: 10.1038/nature05533.
- [83] Artoem Khassanov et al. „Structural investigations of self-assembled monolayers for organic electronics: Results from X-ray reflectivity“. *Accounts of Chemical Research* 48 (2015). DOI: 10.1021/acs.accounts.5b00022.
- [84] Christos Grigoriadis et al. „Suppression of phase transitions in a confined rodlike liquid crystal“. *ACS Nano* 5 (2011).
- [85] Christina Krause. „Structure and dynamics of discotic liquid crystals in the bulk and in the confined state“. PhD thesis. Technische Universität Berlin, 2014.

-
- [86] Kathrin Sentker et al. „Self-Assembly of liquid crystals in nanoporous solids for adaptive photonic metamaterials“. *Nanoscale* 11 (2019). DOI: 10.1039/c9nr07143a.
- [87] Andriy V. Kityk et al. „Liquid n-hexane condensed in silica nanochannels: A combined optical birefringence and vapor sorption isotherm study“. *Physical Review B - Condensed Matter and Materials Physics* 80 (2009). DOI: 10.1103/PhysRevB.80.035421.
- [88] John Schellman et al. „Optical spectroscopy of oriented molecules“. *Chemical Reviews* 87 (1987). DOI: 10.1021/cr00082a004.
- [89] M. Berek. „Zur Messung der Doppelbrechung hauptsächlich mit Hilfe des Polarisationsmikroskops“. *Centr. Mineral. Geol* (1913).
- [90] D. A. G. Bruggeman. „Berechnung verschiedener physikalischer Konstanten von heterogenen Substanzen“. *Annalen der Physik* 421 (1937). DOI: 10.1002/andp.19374210205.
- [91] Wim H. de Jeu. *Basic X-ray scattering for soft matter*. Oxford University Press, 2016.
- [92] O. H. Seeck et al. „The high-resolution diffraction beamline P08 at PETRA III“. *Journal of Synchrotron Radiation* 19 (2012). DOI: 10.1107/S0909049511047236.
- [93] Ruibin Zhang et al. „Honeycombs in honeycombs: Complex liquid crystal alumina composite mesostructures“. *ACS Nano* 8 (2014). DOI: 10.1021/nn406368e.
- [94] Leandro N. Acquaroli et al. „Capillary filling in nanostructured porous silicon“. *Langmuir* 27 (2011). DOI: 10.1021/la104502u.
- [95] P. Huber et al. „Adsorption-desorption isotherms and X-ray diffraction of ar condensed into a porous glass matrix“. *Physical Review B - Condensed Matter and Materials Physics* 60 (1999). DOI: 10.1103/PhysRevB.60.12657.
- [96] L. Sallen et al. „Surface tension and elasticity of hexagonal columnar mesophases“. *Journal de Physique II France* 5 (1995).
- [97] Arda Yildirim et al. „Collective orientational order and phase behavior of a discotic liquid crystal under nanoscale confinement“. *Nanoscale Advances* 1 (2019). DOI: 10.1039/C8NA00308D.
- [98] Mahdy M. Elmahdy et al. „Self-assembly, molecular dynamics, and kinetics of structure formation in dipole-functionalized discotic liquid crystals“. *Journal of the American Chemical Society* 130 (2008). DOI: 10.1021/ja7113618.
- [99] Mitsunori Saito et al. „Anisotropic optical loss and birefringence of anodized alumina film“. *Journal of the Optical Society of America A* 6 (1989). DOI: 10.1364/JOSAA.6.001895.

- [100] B. M. Ocko et al. „Quantized layer growth at liquid-crystal surfaces“. *Physical Review Letters* 57 (1986). DOI: 10.1103/PhysRevLett.57.94.
- [101] Jonathan V. Selinger et al. „Density-functional theory of nematic and smectic A order near surfaces“. *Physical Review A* 37 (1988).
- [102] B. M. Ocko. „Smectic-layer growth at solid interfaces“. *Physical Review Letters* 64 (1990). DOI: 10.1103/PhysRevLett.64.2160.
- [103] Nanfang Yu et al. „Light propagation with phase discontinuities: Generalized laws of reflection and refraction“. *Science* 334 (2011). DOI: 10.1126/science.1210713.
- [104] J. B. Pendry et al. „Transformation optics and subwavelength control of light“. *Science* 337 (2012). DOI: 10.1126/science.1220600.
- [105] Zhanni Wu et al. „Tunable metasurfaces: A polarization rotator design“. *Physical Review X* 9 (2019). DOI: 10.1103/PhysRevX.9.011036.
- [106] Dianmin Lin et al. „Dielectric gradient metasurface optical elements“. *Science* 345 (2014). DOI: 10.1126/science.1253213.

A. Appendix

A.1. Complementary information

Confining hosts

Producer	Type	d (nm)	P (%)	Electrolyte
TUHH	pSiO ₂	15.6 ± 1.9	44 ± 0.1	HF
SM	AAO	16.7 ± 0.6	16 ± 1	H ₂ SO ₄
TUHH	pSiO ₂	17.4 ± 0.3	50 ± 1.9	HF
IR	AAO	17.8 ± 1.8	19.4 ± 1.6	H ₂ SO ₄
OS	”	24.3 ± 1.2	17.9 ± 0	”
SM	”	25.3 ± 0.2	28.8 ± 1	”
SM	”	34.2 ± 0.2	44.0 ± 0	”
SM	”	37.8 ± 0.7	15.8 ± 0.7	C ₂ H ₂ O ₄
SM	”	47.3 ± 0.2	21.5 ± 0	”
SM	”	73 ± 3	36.5 ± 1.6	”
IR	”	86 ± 9	7.6 ± 0.6	”
SM	”	161 ± 10	13.8 ± 1.6	H ₃ PO ₄

Table A.1.: Pore diameter and porosities of all meso- and macroporous membranes as determined by N₂ sorption isotherms. Indicated are the electrolytes used during the etching procedure. The membranes not fabricated at TUHH are purchased from SmartMembranes GmbH (SM), InRedox LLC (IR) and provided by the research group of M. Steinhart at University of Osnabrück (OS).

AAO isotherms

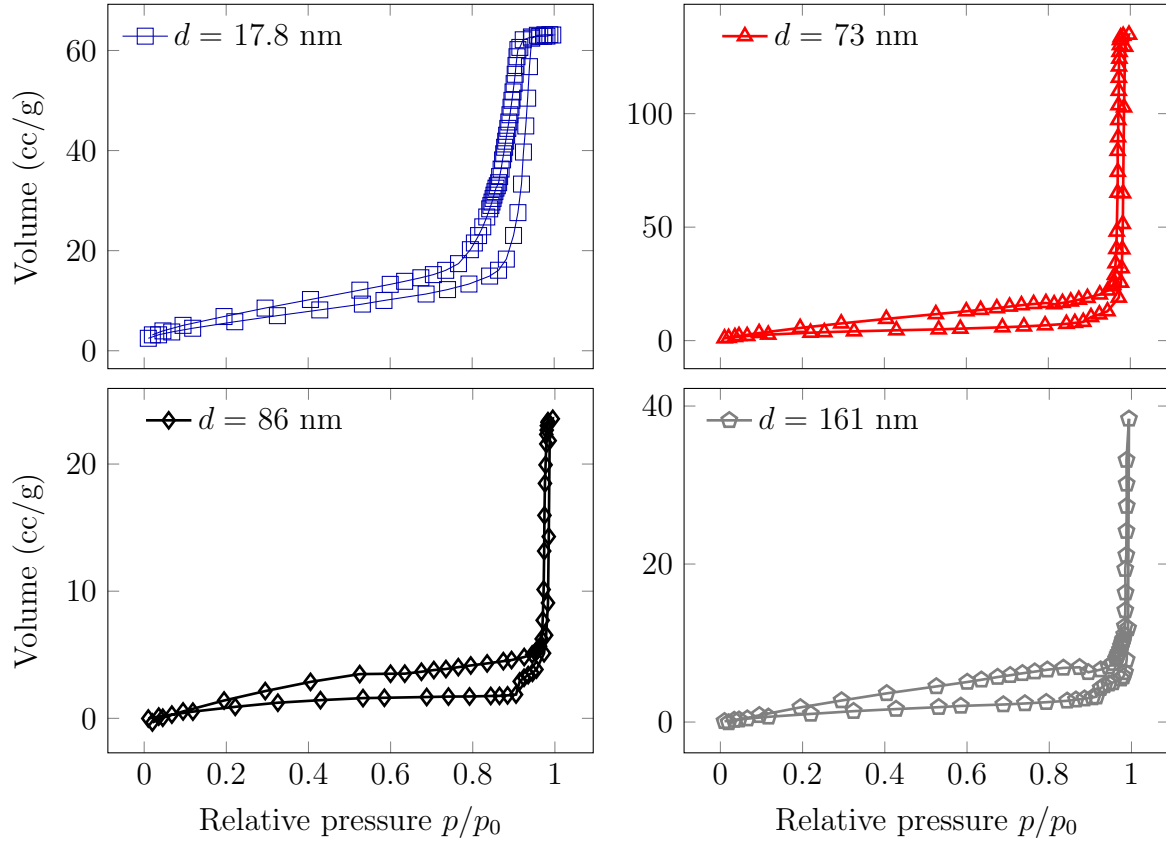


Figure A.1.: Volumetric nitrogen sorption isotherm of AAO showing the relative filling degree as a function of the relative pressure p/p_0 corresponding to the pore size distributions shown in fig. 3.4.

Copper temperature cell

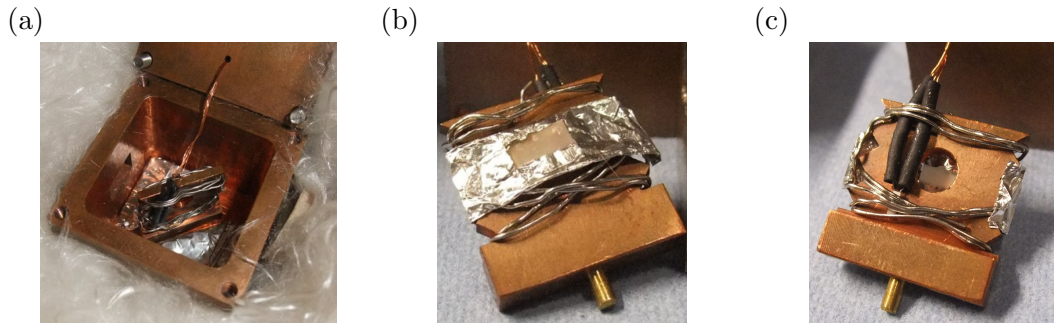


Figure A.2.: (a) Custom-build copper temperature cell inside insulation wool. The angle between laser beam and long pore axis is approx. $40^\circ \pm 5^\circ$. (b,c) Copper sample holder with PT-100 temperature sensor connected to a LakeShore temperature controller. Temperature from room temperature up to approx. 100°C are possible. The sample is wrapped in aluminum foil for good thermal contact and fixed to the holder.

Calibration optical birefringence

Positive			Negative		
1st harmonic	2nd harmonic	$R(T)$	1st harmonic	2nd harmonic	$R(T)$
90	90	\uparrow	90	90	\downarrow
90	-90	\downarrow	90	-90	\uparrow
-90	90	\downarrow	-90	90	\uparrow
-90	-90	\uparrow	-90	-90	\downarrow

Table A.2.: Reference measurement on a known positive and negative birefringent sample. The sign of the phases of the 1st and 2nd harmonic phase in combination with the temperature curve of the optical retardation $R(T)$ indicate the sign of the measured optical birefringence of a sample.

X-ray diffraction experiments

Light source	Beamline	Detector	Beamsize $V \times H$ (μm^2)	Wavelength λ (\AA)	q -range (\AA^{-1})
PETRA III	P08	Perkin Elmer	30×100	0.496	0.2 - 2.8
		XRD1621		0.687	0.1 - 2.0
ESRF	ID31	Pilatus3 X 2M	100×100	0.177	0.2 - 2.1
NSLS II	CMS	Pilatus3 X 2M	200×200	0.729	0.1 - 0.5

Table A.3.: Experimental details of the transmission X-ray experiments performed at PETRA III at Deutsches Elektronen-Synchrotron (DESY), the European Synchrotron Radiation Facility (ESRF) and the National Synchrotron Light Source (NSLS II).

Molecular orientation as a function of filling time

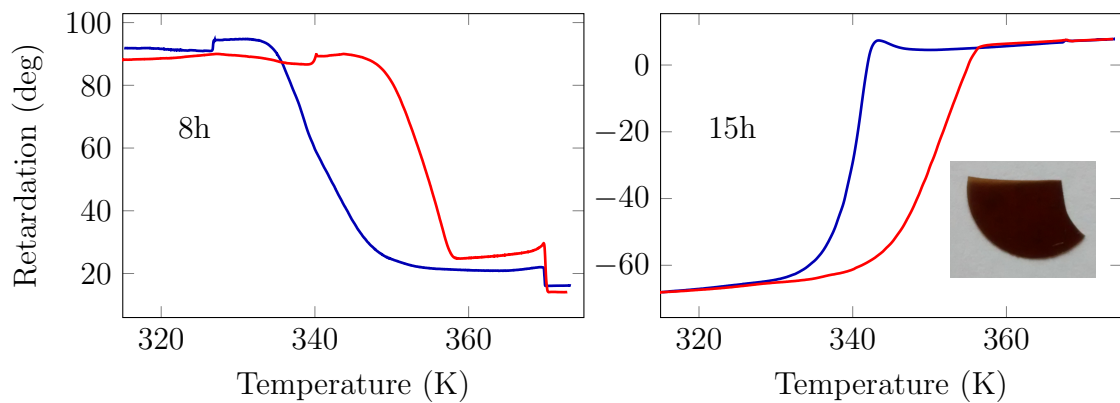


Figure A.3.: Temperature dependent optical retardation for HAT6 in AAO with $d = 16.7$ nm. Inbetween 8 hours and 15 hours filling time at 200°C the molecular orientation switches from logpile to axial. Additionally, the AAO membrane becomes brownish, see photograph.

Conductive AFM measurements

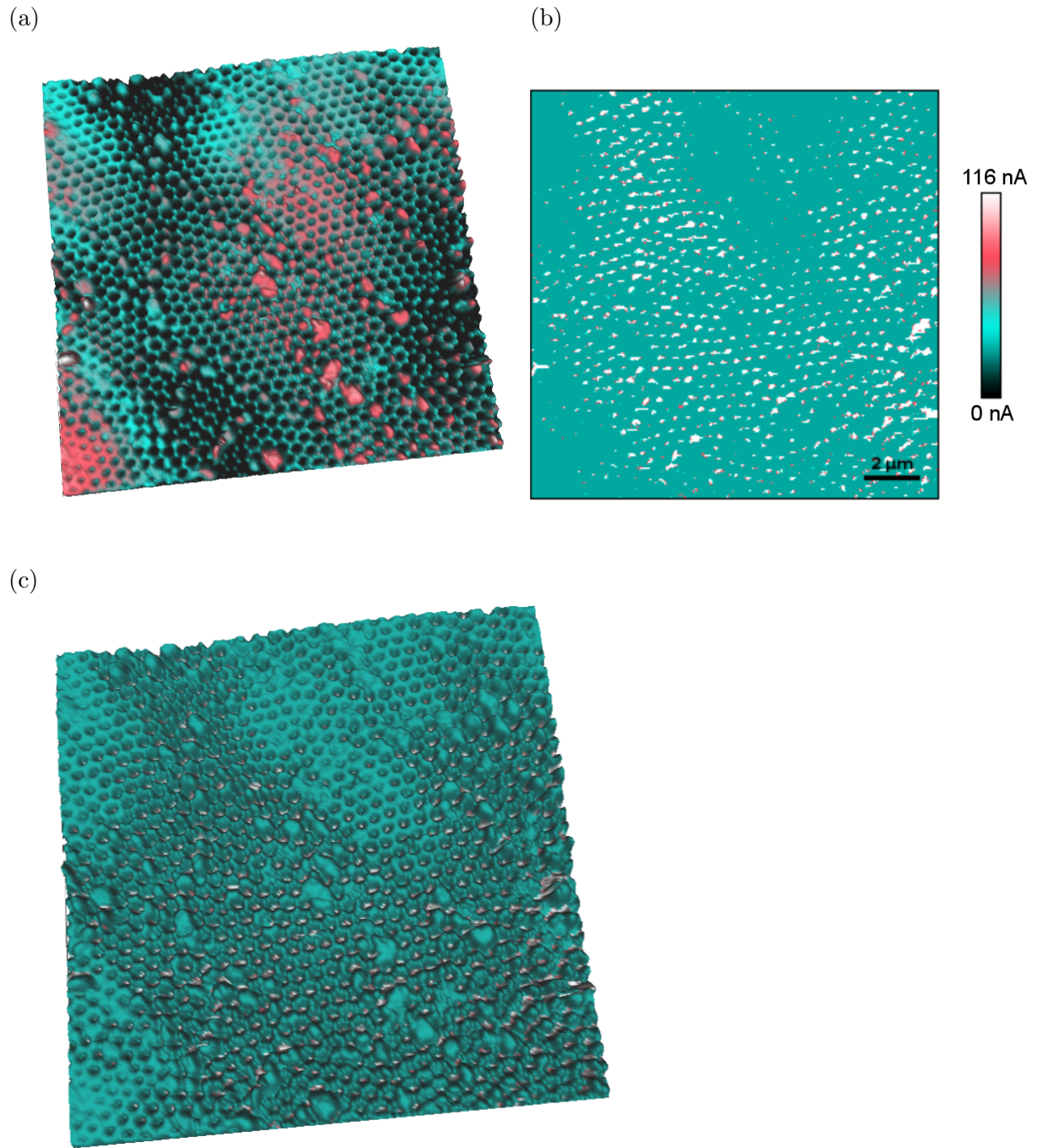


Figure A.4.: Atomic force microscopy images at room temperature of an HAT6 filled hydrophobic AAO sample with $d = 161$ nm. By using a conductive tip, sputtering both sample sides with a thin gold layer and applying a voltage the current along the nanopores can be detected. (a) Height profile ($15 \mu\text{m} \times 15 \mu\text{m}$), (b) conductive profile at 4V and (c) superposition of both. The hexagonal AAO structure shows a slightly increased current inside the pores filled with HAT6. Measurements were performed with the AFM Nanowizard 4 (JPK/Bruker) by Stella Gries (Master Student).

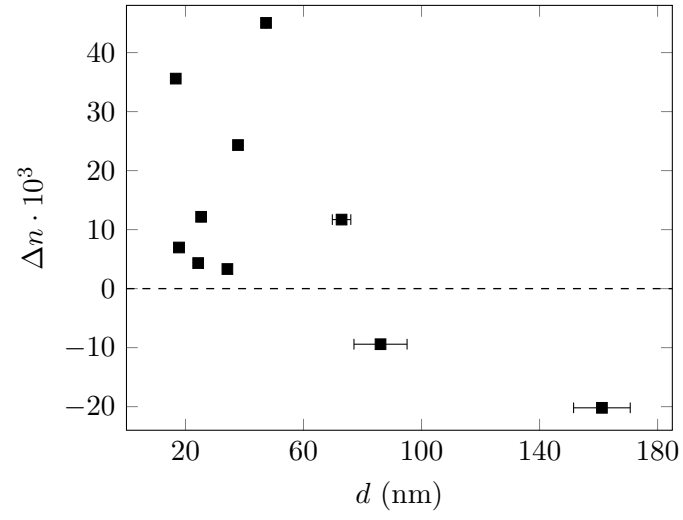
Form birefringence of empty AAO

Figure A.5.: Effective birefringence of empty anodic aluminum oxide as a function of pore diameter.

A.2. LabView programm

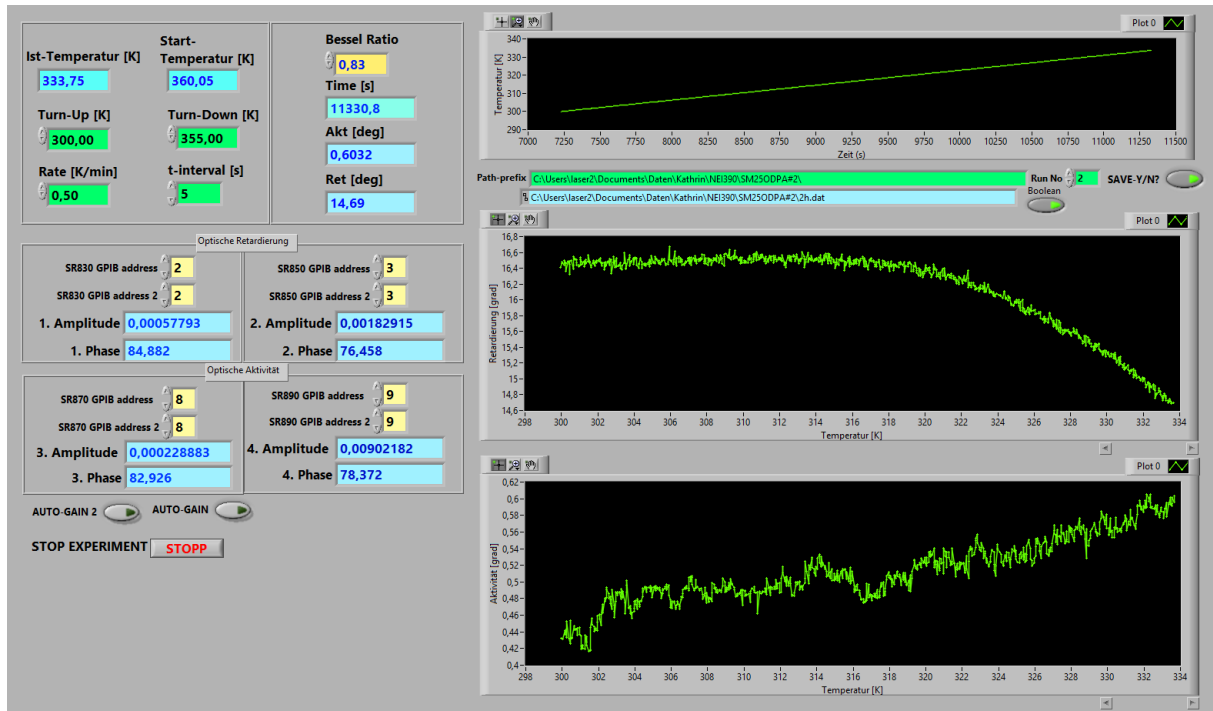


Figure A.6.: LabView program frontpanel.

To automatically address the measuring instruments shown in fig. 3.8 an already existing LabView program is extended to simultaneously measure the optical retardation and optical activity. In addition, the temperature control for the THS600 heating chamber is implemented. All hardware components are connected to the analysis computer via a GPIB-controller. Only the THS600 heating chamber is connected via a COM port. The programmed VI (Virtual Instrument) contains to programming levels: front panel shown in fig. A.6 and block diagram, parts are shown in fig. A.7 and A.8. The highlighted green boxes Turn-Up [K], Turn-Down [K], Rate [K/min], t-Interval [s], Path-prefix and Run-No are chosen by the user prior to every measurement. Turn-Up [K] and Turn-Down [K] indicate the temperatures inbetween which the measurement is performed, while Rate [K/min] indicates the heating/cooling rate. The Path-prefix gives the name of the data file indexed with the number Run-No. The yellow highlighted boxes give the GPIB addresses for every Lock-in as well as the Bessel ratio needed to calculated the optical retardation, see eq. 3.10 and optical activity. The blue highlighted boxes give the parameters that are read from the measurement instruments continuously. Hence, except the Start-Temperature [K], they change permanently depending on the t-Interval [s]. Additionally, three graphs are shown. The course of the temperature over time as well as the temperature dependent optical retardation and optical activity.

Is the program started initially the input parameters necessary to enable the communication between computer and hardware are set for the temperature controller of the THS600

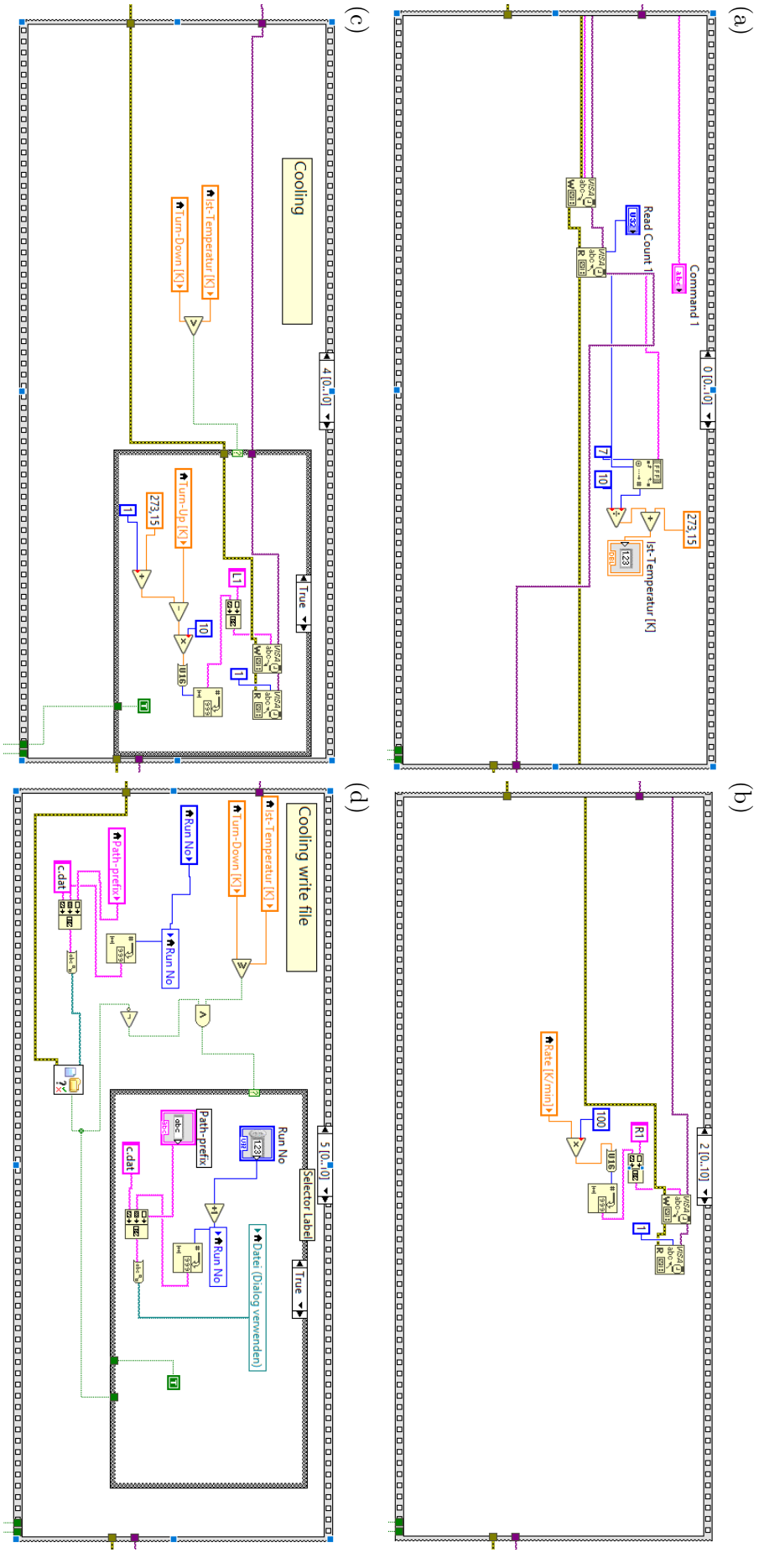


Figure A.8.: Temperature control for the THS600 heating chamber inside loop (part 2). (a) The current temperature is read. (b) Heating/cooling rate is sent to temperature controller. (c) If the current temperature is above the Turn-Down temperature the new target temperature is the Turn-Up temperature. (d) Additionally, if it does not already exist, a new cooling file including the Path-Prefix and run number is generated. All the data down to the Turn-Up temperature is written in this file. The VIs (c,d) equally exist for the heating run.

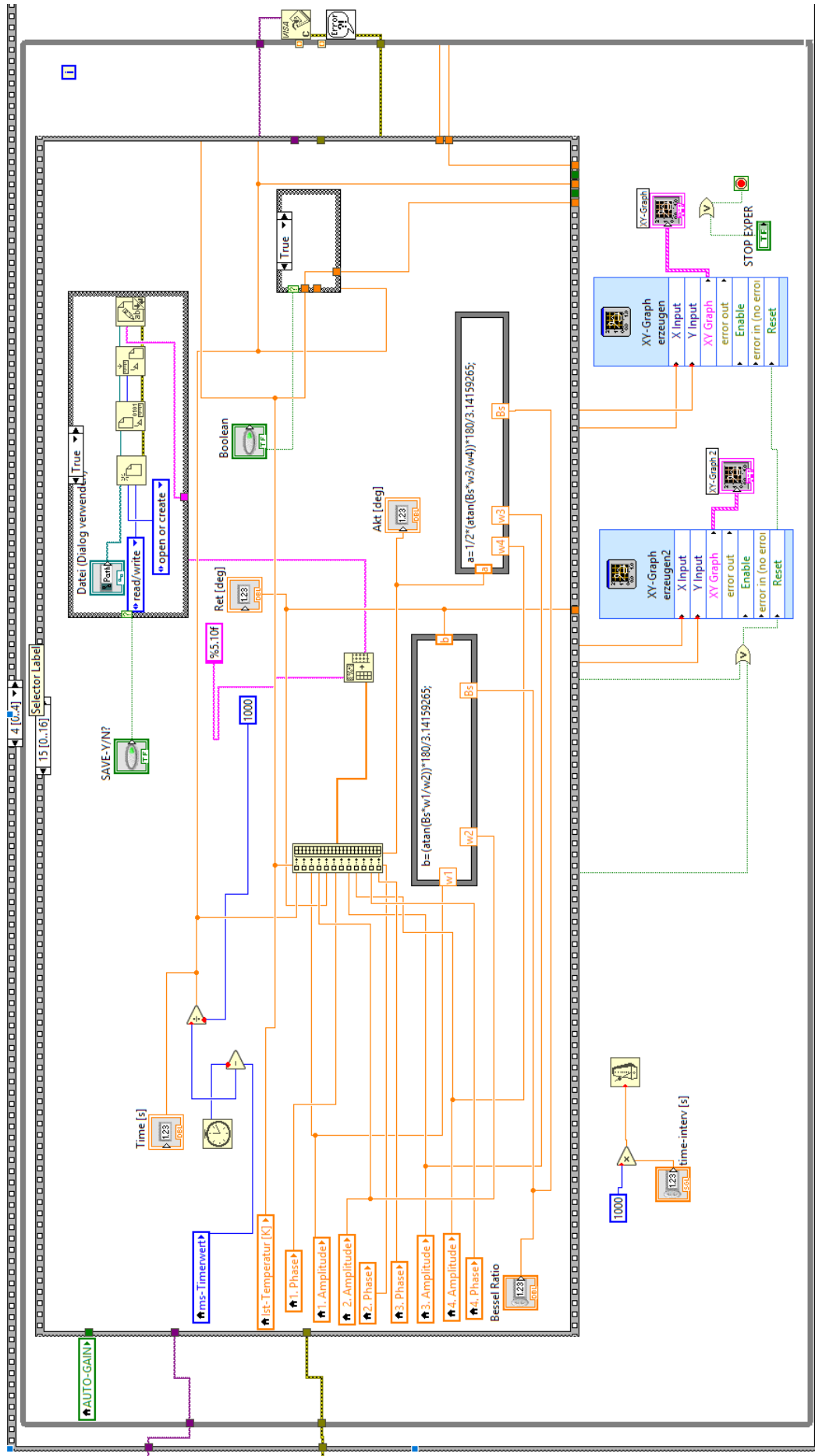


Figure A.9.: Assembling of all measured parameters and calculation of the optical retardation and activity. The data is saved and the graphs shown in the front panel are generated.

heating chamber, see fig. A.7(a), and Lock-Ins (VI not shown). In addition, a "0" file is created. Until either the Turn-Up [K] or Turn-Down [K] temperature is reached for the first time all measurement parameters are saved into this file. In the next step the initial Start-Temperature [K] is read, see fig. A.7(a). Is it inbetween Turn-Up [K] or Turn-Down [K] the controller heads up the chamber to Turn-Down [K], see fig. A.7(b), with a given rate, see fig. A.7(c).

As soon as the Turn-Down [K] temperature is reached for the first time a while loop starts. This loop is executed successively depending on the t-Interval [s] until it is stopped. At first, the current temperature is read, see fig. A.8(a), and the heating/cooling rate is set, see fig. A.8(b). As soon as the temperature reaches either Turn-Up [K] or Turn-Down [K] a new file with suffix "h" or "c" is generated and a new cooling/heating run starts, see fig. A.8(c,d). Then the 1. and 2. harmonic from the four Lock-Ins are read (VI not shown). These values are then used to calculate the optical retardation and activity, see fig. A.9. All measured parameters are then put together in one file and plotted in the front panel.

A.3. Berek's equation

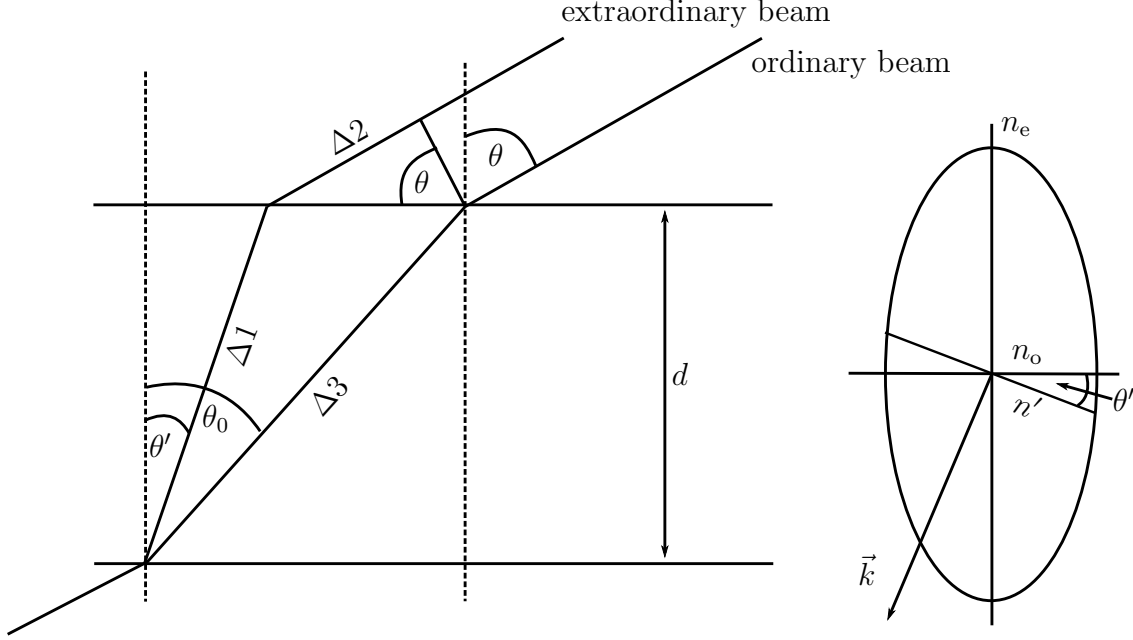


Figure A.10.: (Left) Illustration of optical pathways of ordinary and extraordinary beam inside sample with thickness d and incident angle θ of beam with respect to sample surface. This tilted sample geometry is described in section 3.2.2. (Right) Optical indicatrix for tilted sample geometry.

The incident angle θ is related to θ_0 and θ' as well as to the refractive indices n_o and n' by

$$\frac{\sin(\theta_0)}{\sin(\theta)} = \frac{1}{n_o} \quad \frac{\sin(\theta')}{\sin(\theta)} = \frac{1}{n'}. \quad (\text{A.1})$$

Considering the indicatrix shown in fig. A.10 n' is given by

$$\begin{aligned} \frac{(n' \cos(\theta'))^2}{n_o^2} + \frac{(n' \sin(\theta'))^2}{n_e^2} &= 1 \\ \Leftrightarrow \frac{(n' \sqrt{1 - \sin^2(\theta')})^2}{n_o^2} + \frac{\sin^2(\theta)}{n_e^2} &= 1 \\ \Leftrightarrow n'^2 n_e^2 - n_e^2 \sin^2(\theta) + n_o \sin^2(\theta) &= n_o^2 n_e^2 \\ \Leftrightarrow \sin^2(\theta) - \frac{n_o^2}{n_e^2} \sin^2(\theta) + n_o^2 &= n'^2. \end{aligned} \quad (\text{A.2})$$

The optical retardation R can be calculated by

$$R = \Delta 1 + \Delta 2 - \Delta 3 \quad (\text{A.3})$$

with optical paths $\Delta 1$, $\Delta 2$ and $\Delta 3$ given by

$$\begin{aligned}
 \Delta 1 &= \frac{dn'}{\cos(\theta')} = \frac{dn'}{\sqrt{1 - \sin^2(\theta')}} = \frac{dn'^2}{\sqrt{n'^2 - n'^2 \sin^2(\theta')}} = \frac{dn'^2}{\sqrt{n'^2 - \sin^2(\theta)}} \\
 &= d \cdot \frac{\sin^2(\theta) - \frac{n_o^2}{n_e^2} \sin^2(\theta) + n_o^2}{\sqrt{\sin^2(\theta) - \frac{n_o^2}{n_e^2} \sin^2(\theta) + n_o^2 - \sin^2(\theta)}} \\
 &= d \cdot \frac{\sin^2(\theta) - \frac{n_o^2}{n_e^2} \sin^2(\theta) + n_o^2}{n_o^2 \sqrt{1 - \frac{\sin^2(\theta)}{n_e^2}}} \\
 &= dn_o \cdot \frac{\frac{\sin^2(\theta)}{n_o^2} - \frac{\sin^2(\theta)}{n_e^2} + 1}{\sqrt{1 - \frac{\sin^2(\theta)}{n_e^2}}}, \tag{A.4}
 \end{aligned}$$

$$\begin{aligned}
 \Delta 2 &= (d \tan \theta_o - d \tan \theta') \sin(\theta) = d \cdot \left(\frac{\sin(\theta_o)}{\sqrt{1 - \sin^2(\theta)_o}} - \frac{\sin(\theta')}{\sqrt{1 - \sin^2(\theta')}} \right) \sin(\theta) \\
 &= d \left(\frac{\sin^2(\theta)}{n_o \sqrt{1 - \sin^2(\theta)_o}} - \frac{\sin^2(\theta)}{n' \sqrt{1 - \sin^2(\theta')}} \right) \\
 &= d \left(\frac{\sin^2(\theta)}{\sqrt{n_o^2 - \sin^2(\theta)}} - \frac{\sin^2(\theta)}{\sqrt{n'^2 - \sin^2(\theta)}} \right) \\
 &= dn_o \left(\frac{\sin^2(\theta)}{n_o^2 \sqrt{1 - \frac{\sin^2(\theta)}{n_o^2}}} - \frac{\sin^2(\theta)}{n_o^2 \sqrt{1 - \frac{\sin^2(\theta)}{n_e^2}}} \right) \\
 &= dn_o \left(\frac{\frac{\sin^2(\theta)}{n_o^2}}{\sqrt{1 - \frac{\sin^2(\theta)}{n_o^2}}} - \frac{\frac{\sin^2(\theta)}{n_o^2}}{\sqrt{1 - \frac{\sin^2(\theta)}{n_e^2}}} \right), \tag{A.5}
 \end{aligned}$$

and

$$\Delta 3 = \frac{dn_o}{\cos(\theta_o)} = \frac{dn_o}{\sqrt{1 - \sin^2(\theta_o)}} = dn_o \frac{n_o}{n_o \sqrt{1 - \sin^2(\theta_o)}}$$

$$\begin{aligned}
&= dn_o \frac{n_o}{\sqrt{n_o^2 - \sin^2(\theta)}} = dn_o \frac{1}{\sqrt{1 - \frac{\sin^2(\theta)}{n_o^2}}} \\
&= dn_o \frac{1}{\sqrt{1 - \frac{\sin^2(\theta)}{n_o^2}}}.
\end{aligned} \tag{A.6}$$

Combining eqs. A.4, A.5 and A.6 with eq. A.3 gives the optical retardation R in units of length

$$\begin{aligned}
R &= dn_o \left(\frac{1 - \frac{\sin^2(\theta)}{n_e^2}}{\sqrt{1 - \frac{\sin^2(\theta)}{n_e^2}}} - \frac{1 - \frac{\sin^2(\theta)}{n_o^2}}{\sqrt{1 - \frac{\sin^2(\theta)}{n_o^2}}} \right) \\
&= dn_o \left(\sqrt{1 - \frac{\sin^2(\theta)}{n_e^2}} - \sqrt{1 - \frac{\sin^2(\theta)}{n_o^2}} \right)
\end{aligned} \tag{A.7}$$

or in radians

$$R = \frac{2\pi dn_o}{\lambda} \left(\sqrt{1 - \frac{\sin^2(\theta)}{n_e^2}} - \sqrt{1 - \frac{\sin^2(\theta)}{n_o^2}} \right). \tag{A.8}$$

Using the definitions

$$n_o = \bar{n} - \frac{2\Delta n}{3} \quad n_e = \bar{n} + \frac{\Delta n}{3} \quad \bar{n} = \frac{2n_o + n_e}{3} \tag{A.9}$$

eq. A.8 yields eq. 3.11.

Publications and conferences

List of publications

- K. Sentker, A. Zantop, M. Lippmann, T. Hofmann, O. H. Seeck, A. V. Kityk, A. Yildirim, A. Schönhals, M. G. Mazza, and P. Huber, "Quantized self-assembly of discotic rings in a liquid crystal confined in nanopores", *Physical Review Letters* 120, 067801 (2018).
- K. Sentker and P. Huber, "Discrete supermolecular ring assembly: From nanoscale physics to metamaterials science", *Photon Science* 2018. Highlights and Annual Report. Deutsches Elektron-Synchrotron (2018).
- A. Yildirim, K. Sentker, G. J. Smales, B. R. Pauw, P. Huber and A. Schönhals, "Collective orientational order and phase behavior of a discotic liquid crystal under nanoscale confinement", *Nanoscale Advances* 1, 1104-1116 (2019).
- K. Sentker, M. Busch, A. V. Kityk and P. Huber, "Liquid crystals confined in nanoporous solids: From fundamentals to functionalities" in "Soft Matter and Biomaterials on the Nanoscale. Vol 1: Soft molecular matter under confinement: From planar interfaces to nanoporous media", *World Scientific Series in Nanoscience and Nanotechnology*, 20 (2020).
- K. Sentker, A. Yildirim, M. Lippmann, F. Bertram, T. Hofmann, O. H. Seeck, A. V. Kityk, A. Yildirim, A. Schönhals, and P. Huber, "Self-assembly of liquid crystals in nanoporous solids for adaptive photonic metamaterials", *Nanoscale*, 11, 23304-23317 (2019).

Conference contributions

Invited talks

- Condensed Matter Physics and Chemistry (CMPC) Workshop on “Nanoscale Materials - Structure and Properties”, Hamburg 02.2019
K. Sentker, A. Yildirim, M. Lippmann, A. Zantop, T. Hofmann, O. Seeck, A. Kityk, M. Mazza, A. Schönhals, P. Huber - ”Controlling optical properties and molecular self-assembly of a discotic liquid crystal in nanoconfinement”
- Gemeinsames Kolloquium – Institut für Organische Chemie und Institut für Physikalische Chemie, Universität Stuttgart 03.2016
K. Sentker, A. Yildirim, K. Knopp, A. Schönhals, P. Huber - ”Diskotische Flüssigkristalle in nanoporösen Festkörpern“

Contributed talks

- CRYSPOM VI - Crystallization in porous media, Hamburg 09.2018
DPG Frühjahrstagung, Berlin 03.2018
GLCC - German Liquid Crystal Conference, Luxemburg 03.2018
K. Sentker, A. Yildirim, M. Lippmann, A. Zantop, T. Hofmann, O. Seeck, A. Kityk, M. Mazza, A. Schönhals, P. Huber - ”Self-Assembly of Discotic Rings and Nanowires in a Liquid Crystal Confined in Nanopores”
- Interpore, Rotterdam 05.2017
K. Sentker, A. Yildirim, A. Schönhals, P. Huber - “Molecular orientation of a discotic liquid crystal in nanoporous solids”
- DPG Physikerinnentagung, Hamburg 11.2016
K. Sentker, A. Yildirim, A. Schönhals, P. Huber - ”Discotic Liquid Crystals in Nanoporous Solids“

Poster contributions

- DESY Photon Science Users‘ Meeting, Hamburg 01.2019
DESY Photon Science Users‘ Meeting, Hamburg 01.2018
PETRA IV Workshop, Hamburg 10.2017
10th Liquid Matter Conference, Ljubljana 07.2017
K. Sentker, A. Yildirim, A. Zantop, M. Lippmann, T. Hofmann, O. Seeck, A. Kityk, M. Mazza, A. Schönhals and P. Huber - “Characterization of the thermotropic phase behavior and microscopic structure of a confined discotic liquid crystal”

- DESY Research Course 2017, Hamburg 03.2017
 DPG Frühjahrstagung, Dresden 03.2017
 DESY Photon Science Users' Meeting, Hamburg 01.2017
K. Sentker, A. Yildirim, M. Lippmann, T. Hofmann, O. Seeck, A. Kityk, A. Schönhals and P. Huber - "Fabrication of organic nanowires by melt infiltration of a discotic liquid crystal: A combined X-ray diffraction and optical birefringence study"
- GISAXS 2016, Hamburg 11.2016
K. Sentker, A. Yildirim, A. Schönhals, P. Huber - "Discotic Liquid Crystals in Nanoporous Solids"
- DPG Frühjahrstagung, Regensburg 03.2016
K. Sentker, K. Knopp, A. Yildirim, A. Schönhals, P. Huber - "Columnar Axial Orientation of Discotic Liquid Crystals in Nanoporous Solids"

Acknowledgments

Thanks to

- Patrick Huber, Robert Meißner and Otto von Estorff for reviewing this thesis and its defense.
- Patrick Huber for giving me the possibility to write this thesis in his group, his enthusiasm about physics and many fruitful discussions.
- the Deutsche Forschungsgemeinschaft for financial support via project HU 850/5-1 and Sonderforschungsbereich 986.
- the beamline scientists at the P08 beamline at DESY, ID31 beamline at ESRF and 11-BM (CMS) beamline at NSLS II for their excellent support.
- Tommy Hofmann, Milena Lipmann and Manuel Brinker for sharing many hours of beamtime experience.
- Arda Yildirim and Andreas Schönhals for the successful collaboration within the DFG project.
- Arne Zantop and Marco Mazza for the Monte Carlo simulations and the resulting beautiful images.
- Andriy Kityk for many helpful discussions about optics and for proofreading this thesis.
- our technicians Rainer Behn, Dagmar Rings and Claudia Plaumann for their support with experimental setups.
- all current and former members of the Institute of Materials Physics and Technology, especially Mark Busch and Manuel Brinker for the good teamwork, but also for everything beyond. For Regensburg, Dresden and Berlin. For Rotterdam, New York and everything in between.
- Lena Meyer and Thilo Sentker for proofreading this thesis.
- again Thilo Sentker for his LaTeX and MATLAB support.
- my former fellow students for many years of shared physics and the friendships that have arised out of it: Carolin Behncke, Lena-Marie Woelk, Jana von Poblitzki, Tobias Dressel, Pablo Woelk, Philipp Neuhäuser, Hannes Wittern and Leon Kolbe.

- my friends and family for their constant support in things far beyond physics.
Thanks you so much: Thilo and Thorben Sentker, Lena Meyer, Roswitha and Bernd Eckholt and Peter Sentker.